New Methods for Terahertz and Ultrafast Infrared Spectroscopy of Biological Materials and Graphene Buffer Layer

by

Gong Cheng

A dissertation submitted in partial fulfillment
of the requirements for the degree of
Doctor of Philosophy
(Physics)
in the University of Michigan
2019

Doctoral Committee:

Professor Theodore B. Norris, Chair
Professor Nicholas A. Kotov
Professor Cagliyan Kurdak
Associate Professor Lu Li
Professor Kamal Sarabandi

Gong Cheng

gongch@umich.edu

ORCID iD: 0000-0002-1206-1762

Dedication

To my family

Acknowledgements

The past seven years has been a wonderful journey, both for my research and for my life. I am truly thankful for everyone who has supported me and helped me during this period, and it is them who made this journey unforgettable.

First, I am sincerely grateful to my advisor, Prof. Theodore Norris. He provided me a wide range of projects and gave me much freedom to learn and explore myself; at the same time, he was always there when I needed directions and suggestions. This work could not be done without his vision and guidance. I also really appreciate his advice for my career development and support for my family.

I am thankful for all my committee members – Prof. Nicholas Kotov, Prof. Cagliyan Kurdak, Prof. Kamal Sarabandi and Prof. Lu Li – for taking time reading my thesis and providing invaluable feedback. I would especially like to thank Prof. Kotov, with whom I collaborated for three amazing THz projects, for his tremendous help and support for my research and publications.

All my research projects were highly interdisciplinary, and it was my enormous privilege to work with so many outstanding scientists and engineers from various fields over the years. I want to thank Won Jin Choi from Prof. Nicholas Kotov's group for the wonderful experience developing THz polarimetry and kirigami modulators together. For the biofilm projects, I would like to thank Usha Kadiyala and Christopher Altheim from Prof. J. Scott VanEpps' group for growing the biofilms, Hee-Jeong Jang from Prof. Kotov's group for preparing the samples and taking the measurements together, Yichun Wang and Paolo Elvati from Prof. Angela Violi's group for the molecular dynamics simulations. For the graphene buffer layer project, I want to thank Jean-Philippe Turmaud from Prof. Walt de Heer's group at the Georgia Institute of Technology for providing the samples and designing the high temperature experiment. Also, I want to thank Dehui Zhang from Prof. Zhaohui Zhong's group for the collaboration on the graphene photodetector and photo-Dember projects.

As an experimentalist, it is important to learn skills and gain experience from others. I was fortunate to have a group of great lab mates: Jessica Ames, Momchil Mihnev, You-Chia Chang, Miao-Bin Lien, Heather George, Laura Elgin, Nooshin Mohammadi Estakhri, Zhen Xu, Zhengyu Huang, Yifan Shen and Liangqing Cui. I would like to give special thanks to Momchil who taught me a lot about the THz system and You-Chia who provided much help on the lasers and the bolometer when I first joined the group. I also want to give my gratitude to Steve Katnik for his tremendous assistance with our lasers.

I am indebted to all my friends in the United States and back in China, especially my two best friends Hao Liu and Huan Yang for their continued help and encouragement for my study, job search and my life. I will always remember those wonderful moments we had together, and I believe we all will have a bright future.

Finally, I would like to express my deepest gratitude to my beloved family. I thank my parents for raising me up and giving me unlimited love, care and support. I thank my wife, Shuai, for being together with me through ups and downs during my whole PhD years and for always believing in me. I thank my son, Vincent, for the great joy he has brought to this family.

Table of Contents

List of Figures

Abstract

The development of advanced optical spectroscopy has always been a frontier in optics and material science. This dissertation develops several new methods for terahertz (THz) and infrared spectroscopy and presents their applications for the better understanding of biological materials and novel two-dimensional (2D) materials.

One limitation of current THz spectroscopy has been its inability to reveal the chiral properties, e.g. circular dichroism (CD), of complex materials. Our first new spectroscopic method aims to solve this issue using existing experimental techniques. Based on the conventional THz time-domain spectroscopy and with three additional wire-grid linear polarizers, a complete THz time-domain polarimetric (THz-TDP) methodology is developed to extract CD in any generalized complex materials through a sequence of linear polarization measurements. The accuracy and effectiveness of the new method are demonstrated and justified by the measurements of several test samples including anisotropic polymer sheet and chiral DNA solutions.

Next, THz-TDP is applied for the study of several bacterial biofilms, including *S. aureus* and *B. subtilis* biofilms grown in PNG and TSBg media, both in freeze-dried and pristine wet states. An absorption band at 0.6 – 0.8 THz and negative circular dichroism at around 1 THz are consistently found in all the samples and match the predictions from molecular dynamics simulations. These results are not only essential for the understanding of the low-energy vibrations of the extracellular matrix (ECM) components in these biofilms, but also could provide insight into the further investigation of the potential electromagnetic communication between biological cells.

Another long-standing problem in THz spectroscopy is the lack of THz polarization modulators and related optical devices. To tackle this problem, we develop an entirely new approach to the real-time polarization modulation of THz beams using tunable and reconfigurable kirigami plasmonic metasurfaces, achieving polarization rotation as large as 80° and ellipticity up to 40°. Based on these kirigami modulators, another new spectroscopic method – THz circular dichroism (TCD) spectroscopy – is developed and demonstrated on several chemical and biological materials.

Lastly, ultrafast time-resolved infrared spectroscopy for both room temperature and high temperature above 1000 °C is developed to study the optical properties of epitaxial graphene buffer layer on SiC(0001). This novel 2D material exhibits very different optical responses from conventional graphene layers, with a proposed bandgap opening between 2 eV to 2.4 eV due to the interaction with the substrate. The preliminary results also indicate the possibility of its temperature-dependent transition from semiconducting to semimetal form, which is hypothesized to be caused by the decoupling of the buffer layer from the substrate.

Chapter 1

Introduction

1.1 Motivation and thesis organization

Over the past decades, dramatic advances have been made in the generation, manipulation and detection of ultrafast laser pulses, and they have found numerous applications in science and technology [1-8] enabled by a combination of unique characteristics of ultrafast pulses, including high temporal and spatial resolution, high bandwidth and high intensity [9]. All these characteristics make ultrafast spectroscopy a powerful tool for the characterization of materials, spanning from picosecond (10^{-12} s) to attosecond (10^{-18} s) [10,11] in time scale for different processes and dynamics, ranging from x-ray [11] to THz in frequency/wavelength domain for all kinds of transitions and modes, and allowing both linear and nonlinear phenomena with up to 10^{22} W/cm^2 intensity [12,13].

The current research in ultrafast spectroscopy is at a stage where in some areas mature methods are being used to investigate novel materials and devices, while in some other areas new optical techniques are still in development for the complete understanding of materials that have been known for long time. One example is that, in the visible and near-infrared ranges various spectroscopic methods that have been fully developed over years are being used for the characterization of novel two-dimensional (2D) materials such as graphene, transition metal dichalcogenides (TMDs), and black phosphor [1,14,15]; on the contrary, the variety of THz spectroscopy is greatly limited by the lack of necessary optical components [16], e.g. efficient intense source and convenient modulators, and therefore the deep understanding of many biological materials with potential THz modes, such as DNA, amino acid and bacterial communities, requires further advances in the spectroscopic methodology.

This dissertation covers both the new development of advanced ultrafast spectroscopic techniques, specifically in infrared (IR) and terahertz (THz) regions, and their applications to the studies and discoveries of key processes and properties in many types of materials, including biological materials, metamaterials and novel 2D semiconductors. In Chapter 1, a general ultrafast laser system, which is used to further generate different frequencies used for the IR and THz spectroscopy, is introduced. In Chapter 2, new THz time-domain polarimetric methods are developed to study the complete optical properties of generalized complex materials. In Chapter 3, the THz polarimetric spectroscopy is applied to the study of normal vibrational modes and electromagnetic processes in bacterial communities, i.e. biofilms. In Chapter 4, a THz polarization modulator using plasmonic kirigami metasurfaces is developed and demonstrated for the direct realization of THz circular dichroism (TCD) spectroscopy. In Chapter 5, the optical properties of novel buffer layer graphene on SiC is investigated using time-resolved IR spectroscopy. In Chapter 6, a brief conclusion of the research work in this dissertation and remarks on future directions for each project are presented.

1.2 Ultrafast laser system

The central tool and source for our ultrafast spectroscopy is an ultrafast laser system which generates and amplifies femtosecond (10^{-15} s) laser pulses. A Ti:Sapphire oscillator provides initial ultrashort pulses which are then amplified by a regenerative amplifier together with the technique of chirped pulse amplification (CPA). The resulting 800-nm pulses are converted into longer wavelengths either in near-IR by an optical parametric amplifier (OPA) or in THz range by an active photoconductive antenna. The short pulse duration provides sub-picosecond temporal resolution for the time-resolved spectroscopy and the amplified peak intensity enables the frequency conversion and tunability into longer wavelengths in infrared and THz regions.

This section describes the commercially purchased lasers that are basic components of the general ultrafast laser system. The self-built experimental setups for THz time-domain spectroscopy (THz-TDS) and time-resolved near-IR spectroscopy are described in their respective chapters.

1.2.1 Ti: Sapphire oscillator

The oscillator (Mira, Coherent Inc.) is a mode-locked ultrafast laser that produces ultrashort, wide bandwidth, femtosecond pulses using Titanium:Sapphire (sapphire doped with titanium) as the gain medium, and is designed for optimum bandwidth and amplifier seeding. Figure 1-1 shows the schematic of the Ti:Sapphire oscillator, which is optically pumped by a 5 W continuous-wave (CW), frequency-doubled Nd:Vanadate (Nd:YVO_4) solid state laser (Verdi V5, Coherent Inc.) running at 532 nm and produces 60 fs, 7 nJ pulses with 600 mW average power, 800nm center wavelength and >25 nm spectral bandwidth at a repetition rate of 76 MHz. The laser is mode-locked through “Kerr lens mode-locking” [18] which is induced by a combination of self-focusing and spatial modulation by the intracavity slit. The short crystal negative group velocity dispersion (-GVD) accomplished by a pair of fused silica prisms results in negligible second order and reduced third order dispersion. An auxiliary cavity by removing one prism (BP1) from the beam path is also included for the alignment purposes.

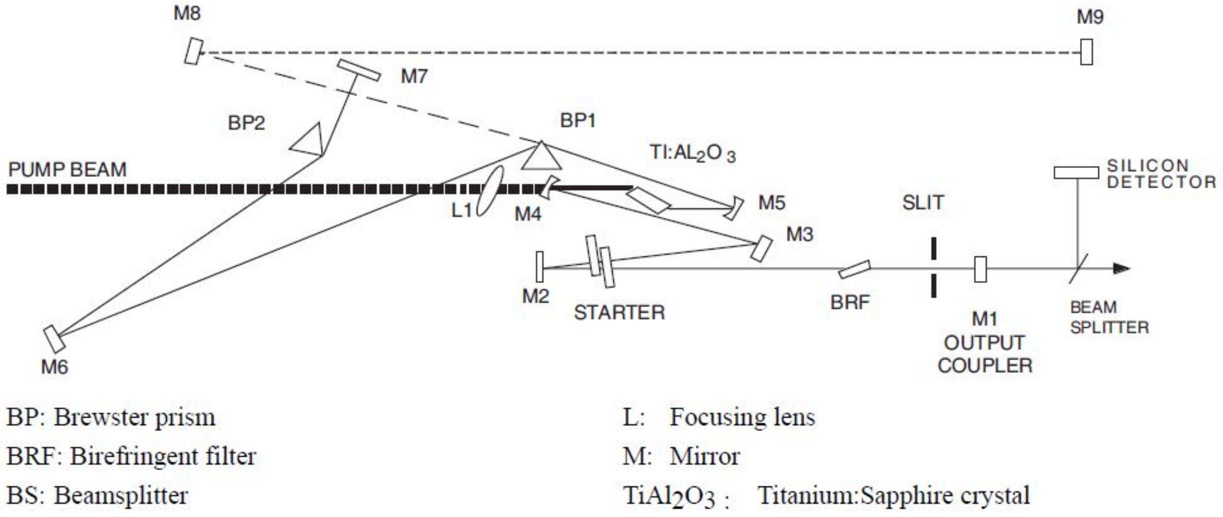

Figure 1-1. Schematic of a Ti:Sapphire oscillator. Taken from Ref. [17].

1.2.2 Ti: Sapphire regenerative amplifier

The pulse energy from the oscillator is amplified by a Ti:Sapphire regenerative laser (RegA 9000, Coherent Inc.) whose schematic is shown in Figure 1-2 [20]. The laser is optically pumped by a 12 W CW solid-state laser at 532 nm (Sprout G-12W, Lighthouse Photonics). Q-switching in the system sets the target repetition rate at 250 kHz, which is limited by the ~3 μs lifetime of Ti:

Sapphire. When the Q-switch is closed, the system cannot achieve lasing and a population inversion develops in the Ti:Sapphire crystal. When the Q-switch is open, a pulse from the oscillator is injected by a SiO_2 acousto-optic cavity dumper and circulates inside the cavity. The amplification is done over 25 to 35 round trips after it depletes the gain. The amplified pulse with an energy of ~5 μJ is then ejected out of the cavity by the same cavity dumper and returns through the Faraday isolator which isolates the back-reflection light from the oscillator.

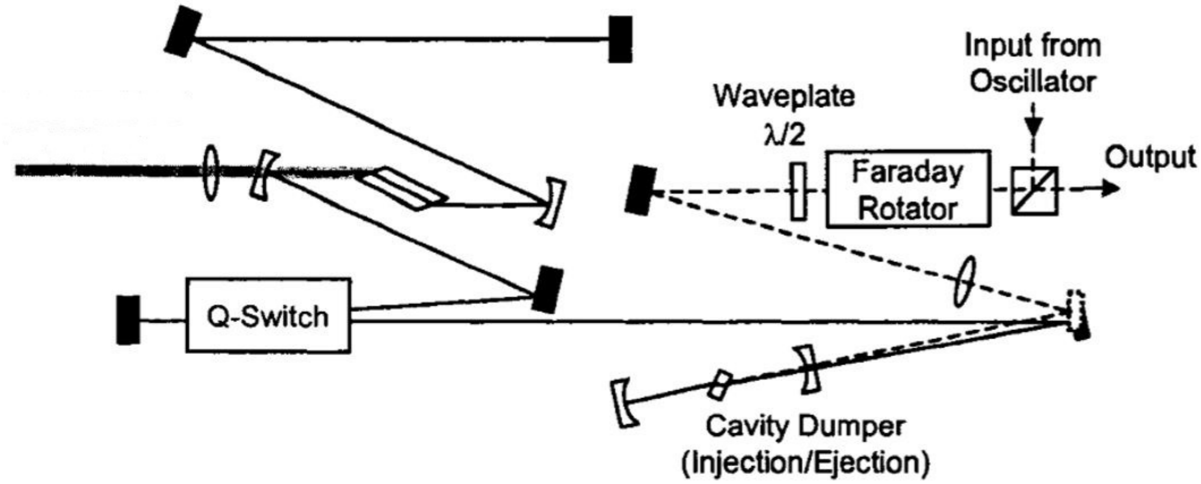

Figure 1-2. Schematic of a Ti:Sapphire regenerative amplifier. Adapted from Ref. [19].

1.2.3 Chirped pulse amplification

To avoid serious damage caused by high laser intensity to the Ti:Sapphire crystal in the amplifier, the technique of chirped pulse amplification (CPA), which was awarded the Nobel Prize in Physics in 2018, is used to stretch the pulse before the amplification and then recompress the pulse to the desired duration [21]. Figure 1-3 shows a typical scheme of CPA. The femtosecond pulse from the oscillator is first expanded using a pair of gratings by a factor of ten thousand or more to nanosecond duration, so that the peak intensity is low enough to be safely amplified to much higher energy level without any nonlinear effects (e.g. self-focusing) and gain medium breakdown. The ejected pulse from the regenerative amplifier is then compressed by a second pair of gratings resulting a high-energy, ultrashort pulse. For our ultrafast laser system, the stretching and recompression are accomplished by a unified expander/compressor (EC 9150, Coherent Inc.) and the resulting pulse after CPA has a ~80 fs pulse duration, ~5 μJ pulse energy at 250 kHz repetition rate.

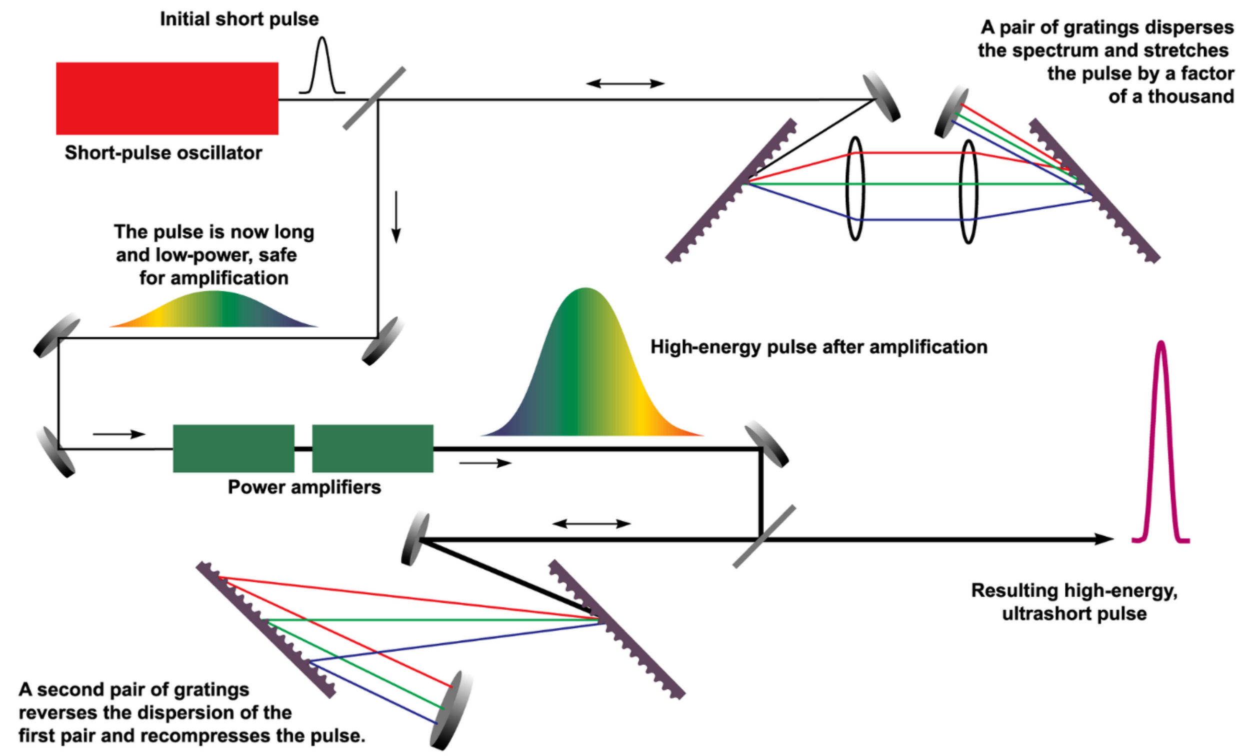

Figure 1-3. Scheme of chirped pulse amplification (CPA). Taken from Ref. [22].

1.2.4 Optical parametric amplifier

The amplified pulses at 800 nm are then directed into different systems to be converted to either infrared or THz frequencies: the THz generation and detection will be discussed in the next chapter; for the near-IR wavelengths, an optical parametric amplifier (OPA) is used to produce amplified femtosecond pulses tunable from 1.2 μm to 2.4 μm at a 250 kHz repetition rate. The schematic of our OPA (OPA 9850, Coherent Inc.) is shown in Figure 1-4. The 800 nm RegA output enters the OPA and is split into two arms: 25% of energy is used to generate the white light continuum [24] in the 460 nm to 1600 nm spectral range via the thick sapphire crystal, and the other 75% passes through a waveplate rotating its polarization by 90° to provide the pump for the parametric amplification process [25]. The two arms are recombined through a dichroic mirror and focused onto a type-II Beta-Barium Borate (BBO) crystal, and an adjustable optical delay (first pass delay) is used to exactly match the timing of the pump and white light pulses. After the first pass through the BBO crystal, a small amount of signal (1.2 μm – 1.6 μm) and idler (1.6 μm – 2.4 μm) are generated. The signal and the 800 nm pump are then separated, reflected and recombined for a second pass through the BBO crystal with their relative timing adjusted by another adjustable optical delay (second pass delay). In this double-pass configuration, the first pass weakly saturates the amplifier's gain while the second pass extracts ~10% of the 800 nm pump energy, resulting in ~100 mW signal and ~30 mW idler which are separated from remnant 800 nm pump as output for the subsequent experiments. The exact signal and idler wavelengths can be angle-tuned by an external micrometer to adjust the phase matching condition of the BBO crystal.

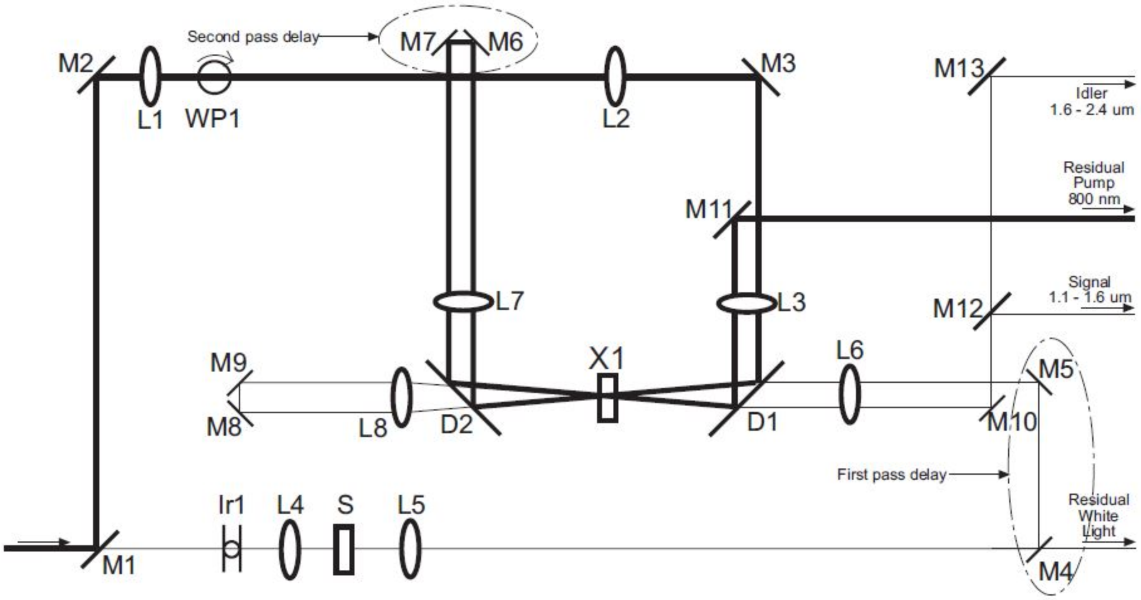

M:	Mirror	WP:	Waveplate
D:	Dichroic mirror	Ir:	Iris
L:	Lens	X:	Optical parametric amplifier Beta Barium Borate crystal
S:	Sapphire crystal		

Figure 1-4. Schematic of an optical parametric amplifier (OPA). Taken from Ref. [23].

Reference

1. Sun, D., et al. Ultrafast relaxation of excited Dirac fermions in epitaxial graphene using optical differential transmission spectroscopy. *Phys. Rev. Lett.*, **101**, 157402, (2008).
2. Beaurepaire, E., Merle, J. C., Daunois, A., and Bigot, J. Y. Ultrafast spin dynamics in ferromagnetic nickel. *Phys. Rev. Lett.*, **76**, 4250, (1996).
3. Nibbering, E. T., Fidder, H., and Pines, E. Ultrafast chemistry: using time-resolved vibrational spectroscopy for interrogation of structural dynamics. *Annu. Rev. Phys. Chem.*, **56**, 337-367, (2005).
4. Spörlein, S., et al. Ultrafast spectroscopy reveals subnanosecond peptide conformational dynamics and validates molecular dynamics simulation. *Proc. Natl. Acad. Sci. U.S.A.*, **99**, 7998-8002, (2002).
5. Juhasz, T., Loesel, F. H., Kurtz, R. M., Horvath, C., Bille, J. F., and Mourou, G. Corneal refractive surgery with femtosecond lasers. *IEEE J. Sel. Top. Quantum Electron.*, **5**, 902-910, (1999).
6. Sugar, A. Ultrafast (femtosecond) laser refractive surgery. *Current opinion in ophthalmology*, **13**, 246-249, (2002).
7. Sugioka, K., and Cheng, Y. Ultrafast lasers-reliable tools for advanced materials processing. *Light Sci. Appl.*, **3**, e149, (2014).
8. Malinauskas, M., Žukauskas, A., Hasegawa, S., Hayasaki, Y., Mizeikis, V., Buividas, R., and Juodkazis, S. Ultrafast laser processing of materials: from science to industry. *Light Sci. Appl.*, **5**, e16133, (2016).
9. Weiner, A. *Ultrafast optics* (Vol. 72). John Wiley & Sons, (2011).
10. Krausz, F., and Ivanov, M. Attosecond physics. *Rev. Mod. Phys.*, **81**, 163, (2009).
11. Hentschel, M., et al. Attosecond metrology. *Nature*, **414**, 509, (2001).
12. Bahk, S. W., et al. Generation and characterization of the highest laser intensities (10 22 W/cm 2). *Opt. Lett.*, **29**, 2837-2839, (2004).
13. Yanovsky, V., et al. Ultra-high intensity-300-TW laser at 0.1 Hz repetition rate. *Opt. Express*, **16**, 2109-2114, (2008).
14. Wang, H., Zhang, C., and Rana, F. Ultrafast dynamics of defect-assisted electron–hole recombination in monolayer MoS2. *Nano Lett.*, **15**, 339-345, (2014).
15. Wang, Y., et al. Ultrafast recovery time and broadband saturable absorption properties of black phosphorus suspension. *Appl. Phys. Lett.*, **107**, 091905, (2015).
16. Dhillon, S. S., et al. The 2017 terahertz science and technology roadmap. *J. Phys. D*, **50**, 043001, (2017).
17. Mira seed laser operator’s manual. Coherent, Inc.

18. Brabec, T., Spielmann, C., Curley, P. F., and Krausz, F. Kerr lens mode locking. *Opt. Lett.*, **17**, 1292-1294, (1992).
19. Wu, Z.-K. J., Ultrafast electronic dynamics in unipolar n-doped indium gallium arsenide/gallium arsenide self-assembled quantum dots. Ph.D Thesis, University of Michigan, (2006).
20. Norris, T. B. Femtosecond pulse amplification at 250 kHz with a Ti: sapphire regenerative amplifier and application to continuum generation. *Opt. Lett.*, **17**, 1009-1011, (1992).
21. Strickland, D., and Mourou, G. Compression of amplified chirped optical pulses. *Opt. Commun.*, **55**, 447-449, (1985).
22. Perry, M., Shore, B., Boyd, R., and Britten, J. Multilayer dielectric gratings: Increasing the power of light. *Science & Technology Review*, **9**, 25-33, (1995).
23. Optical parametric amplifier 9800/9850 operator's manual. Coherent, Inc.
24. Brodeur, A., and Chin, S. L. Ultrafast white-light continuum generation and self-focusing in transparent condensed media. *J. Opt. Soc. Am.*, **16**, 637-650, (1999).
25. Shen, Y. R. The principles of nonlinear optics. *New York, Wiley-Interscience*, (1984).

Chapter 2

THz Time-Domain Polarimetry for Generalized Anisotropic and Chiral Materials

2.1 Chapter introduction

Characterizing THz anisotropy and chirality such as THz linear dichroism (TLD) and THz circular dichroism (TCD) is essential for understanding the mesoscale structures and low-energy vibrations of biological molecules [1-3] such as DNA and proteins, as well as for designing and optimizing metamaterials for THz functionalities [4,5]. Due to the lack of efficient THz polarization modulators [6], however, THz anisotropy and especially chirality spectroscopy are far from standard metrology techniques, not to mention any applications in the fields of biochemistry and materials science.

Although some active THz polarization modulators [4,5] or electronic control methods [7] have been proposed and demonstrated to function similarly to a photoelastic modulator (PEM) in a conventional circular dichroism (CD) spectrometer [8] to generate alternating left- and right-handed circular/elliptical polarizations, they have the problems that either the polarization modulation is small and narrowband or the required optical devices and control schemes are fairly bulky and complicated.

In this chapter, I will describe two THz polarimetric methodologies based on conventional terahertz time-domain spectroscopy (THz-TDS) with three additional wire-grid linear polarizers. They require no change of existing THz-TDS setup and is free of any complicated electronic controls and synchronizations. In addition to the standard optical properties measured by THz-TDS such as transmission and optical constants, they provide the complete information about anisotropy and chirality for a generalized material through measuring full electric field vector, deriving Jones matrix and calculating specific quantities, therefore our terahertz time-domain polarimetry (THz-TDP) can be considered as a replacement and upgrade of the conventional THz-TDS. The details of the experimental settings, mathematical procedures and property quantifications of the proposed methods will be described and the experimental results on an anisotropic polymer sheet showing the effectiveness of the methods and the preliminary data of chiral DNA molecules for the first time in the THz frequency range will also be presented.

This work was done in collaboration with Prof. Nicholas Kotov's group from Chemical Engineering. The sample fabrication and preparation were performed by Won Jin Choi and Hee-Jeong Jang from Kotov group. I proposed the THz polarimetric methods, built the experimental setup and performed the optical characterization of the samples. The results of this work are published as an invited paper in *SPIE Photonics West* in 2019 [9].

2.2 THz time-domain spectroscopy (THz-TDS)

THz time-domain spectroscopy (THz-TDS) has been widely used for the last three decades to extract material parameters of metals [10], dielectrics [11,12], semiconductors [11,12] and novel 2D materials e.g. graphene [13] and to probe vibrational bands in molecules [14,15] through measuring electric field transmission. A schematic representation of a typical THz-TDS spectrometer is shown in Figure 2-1. Optical pulses from a femtosecond laser are separated by a beamsplitter into two arms: one excites a THz photoconductive (PC) switch generating THz pulses which are focused onto sample and then collected by two pairs of parabolic mirrors; the other arm goes to a crystal detector such as a piece of ZnTe or GaP for the THz detection with the method of electro-optic (EO) sampling [16]. An optical delay line is used to adjust the relative timing between the two arms to map out the electric field of THz pulse in time domain. A fast Fourier transform (FFT) is then applied to obtain the magnitude and phase information in frequency domain from which optical parameters such as dielectric constant and refractive index can be extracted.

Figure 2-2 shows the experimental data for a THz pulse generated and measured with our THz-TDS system after averaging 100 scans. Figure 2-2 (a) is the time-domain waveform of the

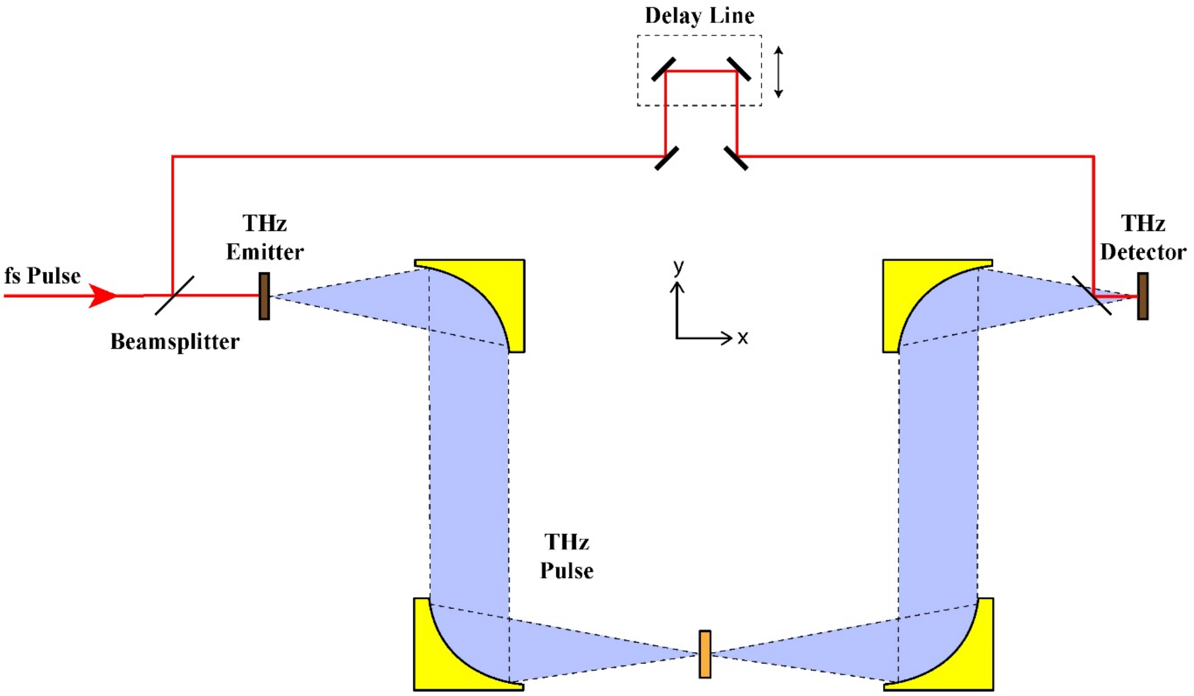

Figure 2-1. Schematic illustration of a THz-TDS spectrometer showing the laser excitation source, optical delay line, THz emitter and detector, and parabolic mirrors. Adapted from Ref [9].

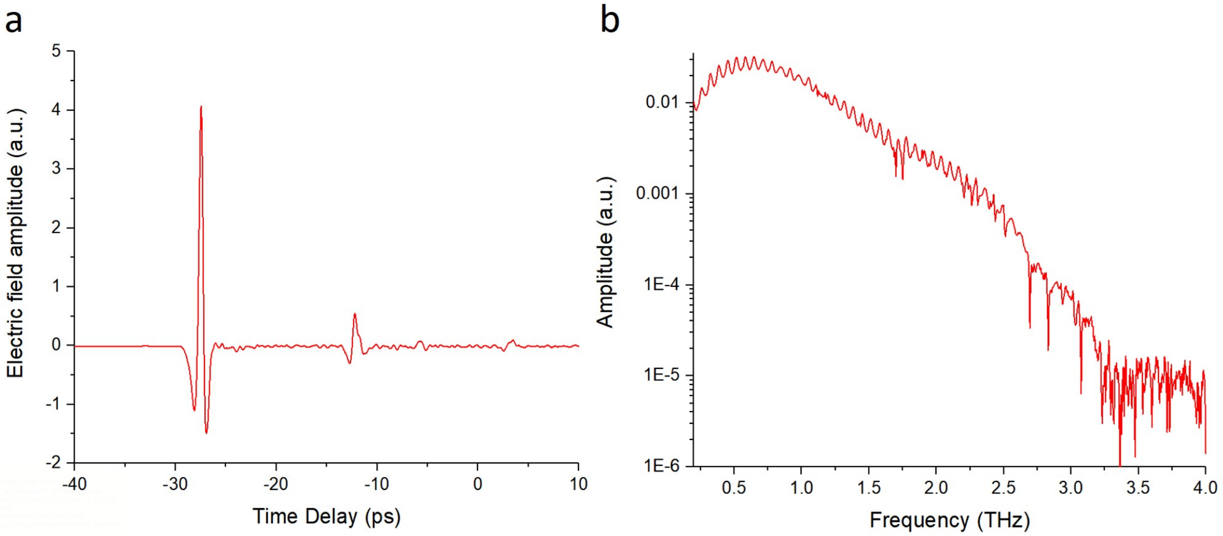

Figure 2-2. Experimental data of a THz pulse generated and measured by THz-TDS. (a) Time-domain waveform. (b) Frequency-domain spectrum.

THz pulse. The small peaks after the large main peak are due to the reflections inside the THz emitter and detector. Figure 2-2 (b) shows the amplitude of the frequency-domain spectrum after the Fourier transform of the time-domain signal. The fringe pattern is caused by the interference between the main THz peak and the reflected peaks. As can be seen, the spectral range is from 0.2 – 3 THz and the signal-to-noise ratio (SNR) is of the order of 10^5. The additional phase information is not visualized here.

2.3 THz time-domain polarimetry (THz-TDP) for electric field and polarization state

Based on the conventional THz-TDS described above and without major modification, a THz time-domain polarimetry (THz-TDP) measuring full electric field and characterizing the polarization changes induced by materials can be achieved using three additional wire-grid linear polarizers [17]. One advantage of this method is that it is perfectly compatible with existing THz-TDS apparatus because the additional polarizers can be simply inserted or taken out to switch between the two setups.

Here the THz emitter is fixed at an orientation such that its generated THz polarization is perpendicular to the detection direction of the THz detector, so any small polarization rotation can be measured with maximum sensitivity and accuracy. Without loss of generality, it can be assumed that the generated THz has a horizontal linear polarization and the THz detector only registers vertical linear polarization. As shown in Figure 2-3, two fixed wire-grid polarizers are respectively placed after the emitter (P1) to ensure the incident polarization is along horizontal direction and in front of the detector (P3) to further increase the polarization contrast, and the third polarizer (P2) is placed between sample and P3 and can be rotated to different positions to determine the electric field vector: the vertical component $E_y(t)$ is measured when the P2's transmission axis is aligned with P3's, and the horizontal component $E_x(t)$ is measured by rotating the orientation of P2 to +45° and -45° relative to P3 and calculated by the subtraction of the two. Since any arbitrary electric field can be decomposed into two perpendicular components, the total electric field and its corresponding polarization state can be fully determined with these three measurements. Therefore, polarization state change induced by the materials can be obtained by comparing the transmitted electric fields with and without the sample.

Mathematically, the horizontal component of the transmitted electric field can be calculated by

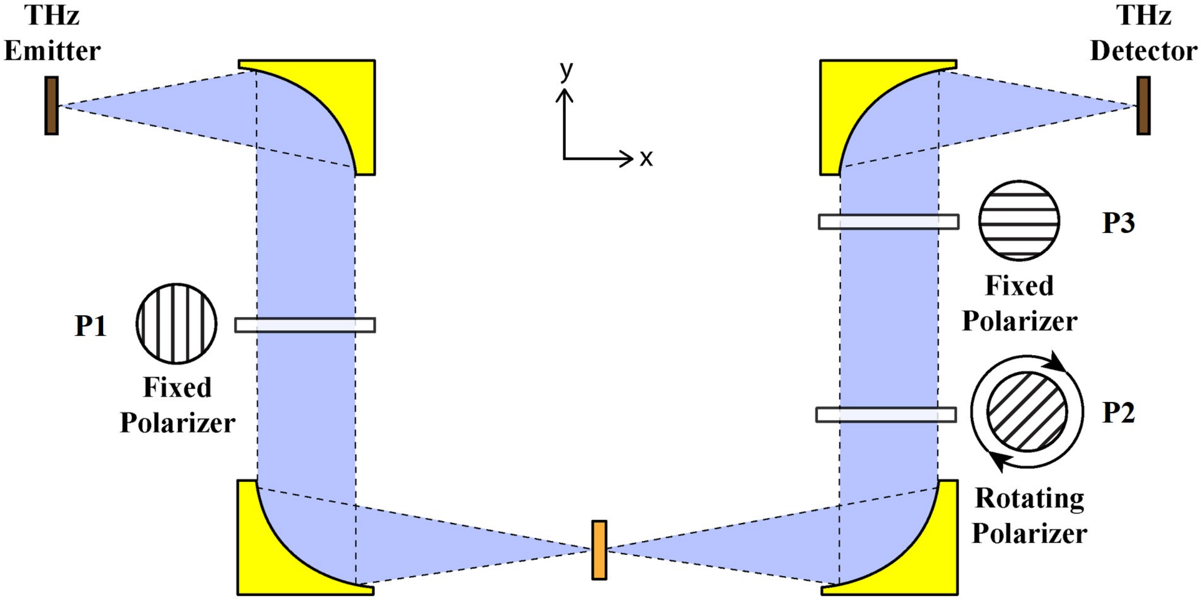

Figure 2-3. Schematic illustration of a THz-TDP spectrometer using three wire-grid polarizers. The polarizer positions are indicated by the white rectangles with adjacent circles indicating their orientations viewed along the optical axis. The THz emitter is oriented such that the polarization of the generated THz pulse is horizontal, and the detection direction of the THz detector is vertical. Adapted from Ref [9].

$$E_x(t) = E_{+45^\circ}(t) - E_{-45^\circ}(t) \tag{2.1}$$

where $E_{+45^\circ}(t)$ and $E_{-45^\circ}(t)$ are the time-domain electric fields measured when the transmission axis of polarizer P2 is at +45° and -45° relative to that of polarizer P3. The vertical component $E_y(t)$ is directly measured when P2 is aligned with P3 therefore requiring no further calculation.

The frequency-domain electric field spectra can be obtained by applying FFT to the time-domain signals, so

$$\begin{gathered} \tilde{E}_x = \tilde{E}_x(\omega) = FFT\{E_x(t)\} \\ \tilde{E}_y = \tilde{E}_y(\omega) = FFT\{E_y(t)\} \end{gathered} \tag{2.2}$$

With these two electric field components, Stokes parameters [18] can be defined as

$$S_0 = \tilde{E}_x\tilde{E}_x^* + \tilde{E}_y\tilde{E}_y^*$$

$$S_1 = \tilde{E}_x\tilde{E}_x^* - \tilde{E}_y\tilde{E}_y^*$$

$$S_2 = \tilde{E}_x\tilde{E}_y^* + \tilde{E}_y\tilde{E}_x^*$$

$$S_3 = i(\tilde{E}_x\tilde{E}_y^* - \tilde{E}_y\tilde{E}_x^*) \tag{2.3}$$

from which the polarization state can be characterized by polarization rotation angle θ and ellipticity angle η as [18]

$$\begin{aligned} \theta &= \frac{1}{2}atan2(S_2,\, S_1), \qquad -\frac{\pi}{2} \leq \theta \leq \frac{\pi}{2} \\ \eta &= \frac{1}{2}sin^{-1}\left(\frac{S_3}{S_0}\right), \qquad -\frac{\pi}{4} \leq \eta \leq \frac{\pi}{4} \end{aligned} \tag{2.4}$$

where θ is relative to the horizontal direction and $atan2(S_2,\, S_1)$ is the four-quadrant inverse tangent function since the rotation angle of an electric field is within the range of $\left[-\frac{\pi}{2}, \frac{\pi}{2}\right]$.

Additionally, the intensity transmission through the sample can be calculated as

$$t = S_0^{sample} / S_0^{ref} \tag{2.5}$$

where S_0^{sample} and S_0^{ref} are the first Stokes parameters for the transmitted electric fields with and without the sample. This quantity is more suitable for the derivation of a sample's absorption coefficient compared to the transmission measured from THz-TDS, when the birefringence or optical activity in the sample is not negligible.

For a simple material absent of anisotropy the polarization rotation and ellipticity only comes from chirality, or vice versa. In these simple cases, this method can provide some information of either anisotropy or chirality and has been used to characterize simple materials exhibiting only anisotropy [19] or only chirality [4,20,21]. However, it does not work for generalized materials with both anisotropy and chirality or for unknown materials that need to be characterized in terms of both anisotropy and chirality, because it only measures the state of electric field instead of the actual optical parameters of materials and it is impossible to distinguish individual effects of anisotropy and chirality just through a single measurement of electric field. It needs some modifications and more steps to completely determine these optical properties.

2.4 THz-TDP for generalized homogeneous materials

The frequency-dependent Jones matrix completely determines the optical properties including anisotropy and chirality in addition to transmission and induced polarization change of a material [22] and can be written as

$$T = \begin{pmatrix} t_{xx} & t_{yx} \\ t_{xy} & t_{yy} \end{pmatrix} \tag{2.6}$$

where the first subscript letter indicates the incident polarization direction and the second subscript indicates the output direction for detection. It relates the complex amplitudes of the incident electric field $\tilde{E}_{in}$ and the transmitted electric field through the sample $\tilde{E}_s$ by

$$\tilde{E}_s = T\tilde{E}_{in} \tag{2.7}$$

The complex Jones matrix contains eight parameters counting real and imaginary parts of the four transmission coefficients. To completely determine these parameters, it requires at least two sets of electric field measurements of $\tilde{E}_{in}$ and $\tilde{E}_s$ with different relative orientations between incident field and sample.

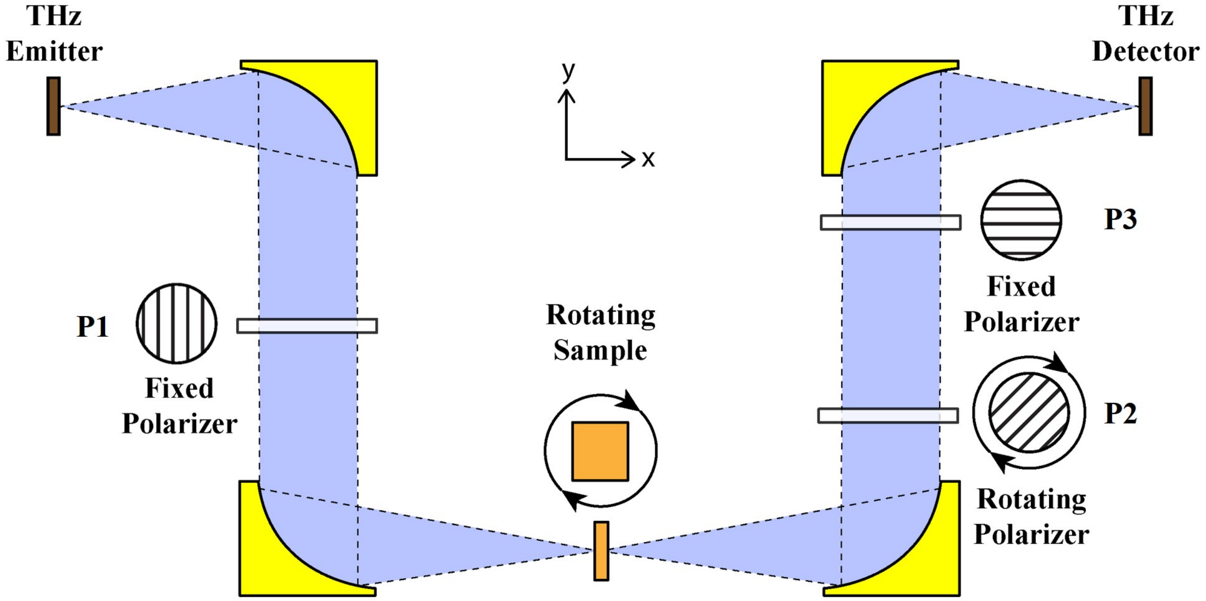

Figure 2-4. Schematic illustration of the modified THz-TDP spectrometer for generalized homogeneous materials. The sample is on a rotation stage and can be rotated to different orientations for the measurement of the material's Jones matrix. Adapted from Ref [9].

For a homogenous material, this different relative orientation can be achieved simply by rotating the sample as shown in Figure 2-4. Here, the homogenous material could be a truly uniform medium, or a periodic material such as a periodically structured metamaterial with a periodicity much smaller than the incident THz spot size in which case the material is effectively “homogeneous” to the THz beam. In this case, at the sample’s first orientation, the two electric fields are related by

$$\begin{pmatrix} \tilde{E}_{sx}^{(1)} \\ \tilde{E}_{sy}^{(1)} \end{pmatrix} = \begin{pmatrix} t_{xx} & t_{yx} \\ t_{xy} & t_{yy} \end{pmatrix} \begin{pmatrix} \tilde{E}_{ref} \\ 0 \end{pmatrix} \tag{2.8}$$

where the superscript “(1)” indicates the first orientation and the subscript “*s*” indicates the electric field transmitted through sample, and the incident electric field is horizontal and measured as reference. Through this equation, two transmission coefficients can be solved by

$$t_{xx} = \tilde{E}_{sx}^{(1)} \,/\, \tilde{E}_{ref}$$

$$t_{xy} = \tilde{E}_{sy}^{(1)} \,/\, \tilde{E}_{ref} \tag{2.9}$$

After rotating the sample by an angle γ, e.g. γ = 90° for convenience, the measured electric fields are related by

$$\begin{aligned} \begin{pmatrix} \tilde{E}_{sx}^{(2)} \\ \tilde{E}_{sy}^{(2)} \end{pmatrix} &= R(90°)TR(-90°) \begin{pmatrix} \tilde{E}_{ref} \\ 0 \end{pmatrix} \\ &= \begin{pmatrix} 0 & -1 \\ 1 & 0 \end{pmatrix} \begin{pmatrix} t_{xx} & t_{yx} \\ t_{xy} & t_{yy} \end{pmatrix} \begin{pmatrix} 0 & 1 \\ -1 & 0 \end{pmatrix} \begin{pmatrix} \tilde{E}_{ref} \\ 0 \end{pmatrix} \\ &= \begin{pmatrix} t_{yy} & -t_{xy} \\ -t_{yx} & t_{xx} \end{pmatrix} \begin{pmatrix} \tilde{E}_{ref} \\ 0 \end{pmatrix} \end{aligned} \tag{2.10}$$

where $R(\gamma)$ is the rotation matrix given by

$$R(\gamma) = \begin{pmatrix} cos(\gamma) & -sin(\gamma) \\ sin(\gamma) & cos(\gamma) \end{pmatrix} \tag{2.11}$$

Thus, the other two transmission coefficients can be solved by

$$t_{yy} = \tilde{E}_{sx}^{(2)} \,/\, \tilde{E}_{ref}$$

$$t_{yx} = -\,\tilde{E}_{sy}^{(2)} \,/\, \tilde{E}_{ref} \tag{2.12}$$

Therefore, the Jones matrix is completely and uniquely determined.

2.5 THz-TDP for generalized inhomogeneous materials

Many materials to be characterized, however, are not homogeneous i.e. neither uniform nor periodic such as highly inhomogeneous biofilms [23] and polycrystalline solids with texture [24] and crystallite size [25,26] much smaller than the THz beam size. For these materials, the above method of rotating sample is not experimentally optimum because any small misalignment between the optical axis and the rotation axis could lead to completely different sample areas and different optical properties probed by the THz pulse.

The most straightforward solution to this problem is to fix the sample position and instead rotate the whole optical setup because this is equivalent to the previous method in terms of relative orientation yet less susceptible to the rotation misalignment due to the much more homogeneous optical components. This rotation of the optical setup, however, requires rotating not only the THz emitter and detector but also the polarization direction of the sampling pulse incident on the EO crystal. To realize this, a waveplate or an optical polarization modulator is needed for the sampling arm, and it needs to be rotated or adjusted as well during the procedure. This could result in some other technical problems including (1) adjusting multiple components is not efficient and more prone to operational mistakes and experimental errors, and (2) rotating polarization using birefringent elements such as waveplates may lead to time delay change which could require more adjustments of the setup, therefore rotating the whole optical setup is not an ideal solution. Also, it is not ideal to only rotate the emitter say by a 90° while keeping the detector unchanged. This is because when the emitter is aligned with the detector along the vertical direction, the small rotated electric field component is in horizontal direction and it needs to be measured twice with P2 at +45° and -45° positions and then calculated using Eq. (2.1). This process has no big influence on measuring a large horizontal electric field component as in the previous methods but could be detrimental for a small electric field component whose magnitude may be only a couple times larger than the noise level because its accuracy would be greatly reduced by the laser fluctuations between the two measurements.

Here, we develop an alternative THz-TDP method suitable for the most generalized materials which is easy and efficient to operate yet remains highly sensitive and robust. As shown in Figure 2-5, the THz-TDP setup is the same as before and the only difference is that the first polarizer P1 is free to rotate while the sample is kept fixed. Rotating the uniform and thin wire-grid polarizer doesn't affect the propagation direction of THz beam, so the rotation misalignment can be avoided. For a symmetric operation and the maximum total sensitivity, the two sets of measurements are taken with P1 at +45° and -45° relative to the THz polarization direction from the emitter which is the horizontal direction. To eliminate the error originated from Eq. (2.1) for a small electric field component, the total electric field is obtained with two measurements instead of three. This is done by rotating the polarizer P2 to be aligned or perpendicular to the polarizer P1. As an example, if P1 is at +45° orientation, then when P2 is aligned with P1 at +45° the direction-unchanged component can be easily measured, and the small rotated electric field component induced by the sample can be measured directly with P2 at -45°. Since polarizer P3 and the detector still only allows vertical component to be recorded, using decomposition, the relation between the recorded and the actual electric field is given by

$$\tilde{E}_x = \sqrt{2}\tilde{E}_{+45^\circ}$$

$$\tilde{E}_y = \sqrt{2}\tilde{E}_{-45^\circ} \tag{2.13}$$

where $\tilde{E}_{+45^\circ}$ and $\tilde{E}_{-45^\circ}$ are the recorded electric field by THz detector with P2 at +45° and -45° respectively, and it should be noted that the x-y coordinate here is rotated with +45° from the original horizontal-vertical coordinate as shown in Figure 2-5. The incident and transmitted electric fields before and after the sample are related by

$$\begin{pmatrix} \tilde{E}_{sx}^{+45^\circ} \\ \tilde{E}_{sy}^{+45^\circ} \end{pmatrix} = \begin{pmatrix} t_{xx} & t_{yx} \\ t_{xy} & t_{yy} \end{pmatrix} \begin{pmatrix} \tilde{E}_{ref}^{+45^\circ} \\ 0 \end{pmatrix}$$

$$\begin{pmatrix} \tilde{E}_{sx}^{-45^\circ} \\ \tilde{E}_{sy}^{-45^\circ} \end{pmatrix} = \begin{pmatrix} t_{xx} & t_{yx} \\ t_{xy} & t_{yy} \end{pmatrix} \begin{pmatrix} 0 \\ \tilde{E}_{ref}^{-45^\circ} \end{pmatrix} \tag{2.14}$$

where the superscripts “+45°” and “-45°” indicate the orientations of polarizer P1. The four transmission coefficients of the Jones matrix can be totally determined as

$$t_{xx} = \tilde{E}_{sx}^{+45^\circ} / \tilde{E}_{ref}^{+45^\circ}$$

$$t_{xy} = \tilde{E}_{sy}^{+45^\circ} / \tilde{E}_{ref}^{+45^\circ}$$

$$t_{yx} = \tilde{E}_{sx}^{-45^\circ} / \tilde{E}_{ref}^{-45^\circ}$$

$$t_{yy} = \tilde{E}_{sy}^{-45^\circ} / \tilde{E}_{ref}^{-45^\circ} \tag{2.15}$$

Again, it should be noted that this Jones matrix is expressed in the rotated x-y coordinate, and to compare it with the results from previous methods it should be transformed back to the horizontal-vertical coordinate using the rotation matrix given by Eq. (2.11) with γ = -45°.

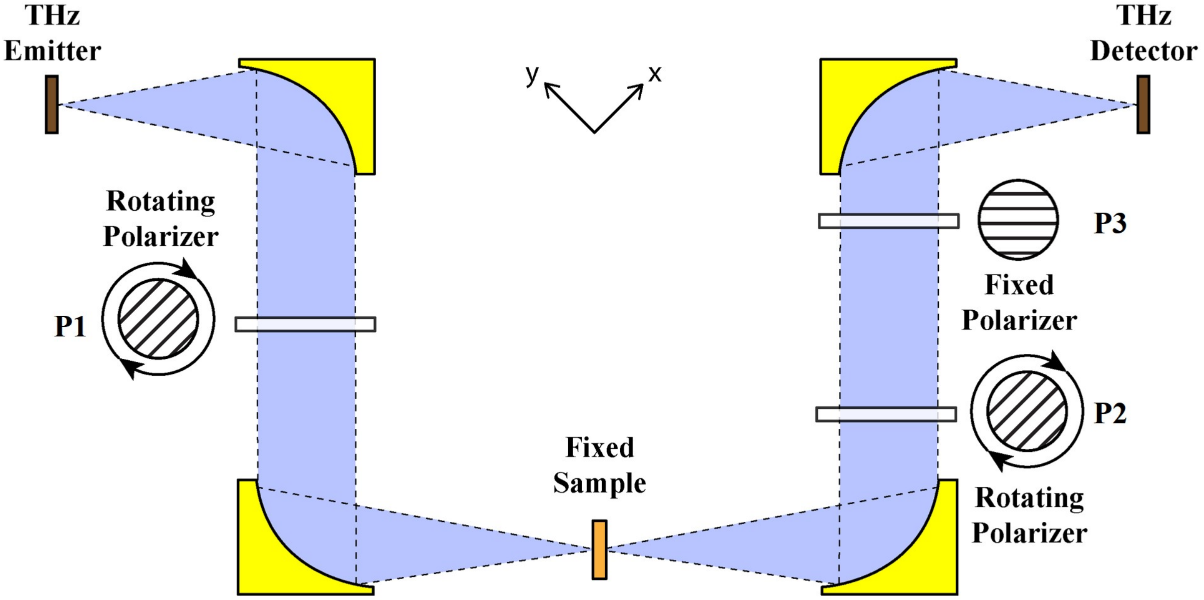

Figure 2-5. Schematic illustration of the modified THz-TDP spectrometer for generalized inhomogeneous materials with sample fixed and P1 rotating. Note that the x-y coordinate here is rotated by +45° relative to the horizontal-vertical coordinate. Adapted from Ref [9].

2.6 Other technical considerations

The above equations are derived under the assumption that the polarizers are ideal and can exactly separate and measure the two perpendicular electric field components, so their effect on the measurement is equivalent to an identity matrix. However, the real polarizers have a finite extinction ratio, so the electric fields measured by polarizers are not exactly the true electric fields.

To improve the accuracy, the actual transfer matrices of these polarizers should be included in the above matrix equations. The Jones matrix of a nonideal polarizer is given by

$$T_{polarizer} = \begin{pmatrix} t_x & 0 \\ 0 & t_y \end{pmatrix} \tag{2.16}$$

where t_x and t_y are the transmission coefficients along its "fast" and "slow" axes, and the matrix needs to be rotated using the rotation matrix in Eq. (2.11) for the actual polarizer orientations in the setup. t_x and t_y can be easily measured experimentally using THz-TDS by aligning the "fast" and "slow" axes along the polarization direction in THz-TDS respectively. With the actual effects of polarizers on the measurement, the general matrix representation relating the measured reference electric field to the true emitted electric field is

$$\tilde{E}_{ref} = T_3T_2T_1\tilde{E}_{emitter} \tag{2.17}$$

where T_1, T_2 and T_3 are the matrix representations of the effects of P1, P2 and P3 on the measurement of electric field and can be obtained using $T_{polarizer}$ and the orientation of each polarizer. $\tilde{E}_{emitter}$ and $\tilde{E}_{ref}$ are two-component electric field vectors whose polarizations are not necessarily linear. With sample inserted, the induced electric field is given by

$$\tilde{E}_s = T_3T_2T_sT_1\tilde{E}_{emitter} \tag{2.18}$$

where T_s is the sample's Jones matrix that needs to be determined. Combining Eq. (2.17) and Eq. (2.18) leads to

$$\tilde{E}_s = (T_3T_2)T_s(T_3T_2)^{-1}\tilde{E}_{ref} \tag{2.19}$$

and each transmission coefficient of T_s can be solved by writing this matrix equation explicitly like Eq. (2.10) and Eq. (2.14). If the polarizers are assumed to be ideal, then T_2 and T_3 are identity matrices and Eq. (2.19) simplifies to Eq. (2.9) and (2.12) or Eq. (2.15).

Alternatively, a more practical method which is also the one used in our experiment is to use two polarizers together as P2. Our wire-grid polarizers have an individual extinction ratio of 200-10000 in the spectral range 0.2-2 THz, so stacking two of them gives an overall extinction ratio well above the maximum signal-to-noise ratio that can be achieved in our experimental setup which is around 20000. Therefore, in this way all the electric field components measured after P2 are strictly linear and P2 and P3 can be experimentally considered as ideal polarizers.

As mentioned above, to uniquely determine the four transmission coefficients of Jones matrix two sets of electric field measurements are needed, and this is achieved by rotating either sample or the polarizer P1 to two different orientations. When more than two sets of data are available, the system of equations for the Jones matrix becomes overdetermined, and from the point of view of numerical linear algebra, least-squares method can be used to improve the precision of the result. Furthermore, much more sets of measurements can be efficiently obtained using automated continuously rotating stages for sample or polarizers [27], and thus precision can be greatly improved.

2.7 Optical properties derived from Jones matrix

With the Jones matrix at hand, various optical properties about the material can be derived. For an arbitrary input electric field $E_{in} = (E_x;\ E_y)$, the transmitted electric field through the material is

$$E_s = TE_{in} = \begin{pmatrix} t_{xx} & t_{yx} \\ t_{xy} & t_{yy} \end{pmatrix} \begin{pmatrix} E_x \\ E_y \end{pmatrix} = \begin{pmatrix} t_{xx}E_x + t_{yx}E_y \\ t_{xy}E_x + t_{yy}E_y \end{pmatrix} \tag{2.20}$$

The Stokes parameters and the polarization states for both electric fields can be calculated with Eq. (2.3) and Eq. (2.4) respectively, and the transmission of this incident electric field through sample is given by Eq. (2.5). As a special example, when the incident electric field is horizontal i.e. $E_{in} = (E_x;\ 0)$, the transmitted electric field is $E_s = (t_{xx}E_x; t_{xy}E_x)$, then the intensity transmission is simplified to $t = |t_{xx}|^2 + |t_{xy}|^2$, and the θ and η calculated with E_s are simply the polarization rotation angle and ellipticity induced by the material which quantify the sample's ability for rotating linear polarization.

The anisotropy of the material can be quantified by THz linear dichroism (TLD) [28] which is defined as the normalized difference between the transmitted electric field magnitudes of two orthogonal linear incident polarizations such as $E_{inx} = \binom{1}{0}$ and $E_{iny} = \binom{0}{1}$. The two transmitted electric fields are

$$E_{sx} = TE_{inx} = \begin{pmatrix} t_{xx} & t_{yx} \\ t_{xy} & t_{yy} \end{pmatrix} \begin{pmatrix} 1 \\ 0 \end{pmatrix} = \begin{pmatrix} t_{xx} \\ t_{xy} \end{pmatrix}$$

$$E_{sy} = TE_{iny} = \begin{pmatrix} t_{xx} & t_{yx} \\ t_{xy} & t_{yy} \end{pmatrix} \begin{pmatrix} 0 \\ 1 \end{pmatrix} = \begin{pmatrix} t_{yx} \\ t_{yy} \end{pmatrix} \tag{2.21}$$

Therefore,

$$TLD = \frac{\sqrt{|t_{xx}|^2+|t_{xy}|^2} - \sqrt{|t_{yx}|^2+|t_{yy}|^2}}{\sqrt{|t_{xx}|^2+|t_{xy}|^2} + \sqrt{|t_{yx}|^2+|t_{yy}|^2}} \tag{2.22}$$

It should be noted that for an anisotropic material the TLD defined in this form is dependent on the sample orientation.

Similarly, the chirality of the material can be characterized by the normalized difference between the transmitted electric field magnitudes of orthogonal right and left circular polarizations (RCP and LCP) which is closely related to THz circular dichroism (TCD) [8,28]. The RCP and

LCP can be expressed as $E_{in}^{RCP} = \frac{1}{\sqrt{2}}\binom{1}{i}$ and $E_{in}^{LCP} = \frac{1}{\sqrt{2}}\binom{1}{-i}$ and their transmitted electric fields are

$$E_s^{RCP} = TE_{in}^{RCP} = \begin{pmatrix} t_{xx} & t_{yx} \\ t_{xy} & t_{yy} \end{pmatrix} \frac{1}{\sqrt{2}}\binom{1}{i} = \frac{1}{\sqrt{2}}\begin{pmatrix} t_{xx}+it_{yx} \\ t_{xy}+it_{yy} \end{pmatrix}$$

$$E_s^{LCP} = TE_{in}^{LCP} = \begin{pmatrix} t_{xx} & t_{yx} \\ t_{xy} & t_{yy} \end{pmatrix} \frac{1}{\sqrt{2}}\binom{1}{-i} = \frac{1}{\sqrt{2}}\begin{pmatrix} t_{xx}-it_{yx} \\ t_{xy}-it_{yy} \end{pmatrix} \tag{2.23}$$

Following the conventional formalism, TCD is defined as the inverse tangent angle of the normalized difference of these two transmitted electric field magnitudes by [8]

$$TCD = tan^{-1}\left(\frac{E_R - E_L}{E_R + E_L}\right) \tag{2.24}$$

where E_R and E_L are the magnitudes of the complex vectors E_s^{RCP} and E_s^{LCP}respectively and are expressed as

$$E_R = \frac{1}{\sqrt{2}}\sqrt{\left|t_{xx} + it_{yx}\right|^2 + \left|t_{xy} + it_{yy}\right|^2}$$

$$E_L = \frac{1}{\sqrt{2}}\sqrt{\left|t_{xx} - it_{yx}\right|^2 + \left|t_{xy} - it_{yy}\right|^2} \tag{2.25}$$

Since a circular polarization is rotationally invariant up to a phase term whose magnitude is unity, the TCD as defined above is independent of sample orientations therefore purely quantifying the chiral properties of the material.

For an arbitrary complex material without any symmetry, the most generalized Jones matrix has the form of [22]

$$T = \begin{pmatrix} t_{xx} & t_{yx} \\ t_{xy} & t_{yy} \end{pmatrix} = \begin{pmatrix} A & B \\ C & D \end{pmatrix} \tag{2.26}$$

where the four elements are all different and not related with each other. For a general chiral material with an *C_2* symmetry with respect to an axis in the x-y plane which is a common case for many biomolecular (poly)crystals [29], the generalized Jones matrix in Eq. (2.26) can be transformed to a simpler form as [22]

$$T_{linear} = \begin{pmatrix} A & B \\ -B & D \end{pmatrix}$$

$$T_{circular} = \begin{pmatrix} T_{++} & T_{+-} \\ T_{-+} & T_{--} \end{pmatrix} = \frac{1}{2}\begin{pmatrix} A+D+2iB & A-D \\ A-D & A+D-2iB \end{pmatrix} \tag{2.27}$$

where T_{linear} and $T_{circular}$ are the transformed matrices in the linear and circular polarization bases, respectively. $T_{circular}$ shows that there is no difference in the circular polarization conversion as for both RCP and LCP it is $A - D$, but the quantity $T_{++} - T_{--} = 2iB$ determines the difference in the optical rotation phases and the dichroic absorptions for RCP and LCP so the element B contains all the information about the chiral properties of the materials. Similarly, T_{linear} shows that the quantity $A - D$ totally represents the anisotropic properties of the materials. Therefore, in this case these two quantities can be used as replacements of the TCD and TLD defined above for characterizing chirality and anisotropy.

2.8 Experimental Data

To test the THz-TDP methods proposed above, measurements were taken on two preliminary materials: an anisotropic polymer sheet and a DNA solution sample.

In our experimental setup, THz is generated by a photoconductive emitter (Tera-SED10, Laser Quantum) and detected by a 1 mm thick (110)-oriented ZnTe crystal. The spot size of the focused THz beam at the sample position is ~500 µm. The wire-grid polarizers (G50 × 20-L, Microtech Instruments, Inc.) have an extinction ratio of 10^3-10^4 in the spectral range of 0.2 – 1.6 THz.

2.8.1 Anisotropic polymer sheet

The first sample is a polymer polarizing sheet made by aligning the iodine-polyvinyl alcohol (PVA) molecules by unidirectional stretching and treated in an iodine bath [30]. It is designed for visible wavelengths and its effectiveness as a polarizer is much reduced at THz frequencies, but it remains anisotropic due to its aligned polymers. The sample is measured with both proposed THz-TDP methods and the results are almost identical. Figure 2-6 shows the data obtained from the more generalized method by rotating the polarizer P1. Figure 2-6 (a) and (b) are the transmission and induced ellipticity for a linear horizontal polarization input. Figure 2-6 (c) is the TCD and it is almost zero for all the frequencies below 1 THz indicating that this polymer sheet has no chirality and thus that the positive ellipticity is totally caused by its anisotropy. The TCD and ellipticity data are noisy and therefore not reliable above 1 THz because the transmission for this range is very small leading to very low signal-to-noise ratio. This data shows that the proposed methods are indeed able to separate and identify the individual effects of anisotropy and chirality.

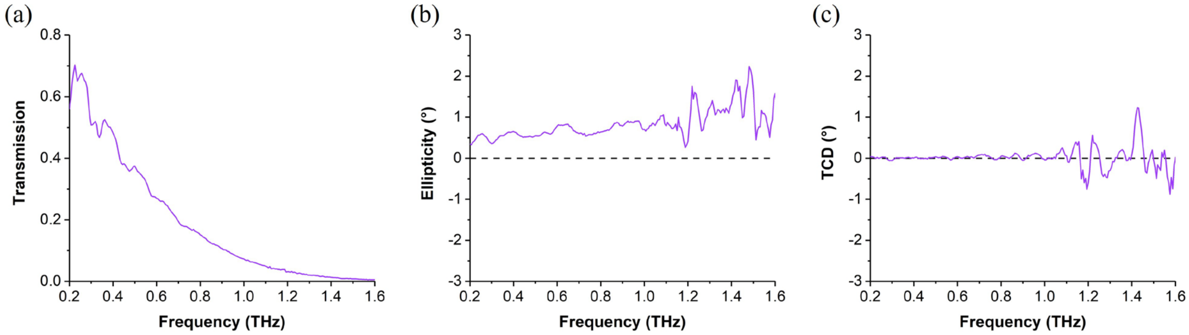

Figure 2-6. Experimental data of an anisotropic PVA polymer sheet measured with THz-TDP. (a) Transmission and (b) induced ellipticity for a linear horizontal polarization input. (c) THz circular dichroism (TCD) of the sample. Adapted from Ref [9].

2.8.2 Chiral DNA solution

The herring testes DNA (D6898, Sigma-Aldrich) is dissolved in deionized (DI) water to the concentration of 10 mg/mL. The DNA solution is then dropped onto a disposable polyethylene (PE) sample card (Z561878, Sigma-Aldrich) forming a gel-like medium sticking to the PE substrate. The measured results of transmission, induced ellipticity and TCD are presented in Figure 2-7. The DNA transmission curve is normalized by that of the PE substrate and shows an absorption band at ~0.4 THz which is consistent with previously published results [31,32]. The ellipticity and TCD of PE substrate are almost zero for the whole range meaning it is neither anisotropic nor chiral, while TCD of DNA shows a broad negative peak below 0.8 THz indicating that it has chirality in this low frequency range. The theory and simulation of the TCD of DNA

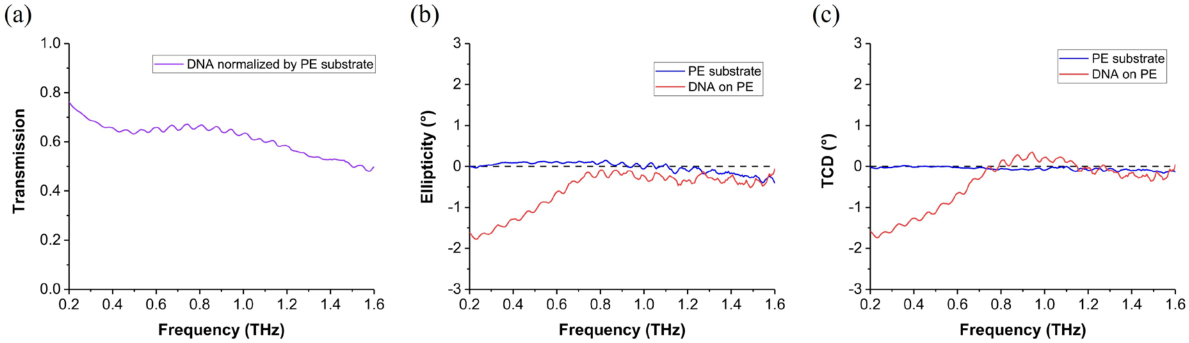

Figure 2-7. Experimental data of a DNA solution sample on PE substrate. (a) Transmission of DNA sample normalized by that of PE substrate. (b) TCD data for both PE substrate and DNA. Adapted from Ref [9].

molecules are currently under investigation. To the best of our knowledge, this is the first spectroscopic CD measurement of biomolecules in the THz range.

2.9 Summary

We have developed two THz polarimetric methodologies for the generalized materials based on the existing THz-TDS and THz-TDP spectroscopy. The new methods can characterize the complete optical properties of a material including transmission, anisotropy and chirality with the determination of the Jones matrix by rotating the sample or the polarizer to produce at least two different relative orientations between the incident polarization and the sample. From the Jones matrix, multiple optical quantities such as intensity transmission, TLD and TCD can be defined and derived. The detailed mathematical expressions are presented and the improvements for better accuracy and precision are also discussed. The two methods are tested and compared experimentally on an anisotropic polymer sheet showing the effectiveness of separating and identifying chirality from anisotropy. The CD data of DNA molecules is also presented for the first time in the THz frequency range, and it is a strong evident that the new methods presented could potentially facilitate the study of complex materials and greatly enhance our understanding of biological molecules.

Reference

1. Acbas, G., Niessen, K. A., Snell, E. H. and Markelz, A. G. Optical measurements of long-range protein vibrations. *Nat. Commun.* **5**, 3076 (2014).
2. Wilmink, G. J. and Grundt, J. E. Invited review article: Current state of research on biological effects of terahertz radiation. *J. Infrared Millim. Terahertz Waves* **32**, 1074–1122 (2011).
3. Choi, J. H. and Cho, M. Terahertz Chiroptical Spectroscopy of an α-Helical Polypeptide: A Molecular Dynamics Simulation Study. *J. Phys. Chem. B* **118**, 12837–12843 (2014).
4. Kan, T., Isozaki, A., Kanda, N., Nemoto, N., Konishi, K., Takahashi, H., Kuwata-Gonokami, M., Matsumoto, K. and Shimoyama, I. Enantiomeric switching of chiral metamaterial for terahertz polarization modulation employing vertically deformable MEMS spirals. *Nat. Commun.* **6**, 8422 (2015).
5. Cong, L., Pitchappa, P., Wang, N and Singh, R. Electrically programmable chiral MEMS photonics. *arXiv*:1807.02914 (2018).
6. Dhillon, S.S., Vitiello, M.S., Linfield, E.H., Davies, A.G., Hoffmann, M.C., Booske, J., Paoloni, C., Gensch, M., Weightman, P., Williams, G.P. and Castro-Camus, E. The 2017 terahertz science and technology roadmap. *J. Phys. D* **50**, 043001 (2017).
7. Kawada, Y., Yoshioka, K., Arashida, Y., Katayama, I., Takeda, J., and Takahashi, H. Simultaneous acquisition of complex transmittance and birefringence with two counter-rotating, circularly polarized THz pulses. *Opt. Express* **26**, 30420 (2018).
8. Tranter, G. E. Circular Dichroism Spectrometers in *Encyclopedia of Spectroscopy and Spectrometry*, Academic Press, 325-336 (2010).
9. Cheng, G., Choi, W. J., Jang, H-J., Kotov, N. A., and Norris, T. B. Terahertz Time-Domain Polarimetry for Generalized Anisotropic and Chiral Materials. *Terahertz, RF, Millimeter, and Submillimeter-Wave Technology and Applications XII*, 1091704, (2019).
10. Zhou, D. X., Parrott, E. P., Paul, D. J., and Zeitler, J. A. Determination of complex refractive index of thin metal films from terahertz time-domain spectroscopy. *J. Appl. Phys.*, **104**, 053110, (2008).
11. Grischkowsky, D., Keiding, S., Van Exter, M., and Fattinger, C. Far-infrared time-domain spectroscopy with terahertz beams of dielectrics and semiconductors. *JOSA B*, **7**, 2006-2015, (1990).
12. Duvillaret, L., Garet, F., and Coutaz, J. L. A reliable method for extraction of material parameters in terahertz time-domain spectroscopy. *IEEE J. Sel. Top. Quantum Electron.*, **2**, 739-746, (1996).
13. Tomaino, J. L., et al. Terahertz imaging and spectroscopy of large-area single-layer graphene. *Opt. Express* **19**, 141-146, (2011).

14. Van Exter, M., Fattinger, C., and Grischkowsky, D. Terahertz time-domain spectroscopy of water vapor. *Opt. Lett.*, **14**, 1128-1130, (1989).
15. Fischer, B. M., Walther, M., and Jepsen, P. U. Far-infrared vibrational modes of DNA components studied by terahertz time-domain spectroscopy. *Phys. Med. Biol.*, **47**, 3807, (2002).
16. Wu, Q., Litz, M. and Zhang, X-C. Broadband detection capability of ZnTe electro-optic field detectors. *Appl. Phys. Lett.*, **68**, 2924 (1996).
17. Yamada, I., Takano, K., Hangyo, M., Saito, M., and Watanabe, W. Terahertz wire-grid polarizers with micrometer-pitch Al gratings. *Opt. Lett.*, **34**, 274-276, (2009).
18. Collett, E. Stokes Polarization Parameters in *Field Guide to Polarization*, SPIE Press, Bellingham, WA, 12-14 (2005).
19. Aschaffenburg, D.J., Williams, M.R. and Schmuttenmaer, C.A. Terahertz spectroscopic polarimetry of generalized anisotropic media composed of Archimedean spiral arrays: Experiments and simulations. *J. Chem. Phys.* **144**, 174705 (2016).
20. Kanda, N., Konishi, K. and Kuwata-Gonokami, M. Terahertz wave polarization rotation with double layered metal grating of complimentary chiral patterns. *Opt. Express* **15**, 11117 (2007).
21. Zhang, S., Zhou, J., Park, Y.S., Rho, J., Singh, R., Nam, S., Azad, A.K., Chen, H.T., Yin, X., Taylor, A.J. and Zhang, X. Photoinduced handedness switching in terahertz chiral metamolecules. *Nat. Commun.* **3**, 942 (2012).
22. Menzel, C., Rockstuhl, C. and Lederer, F. Advanced Jones calculus for the classification of periodic metamaterials. *Phys. Rev. A* **82**, 053811 (2010).
23. Gjaltema, A., Arts, P.A.M., Van Loosdrecht, M.C.M., Kuenen, J. and Heijnen, J.J. Heterogeneity of biofilms in rotating annular reactors: occurrence, structure, and consequences. *Biotechnol. Bioeng.* **44**, 194(1994).
24. Kocks, U.F., Tomé, C.N., Wenk, H.R. and Beaudoin, A.J. *Texture and anisotropy: preferred orientations in polycrystals and their effect on materials properties*. Cambridge University Press, (2000).
25. Thompson, A.W., Baskes, M.I. and Flanagan, W.F. The dependence of polycrystal work hardening on grain size. *Acta Mater.* **21**, 1017-1028 (1973).
26. Hwang, S.L. and Chen, I.W. Grain size control of tetragonal zirconia polycrystals using the space charge concept. *J. Am. Ceram. Soc.* **73**, 3269 (1990).
27. Aschaffenburg, D.J., Williams, M.R., Talbayev, D., Santavicca, D.F., Prober, D.E. and Schmuttenmaer, C.A. Efficient measurement of broadband terahertz optical activity. *Appl. Phys. Lett.* **100**, 241114 (2012).
28. Rodger, A., Nordén, B. and Nordén, B. *Circular dichroism and linear dichroism*. Oxford University Press, USA, (1997).
29. Kitaev, Y.E., Panfilov, A.G., Smirnov, V.P. and Tronc, P. Why biomolecules prefer only a few crystal structures. *Phys. Rev. E* **67**, 011907 (2003).

30. Gunning, W.J. and Foschaar, J. Improvement in the transmission of iodine-polyvinyl alcohol polarizers. *Appl. Opt.* **22**, 3229(1983).
31. Markelz, A.G., Roitberg, A. and Heilweil, E.J. Pulsed terahertz spectroscopy of DNA, bovine serum albumin and collagen between 0.1 and 2.0 THz. *Chem. Phys. Lett.* **320**, 42 (2000).
32. Weidlich, T., Lindsay, S.M., Rui, Q., Rupprecht, A., Peticolas, W.L. and Thomas, G.A. A Raman study of low frequency intrahelical modes in A-, B-, and C-DNA. *J. Biomol. Struct. Dyn.* **8**, 139 (1990).

Chapter 3

THz Spectroscopy of Bacterial Biofilms

3.1 Chapter introduction

Bacteria are an important part of our world. Almost all life forms on earth including human beings, animals and plants are dependent on beneficial bacteria for their survival or health [1,2,3], while harmful bacteria can cause infections and diseases such as pneumonia [4] and food poisoning [5]. Technologically, because of their ability to quickly grow and their relatively simple structures, bacteria are an ideal platform for the research of molecular biology and biochemistry the results of which can then be applied to more complex organisms [6,7]. Together with many other reasons, it is critical to have a better understanding and manipulation of bacteria. Most bacteria especially in the form of bacterial biofilms, however, have not been fully studied yet [8]. Optical spectroscopy is an indispensable tool in studying different scales of these biological structures and functionalities, but most commonly performed characterizations are very limited to the UV-Vis to near- and mid-IR ranges by the current experimental techniques, such as ultraviolet-visible (UV-Vis) spectroscopy, Fourier-transform infrared spectroscopy (FTIR) and Raman spectroscopy. The far-IR and THz characterization of pristine and complex bacterial biofilms remains a big challenge because of the difficulties from the huge water absorption and the development of the compatible methods. For the last three decades, conventional THz time-domain spectroscopy (THz-TDS) has been the major technique for the THz absorption measurements of relatively simple biomolecules [9,10,11], but due to the lack of polarimetric information, the inaccuracy caused by anisotropy and chirality and the susceptibility to water content, THz-TDS is not suitable for the thorough THz characterization of pristine and complex biofilms which is essential to fully study their collective properties.

In this chapter, I will describe the application of the previously described THz time-domain polarimetry (THz-TDP) to the characterization of bacterial communities. More specifically, THz absorption and THz circular dichroism (TCD) are measured for two species of bacterial biofilms in two kinds of growth media. These measurements can provide useful information about low-energy collective vibrational modes and mesoscale structures of biomolecules in biofilms which cannot be obtained from other existing spectroscopic methods. Advances in sample preparation, experimental techniques and data analysis further enable us to overcome the limitation of water absorption and gain a better understanding of the role of water in biological cells. Together with theoretical studies from molecular dynamics simulation, underlying functions of the specific components can be identified and used for further investigation.

This work was done in collaboration with Prof. Nicholas Kotov's group and Prof. Angela Violi's group in Chemical Engineering and Prof. J. Scott VanEpps' group in Biomedical Engineering. The bacterial biofilms were grown by Usha Kadiyala and Christopher Altheim from VanEpps group, and the measured samples were prepared and modified by Hee-Jeong Jang from Kotov group. The molecular dynamics simulation was performed by Yichun Wang and Paolo Elvati from Violi group. I performed the THz measurements and data processing of the biofilms. A manuscript summarizing the following results is currently in preparation [12].

3.2 Bacterial biofilms and extracellular matrix (ECM)

Bacteria form biofilms on all types of surfaces. These complex biological communities, which often include multiple species, considerably increase the environmental and biological resilience of bacteria, aid their metabolism, and facilitate inter-organism gene exchange [13]. In biofilms, bacterial cells are encapsulated in an extracellular matrix (ECM) [14], a three-dimensional network mainly made of macromolecules such as amyloid fibers, polysaccharides and extracellular DNA (eDNA) as schematically shown in Figure 3-1 (a). ECM not only provides structural support of surrounding cells physically connecting them together via protein fibers as shown in Figure 3-1 (b) and (c), but also plays an important role for signaling between bacterial cells for the purposes of survival, proliferation, differentiation, etc. [15] In addition to the most widely investigated quorum sensing i.e. chemical communication [16], recent studies indicate the potential electrical signaling [17] and electromagnetic (EM) communication [18,19] within bacterial communities, although the details of underlying mechanisms and frequencies are unknown. It is a reasonable hypothesis that the ECM biomolecules function as the signal emitters and receivers and their vibrations mediate the EM communication. Therefore, it is essential to apply optical spectroscopy to biofilms not only to have a better understanding of their ECM components and structures but also to investigate the potential optical communication between biological cells. As presented in Chapter 2 by the experimental results of DNA samples and together with knowledge from existing literature about THz features for biomolecules [9,10,11], the normal vibrational modes of these macromolecules in ECM fall in the high-GHz to low-THz range, hence the THz-TDP developed in Chapter 2 is a great tool to study the absorption and circular dichroism of biofilms.

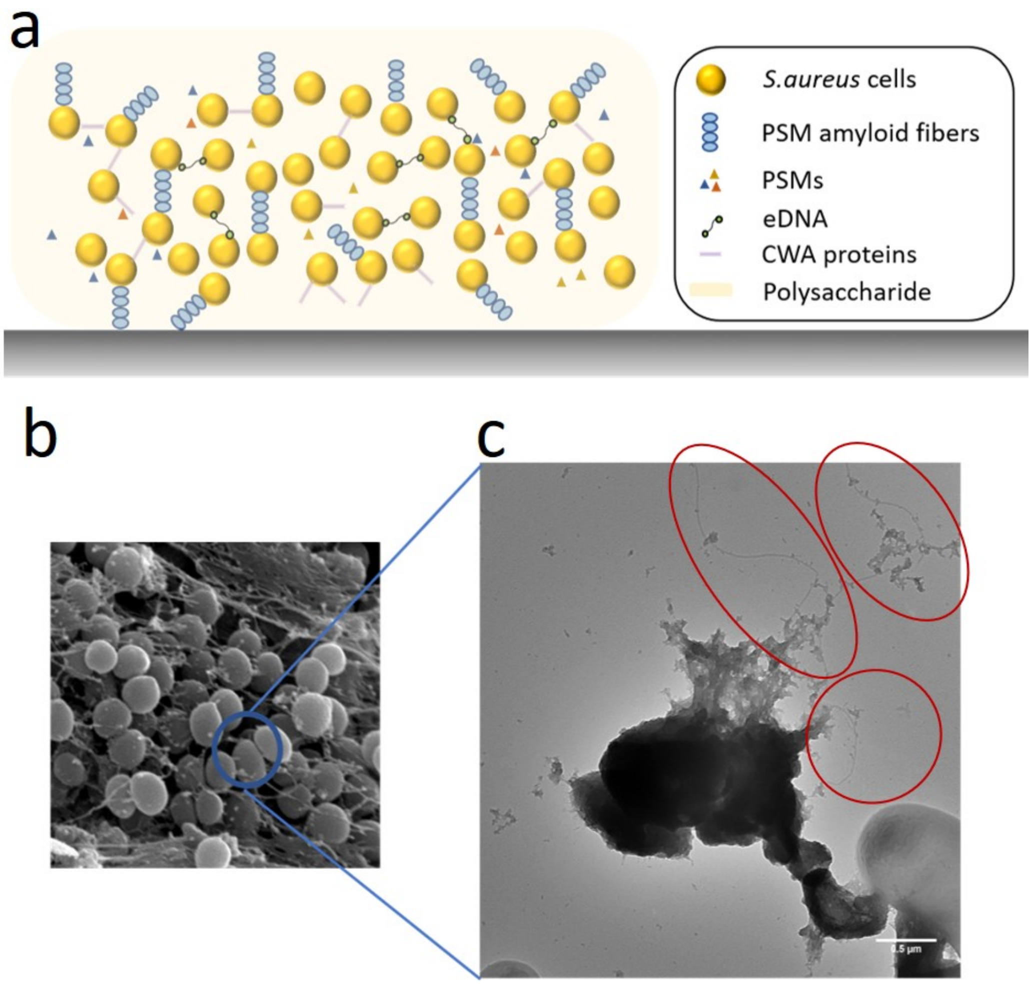

Figure 3-1. Schematic illustration and images of bacterial biofilms and extracellular matrix. (a) schematic illustration of *S. aureus* biofilms. (b) SEM image of *S. aureus* cells in biofilms. (c) TEM of *S. aureus* cells and amyloid fibers highlighted by red circles.

3.3 THz extinction and circular dichroism of freeze-dried biofilms

Biofilms need water and media to survive and grow, so as-grown biofilms are aqueous. This makes the biggest challenge of the THz measurement of these wet biological materials. The absorption coefficient of liquid water is ~220 cm^{-1} at 1 THz and ~350 cm^{-1} at 2 THz [20]. Since the maximum signal-to-noise ratio of our THz time-domain setup is on the order of 10^4, the thickness of media needs to be less than ~100 μm in order to keep the meaningful signals above the noise level. Additionally, the absorption coefficient of normal biomolecules is estimated to be ten to hundred times smaller than that of water, so given that the usual thickness of a pristine biofilm is ~20 μm the absorption signal from water would be dominant and greatly suppress the small signals from biofilms if the amount of media is not well-controlled. Therefore, the overall task is to find an optimum thickness of the sample (biofilm + media) so that the signals from biofilms are measurable while the amount of media is just right enough to keep the biofilms pristine and hydrated; however, it turns out that the precise control of media amount and accurate measurement of the thicknesses of both biofilms and media are experimentally extremely difficult.

To get around this difficulty, we start with freeze-dried biofilms. Freeze-drying, also known as lyophilization, is a dehydration process to remove liquid water from a wet sample by freezing water in low pressure followed by vacuum sublimation [21]. The resulted freeze-dried biofilms may not be very biologically relevant due to the lack of their needed water, but they at least provide some initial important information such as the frequency range of the absorption bands, the magnitudes of absorption and chirality, etc. for the further investigation of much more complicated pristine and wet biofilms.

The sample used for this study is a 5-layer freeze-dried *Bacillus subtilis* (*B. subtilis*) biofilm as a freestanding film attached to an optical aperture. The freeze-dried biofilms are highly inhomogeneous, so the experimental THz setup is the same as the one shown in Figure 2-5 where the sample is fixed and the polarizers are rotated to obtain two sets of electric fields. The THz beam is focused to ~500 μm at the sample position, and the whole THz system is enclosed in a plastic box purged with extra-dry nitrogen to keep the biofilms dry during the measurement.

The experimental results of the THz extinction and circular dichroism spectra are shown in Figure 3-2 (a) and (b), respectively. The extinction is calculated from the measured intensity transmission and is mainly due to absorption. As can be clearly seen from Figure 3-2 (a), there exists an absorption band peaked at 0.8 THz. The very strong absorption above 1.2 THz shows a linearly increasing feature and is due to the remaining or re-absorbed water in the sample. The TCD curve in Figure 3-2 (b) shows a negative peak in the range of 0.8 – 1 THz. These results are reproducible over many different batches of samples indicating the absorption and CD peaks at ~ 0.8 THz indeed come from the biomolecules in the biofilms.

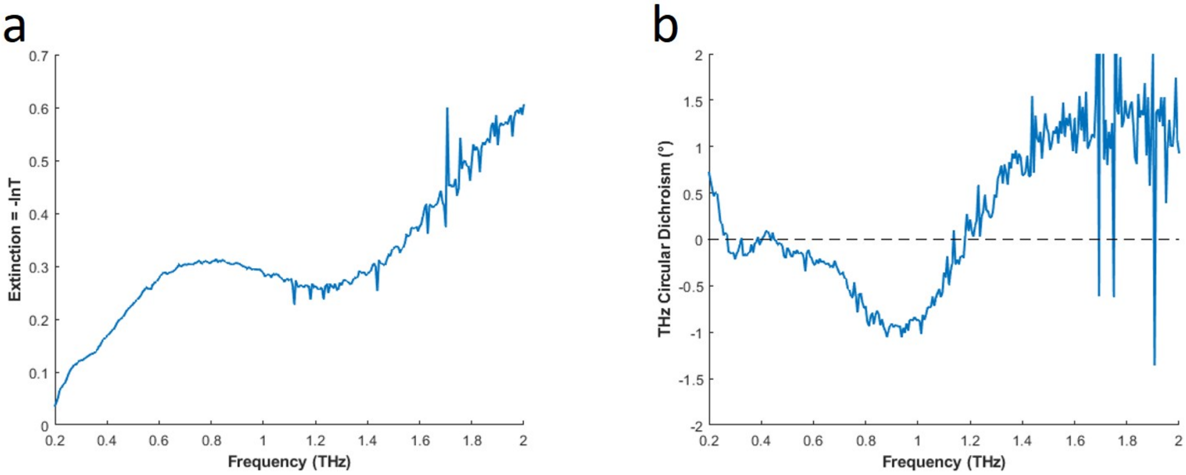

Figure 3-2. Experimental results of freeze-dried biofilms. (a) THz extinction spectrum of a 5-layer *B. subtilis* freeze-dried biofilm. (b) THz circular dichroism spectrum of the same biofilm.

3.4 THz extinction and circular dichroism of wet pristine biofilms

Although the freeze-dried biofilms are simple to measure and produce significant signals of their biomolecules, they are not very biologically relevant because without water these biomolecules may not have the same structures or functions as in aqueous state and the potential effects of water are also totally excluded from the study. Therefore, wet pristine biofilms are still necessary to be characterized to fully understand the ECM functions and the role of water.

3.4.1 Substrate for wet pristine biofilms

Unlike freeze-dried samples, wet biofilms cannot be freestanding and substrates or liquid cells are therefore needed to hold the wet samples. Many substrate materials including glass, high-density polyethylene (HDPE), high-resistivity silicon, and several liquid cell structures either homemade or commercially purchased were tried but failed due to problems of adhesion, hydrophilicity, leakage, thickness control, etc. It turns out that lens tissues as shown in Figure 3-3 (a), which are commonly used in optics labs to clean optical components, are a great substrate for

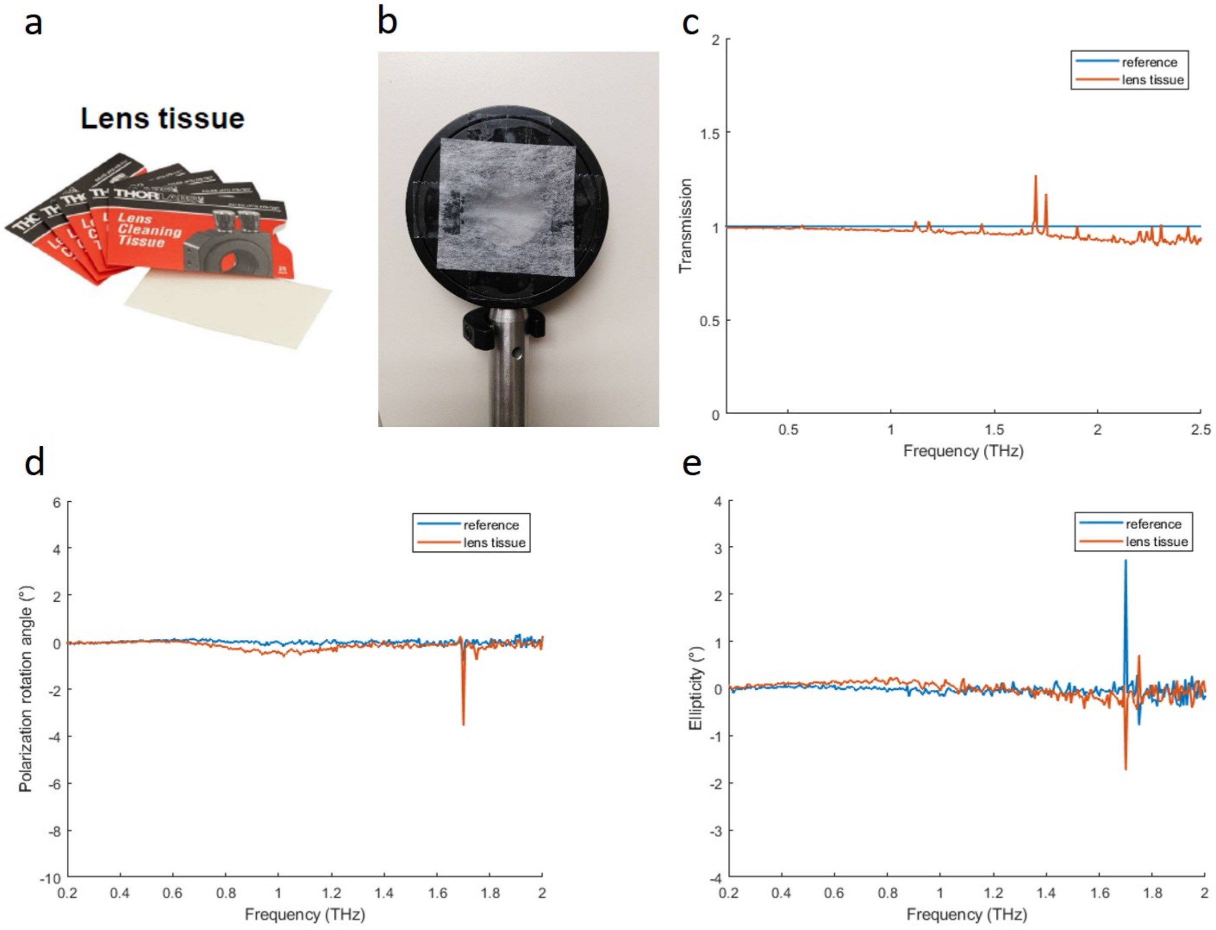

Figure 3-3. Lens tissue as the substrate for wet biofilm samples. (a) Picture of lens tissues commonly used in an optics lab. The picture is from Thorlabs. (b) Picture of a sheet of lens tissue loaded with wet biofilms and mounted onto a holder for the experimental measurement. (c),(d),(e) THz intensity transmission, polarization and ellipticity spectra of a sheet of lens tissue, respectively. The blue curves are the reference without any sample and the red curves are for lens tissue.

our wet biofilm samples: they have almost unity transmission in the THz range as shown in Figure 3-3 (c) and negligible birefringence and chirality shown in Figure 3-3 (d) and (e); their hydrophilicity is relatively high compared to other materials, so wet biofilms can be easily loaded and adhered without moving around during measurement as illustrated in Figure 3-3 (b); the wet media layer formed on the lens tissue is thin enough for the signals from biofilms to be measured with a good signal-to-noise ratio, while hydrated enough to keep bacterial cells wet and pristine. The other big advantage in terms of sample preparation is that biofilms can be directly grown on these lens tissues therefore eliminating the sample transfer process which is usually necessary for other substrate materials.

3.4.2 THz extinction of media and pristine wet biofilms

Two species of biofilms, *Staphylococcus aureus* (*S. aureus*) and *Bacillus subtilis* (*B. subtilis*) in two types of media, PNG (3.3 g/L peptone, 2.6 g/L NaCl, 3.3 g/L glucose) and TSBg (0.6 g/L tryptic soy broth and 1.5 g/L glucose) are grown directly on lens tissues for 5 days, and then pulled out from petri dish right before measurement. *B. subtilis* biofilm does not grow well in PNG media, therefore is not studied, leaving us three kinds of biofilm samples: *S. aureus* in PNG, *S. aureus* in TSBg and *B. subtilis* in TSBg. The control group are the lens tissues soaked in the same PNG and TSBg media but without biofilms and are measured with the same condition as the biofilm samples.

The experimental results of THz extinction are shown in Figure 3-4. Here, the extinction is calculated from the measured intensity transmission by

$$extinction = -\ln T \tag{3.1}$$

where *T* is the THz intensity transmission through the biofilm measured with and without sample. Most of the extinction comes from the sample absorption and a very small part from reflection and scattering, and the resonance-like features should be totally assigned to absorption because the dispersions of both reflection and non-resonant scattering are smooth without peaks. Also, the absolute extinction, which is the product of extinction coefficient and sample thickness, is used since it is difficult to accurately measure the thickness of a wet sample on lens tissue and calculate the corresponding extinction coefficient. However, the exact value of extinction coefficient is not that important for our study; we are more interested in the absorption bands and frequencies associated with the vibrational modes of the biomolecules in these biofilms.

The ingredients of pure PNG media are relatively simple and have no strong THz features, so its THz extinction spectrum as shown in Figure 3-4 (a) is very similar to that of water as linearly increasing with frequency. By comparison, for the spectrum of *S. Aureus* biofilm in PNG as shown in Figure 3-4 (b), it can be clearly seen that there exists a small absorption band in 0.6 – 1 THz above the linearly increasing background of media and this should come from the absorption of biofilm biomolecules. The TSBg media is more complicated than PNG media: as shown in Figure 3-4 (c) its spectrum deviates from that of water and has its own absorption features – the spectrum being flatter – below 1 THz. This makes the comparison between biofilms in TSBg media and pure TSBg media less straightforward, but still, it can be seen from Figure 3-4 (d) and (e) that in the range of 0.6 – 1 THz both *S. Aureus* biofilm in TSBg and *B. Subtilis* biofilm in TSBg have a relatively higher absorption while for other frequencies the spectrum shape remains similar. These results all indicate an absorption band in 0.6 – 1 THz range and are consistent with the previous results from freeze-dried samples.

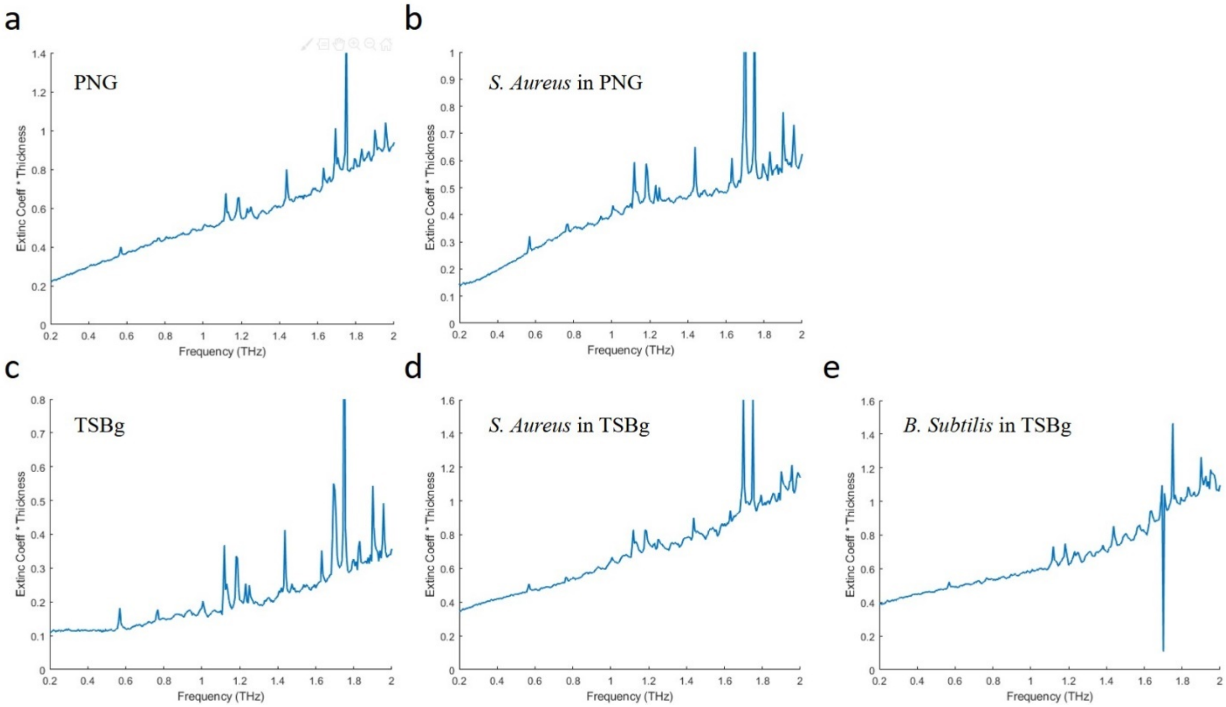

Figure 3-4. THz extinction spectra of media and wet biofilms. (a),(c) Spectra of pure PNG and TSBg media, respectively. (b),(d),(e) Spectra of *S. Aureus* biofilm in PNG media, *S. Aureus* biofilm in TSBg media and *B. Subtilis* biofilm in TSBg media, respectively.

3.4.3 THz relative extinction of pristine wet biofilms

To make the comparison between biofilms and media controls more direct and to locate the absorption frequencies more precisely, it is desirable to eliminate the overwhelming background from the absorption of media. Because there is no good way to accurately measure the separate thicknesses of biofilms and media on lens tissue, it is impossible to extract the individual absorption of pure biofilms from the "biofilm + media" samples. Also, because the thicknesses of biofilm samples and media controls are likely to be different, taking the direct ratio of their experimental transmissions does not cancel out the effect of media. The relative extinction, i.e. the ratio of their total extinctions, however, can achieve this goal.

As mentioned before, the total extinction is the product of extinction coefficient and the sample thickness, therefore for the media control it can be expressed as

$$E_c = extinction\ of\ control = \alpha_m t_{mc} \tag{3.2}$$

where E, α and t stand for total extinction, extinction coefficient and thickness, respectively. The subscripts c and m stand for control and media, respectively.

Correspondingly, under the reasonable assumption that the absorptions of media and biofilm (without media) can be separated and the total absorption is simply their sum, the extinction of a wet biofilm sample (biofilm + media) can be written as

$$E_s = extinction\ of\ sample = \alpha_s t_s = \alpha_m t_{ms} + \alpha_b t_{bs} \tag{3.3}$$

where subscripts s, m and b stand for sample, media and biofilm, respectively.

Then, the relative extinction can be calculated as

$$relative\ extinction = \frac{E_s}{E_c} = \frac{\alpha_m t_{ms} + \alpha_b t_{bs}}{\alpha_m t_{mc}} = \frac{t_{ms}}{t_{mc}} + \frac{t_{bs}}{t_{mc}} \frac{\alpha_b}{\alpha_m} = C_1 + C_2 \frac{\alpha_b}{\alpha_m} \tag{3.4}$$

where $C_1 = \frac{t_{ms}}{t_{mc}}$ and $C_2 = \frac{t_{bs}}{t_{mc}}$ are two constants for a certain sample.

As Eq. (3.4) shows, except for its absolute magnitude, which is again not our concern for this study, the other features of the relative extinction including the dispersive shape and the possible absorption bands are totally independent of the thicknesses of biofilm samples and their media controls. This means that we do not even need to have an accurate measurement of their thicknesses for the investigation of the vibrational modes in biofilms. More importantly, this relative extinction completely eliminates the strong interference of media absorption and presents the properties of biofilms clearly: if the biofilms have no absorption at all, then the relative extinction would be a constant over the whole frequency range; if the biofilms have the same absorption coefficient dispersion as media, then the relative extinction spectrum would be a flat straight line; if there is any resonance mode in biofilms, the biofilm absorption coefficient α_b would deviate from the media absorption coefficient α_m and the relative extinction spectrum would show up a bump or a dip at that resonance frequency. Therefore, any features like an absorption peak in the relative extinction curve must come from the biofilms themselves and must be related to the vibrational modes of their biomolecules.

Using Eq. (3.4), the relative extinction spectra are obtained for the three biofilm samples, *S. Aureus* biofilm in PNG, *S. Aureus* biofilm in TSBg and *B. Subtilis* biofilm in TSBg, as shown in Figure 3-5. The large spikes in these spectra are due to the strong absorption of water vapor surrounding the wet samples. The removal of these spikes requires advanced data processing techniques which is out of the scope of this thesis. Nonetheless, the features from biofilms are expected to be broad due to all kinds of broadening mechanisms in aqueous state, so the very sharp spikes do not affect the overall spectrum shape and the interpretation of the modes in biofilms, at least for the lower frequencies. All spectra have a significant absorption band below 1 THz with a peak centered at 0.6 – 0.7 THz as highlighted by the red arrows in Figure 3-5. For *S. Aureus* biofilms, an additional peak at ~1.2 THz can also be seen in their spectra as highlighted by the green arrows. Overall, these results are consistent with and more significant than the simple comparison between biofilms and media controls in Figure 3-4, and also consistent with the results from freeze-dried biofilms.

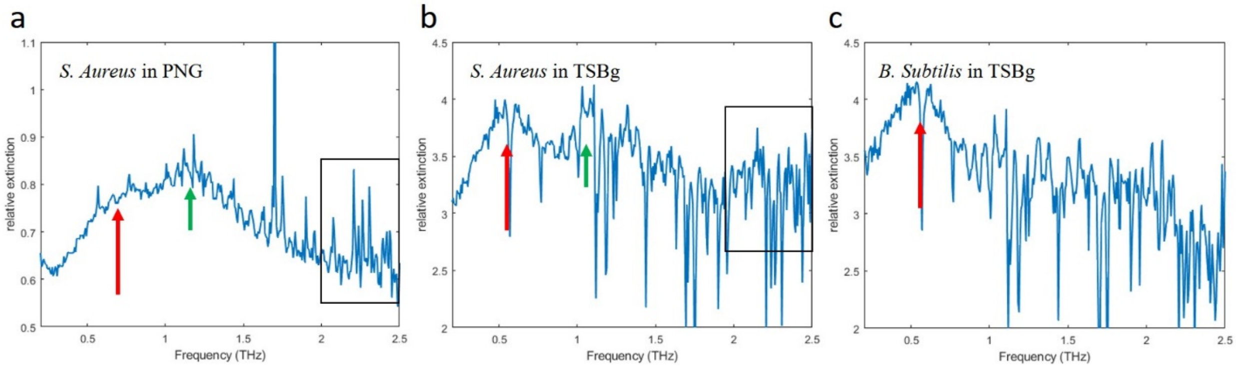

Figure 3-5. Relative extinction spectra of wet biofilms. (a) Spectrum of *S. Aureus* biofilm in PNG media. (b) Spectrum of *S. Aureus* biofilm in TSBg media. (c) Spectrum of *B. Subtilis* biofilm in TSBg media. The magnitudes of the relative extinctions are arbitrary depending on the exact thicknesses of each biofilm and media sample. The red arrows highlight the peaks of the absorption band at 0.6 – 0.7 THz in all samples. The green arrows in (a) and (b) highlight the peaks of the absorption band at ~1.2 THz in *S. Aureus* biofilms. The black rectangles in (a) and (b) highlight the potential absorption band at ~2.3 THz in *S. Aureus* biofilms.

3.4.4 THz circular dichroism of pristine wet biofilms

THz circular dichroism (TCD) measurement is another way to separate the signal of biofilm from the signal of media, because water molecule is achiral while most crucial organic molecules associated with life are chiral and optically active [22]. It should be noted that, although lens tissue works well as the substrate for extinction measurement, it is not as good for TCD measurement of wet biofilms because it is not an easy task to keep the wet lens tissue very flat and small uneven meso-structures on lens tissue surface may cause unwanted TCD artifacts. By careful sample mounting, however, the wet lens tissue can be maintained rather flat during a short measurement period for reasonable and reliable TCD results.

Figure 3-6 shows the TCD spectra of the same three biofilm and two media samples as above. TCD for both PNG and TSBg media are zero over the whole frequency range as shown in Figure 3-6 (a) and (c), meaning the wet lens tissues are mounted flat and the media themselves are not chiral. These two curves are also the reference spectra for the noise level of wet samples in our TCD system and the root-mean-square (RMS) noise is about 0.15° between 0.2 – 2 THz. In contrast, the curves of all biofilm samples have significant TCD peaks with a maximum signal-to-noise ratio (SNR) over 10: *S. Aureus* in PNG has a pretty broad negative TCD band in the range of 0.4 – 1.2 THz with a central peak at ~0.9 THz; *S. Aureus* in TSBg has two negative peaks with a small one at 0.4 THz and a large one at 1.2 THz; the signal from *B. Subtilis* in TSBg is relatively smaller, but still has a discernible negative peak at 0.9 THz. In general, these spectra are consistent with the results from freeze-dried samples in terms of the signs and the frequency range of the TCD peaks.

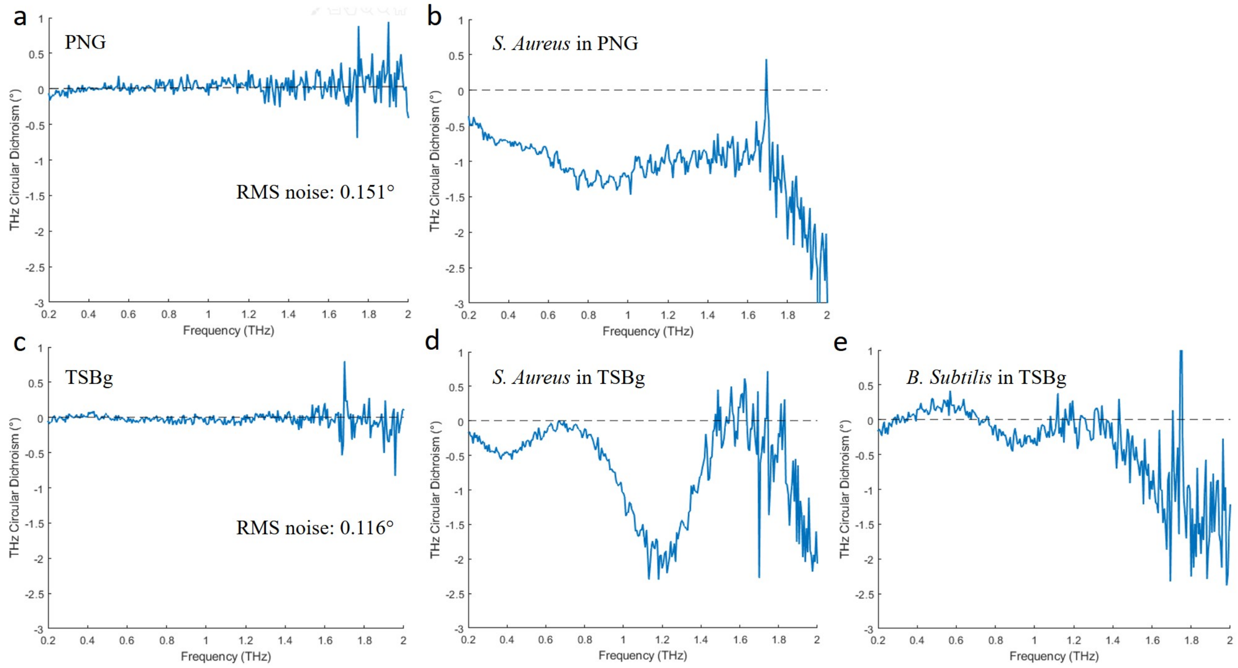

Figure 3-6. THz circular dichroism spectra of media and wet biofilms. (a),(c) Spectra of pure PNG and TSBg media, and the RMS noises are 0.151° and 0.116° respectively, representing the reference and general noise level for our TCD measurements of wet biofilms. (b),(d),(e) Spectra of *S. Aureus* biofilm in PNG media, *S. Aureus* biofilm in TSBg media and *B. Subtilis* biofilm in TSBg media, respectively.

3.4.5 Effects of water on THz signals

Water is critical for biofilms to live and grow, so it is reasonable to expect that water plays an important role to the functions of ECM biomolecules and varying water amount in biofilm samples would lead to different THz signals. To study the role of water, biofilms directly grown on lens tissues for five days are pulled out from petri dish and mounted into the THz chamber which is purged with extra-dry nitrogen gas. Under such conditions wet biofilm samples become dehydrated after 10-20 minutes with water evaporating from the lens tissue. Quick scans are repeated during the whole drying process to obtain the curves for different water content. Each scan takes ~1 minute, and since it is short compared to the whole drying time the water amount can be roughly considered as constant during each measurement. As mentioned above, as a substrate for wet samples, lens tissue is not as good for TCD measurement as for transmission measurement, especially when the sample condition changes. This is because the surface tension changes with varying water amount and may result in different roughness and structures on lens tissue surface causing unexpected changing artifacts for TCD spectra. Therefore, the TCD data for this study is not reliable and not used. Extinction, which is calculated from transmission, however, is not influenced by the lens tissue surface structures, therefore is still valid for this measurement.

Figure 3-7 shows the relative extinction spectra of the same three biofilm samples as above, *S. Aureus* biofilm in PNG, *S. Aureus* biofilm in TSBg and *B. Subtilis* biofilm in TSBg, with varying water amount in them. It is difficult to control and measure the water amount in biofilms on lens tissue at the moment, so the hydration state of these curves are not quantified; however, as the arrow on the right side of Figure 3-7 shows, the biofilms transition from pristine hydrated state as pulled out from petri dish to dehydrated state where a large amount of water is evaporated. As can be seen from the data, for all three biofilms, when they are hydrated the absorption band at 0.6 – 0.8 THz is significant as described in Section 3.4.3. The most hydrated curve in Figure 3-7 (a) for *S. Aureus* biofilm in PNG does not show much feature in this range, and this may be due to that the initial water amount for this sample is too much and the signal from biofilm is totally overwhelmed by water; after the excess water evaporates, the absorption band of biofilm appears on the red and yellow curves. This explanation is consistent and justified by both experimental and simulated results in existing literature [9,23]. With decreasing water amount, the absorption peaks all get smaller, and when the samples are dehydrated the spectra are rather flat and the biofilm features all disappear. This means that water is indeed very important to keep these biofilms functioning normally, and a certain amount of water is needed to induce and enhance the THz signals from biofilms. This may also be a general case for all the hydrated biological systems as discussed in [23] and needs our further investigation.

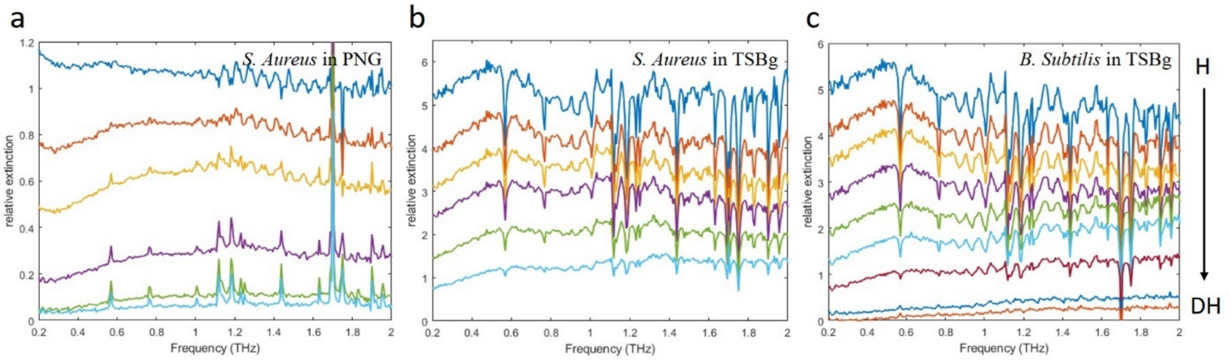

Figure 3-7. Effects of water on THz extinction signals. Spectra of relative extinctions for (a) *S. Aureus* biofilm in PNG media, (b) *S. Aureus* biofilm in TSBg media and (c) *B. Subtilis* biofilm in TSBg media with varying water amount. The arrow on the right side shows the hydration condition of samples. “H” and “DH” stand for hydrated state and dehydrated state, respectively.

3.5 Molecular dynamics (MD) simulation of amyloid proteins and peptides in biofilms

To find out where the experimental THz signals come from in biofilms, theoretical studies are performed using molecular dynamics simulation on the major ECM components of biofilms. Given the importance of amyloid fibers in biofilms highlighted in Figure 3-1 (c) – they provide structural integrity to biofilms [24,25], interact with host [26], detoxify toxic compounds [27], etc. – the simulation is mainly focused on the amyloid proteins or the peptides which form amyloid fibers in extracellular matrix (ECM). The THz absorption spectra of these molecules are presented here. In principle, THz circular dichroism in these biomolecules can also be calculated via MD simulation; however, to date such calculations have not yet been done and remain for future development.

3.5.1 MD simulation of TasA protein in *B. Subtilis* biofilms

For *B. Subtilis* biofilms, the protein that forms amyloid fibers is TasA [24]. Figure 3-8 shows the simulated THz absorption of a TasA protein from *B. Subtilis* in implicit water. The sequence of TasA protein is incomplete and the simulation has some uncertainty, so two different sets of residues are used. Regardless of the slight difference in peak magnitude, the two simulated spectra are almost identical in terms of curve shape and the absorption peak, and is consistent with the experimental data presented in Figure 3-2 and Figure 3-5.

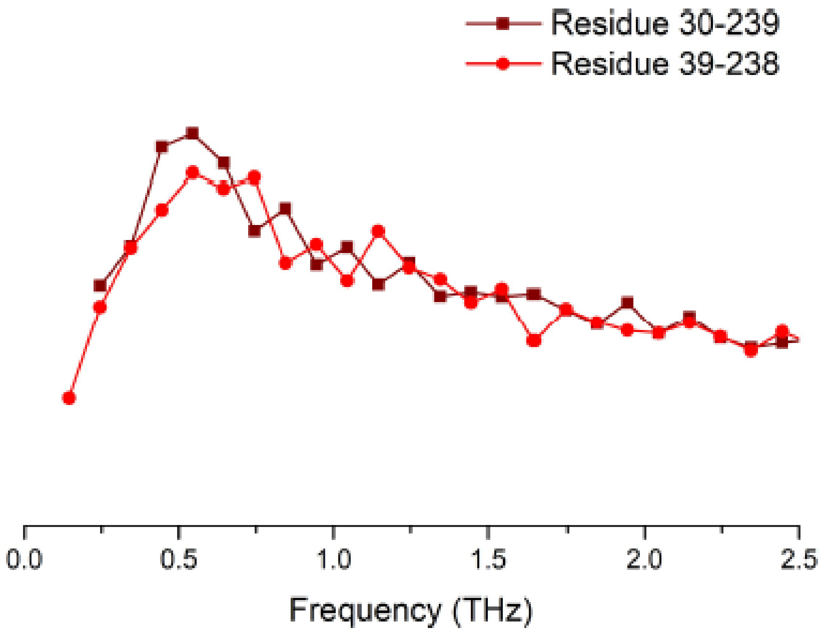

Figure 3-8. THz absorption spectra from molecular dynamics simulation of TasA protein in *B. Subtilis* biofilms with two different sets of residues.

3.5.2 MD simulation of phenol soluble modulin peptides in *S. Aureus* biofilms

For *S. Aureus* biofilms, the amyloid fibers are composed of small peptides called phenol soluble modulins (PSMs) [25], which can be classified into seven groups – PSMα1- α4, PSMβ1, PSMβ2 and δ-toxin – depending on their amino acid sequences [28]. The simulation is only done for PSMα1 now with the results shown in Figure 3-9, and the studies for other PSM peptides are currently underway. The effect of water amount is also studied by incorporating water molecules within 3, 5, and 7 angstroms (Å) of the peptide. As can be seen from Figure 3-9, when water does not exist, there is almost no THz signal from the PSM peptide; with 3 and 5 Å thick water, the absorption signal of the peptide, if there is any, is totally overwhelmed by the strong absorption of water, and the spectra are simply linearly increasing over frequency; when the water thickness is 7 Å, however, two significant absorption peaks from PSMα1 at 0.8 and 2.3 THz appear above the water background. This indicates that a certain amount of water is needed to induce and enhance the signals and functions of such biomolecules in biofilm, and it is consistent with our experimental data and inference discussed in Section 3.4.5 about the role of water in these hydrated biological systems. As for the vibrational modes, the simulated peak at 0.8 THz is also consistent with the experimental results of the pristine wet *S. Aureus* biofilms, except that the absorption band from experiments are much broader due to all kinds of broadening mechanisms in liquid. For the simulated peak at 2.3 THz, it looks like it corresponds to the two small bands between 2.0 and 2.5 THz in Figure 3-5 (a) and (b) highlighted by the black rectangles, but the experimental data is greatly influenced by the large spikes of water vapor at this frequency range and therefore requires more advanced experimental techniques to control the humidity surrounding the biofilms in order to have a more solid comparison.

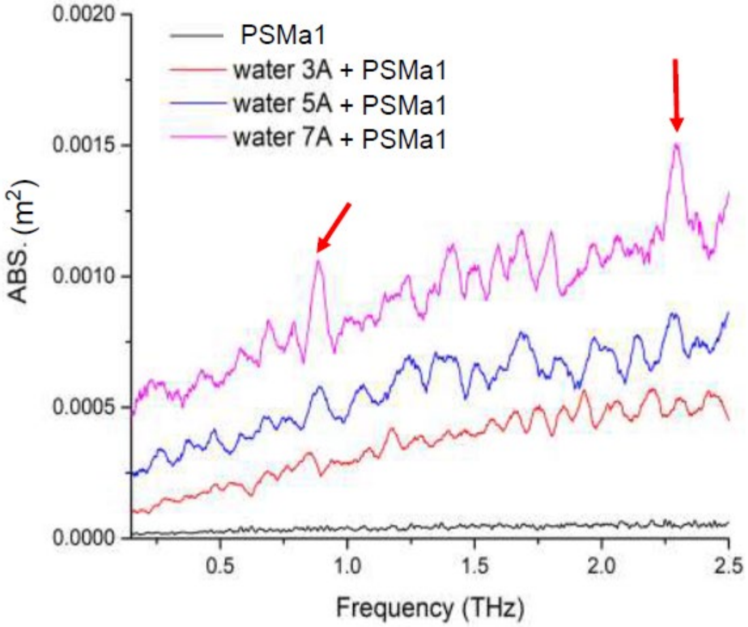

Figure 3-9. THz absorption spectra from molecular dynamics simulation of PSMα1 peptide in *S. Aureus* biofilms with different water amount attached to the peptide. Black curve: PSMα1 only with no water. Red, yellow, pink curves: PSMα1 with 3, 5, 7 angstrom thick water attached, respectively.

3.6 Summary

THz time-domain polarimetry has been used for the characterization of two species of complex bacterial communities, *B. Subtilis* and *S. Aureus* biofilms, in both freeze-dried and pristine wet states. Freeze-drying, as an easier approach in sample preparation, can provide some initial basic understanding of biofilms, while pristine wet samples which requires more careful selection of substrate and sample preparation gives additional important information including multiple absorption bands and the critical role of water in hydrated biological systems. The MD simulations of the components of amyloid fibers in both *B. Subtilis* and *S. Aureus* biofilms are largely consistent with the experimental data. All these results are the potential evidence that amyloid fibers are the major contribution of the THz absorption and circular dichroism signals in biofilms and could provide useful guidance for the further investigation of the potential electromagnetic communication between biological cells.

Reference

1. Salyers, A. A., Gupta, A., and Wang, Y. Human intestinal bacteria as reservoirs for antibiotic resistance genes. *Trends in microbiology*, **12**, 412-416, (2004).
2. Fang, H., Kang, J., and Zhang, D. Microbial production of vitamin B_{12}: a review and future perspectives. *Microb. Cell Fact.*, **16**, 15, (2017).
3. Davison, J. Plant beneficial bacteria. *Bio/technology*, **6**, 282, (1988).
4. Trouillet, J. L., Chastre, J., Vuagnat, A., Joly-Guillou, M. L., Combaux, D., Dombret, M. C., and Gibert, C. Ventilator-associated pneumonia caused by potentially drug-resistant bacteria. *Am. J. Respir. Crit. Care Med.*, **157**, 531-539, (1998).
5. Le Loir, Y., Baron, F., and Gautier, M. Staphylococcus aureus and food poisoning. *Genet Mol Res*, **2**, 63-76, (2003).
6. Roberts, I. S. The biochemistry and genetics of capsular polysaccharide production in bacteria. *Annual Reviews in Microbiology*, **50**, 285-315, (1996).
7. Jetten, M. S., Niftrik, L. V., Strous, M., Kartal, B., Keltjens, J. T., and Op den Camp, H. J. Biochemistry and molecular biology of anammox bacteria. *Crit. Rev. Biochem. Mol. Biol.*, **44**, 65-84, (2009).
8. Stewart, E. J. Growing unculturable bacteria. *J. Bacteriol.*, **194**, 4151-4160, (2012).
9. Markelz, A. G., Roitberg, A., and Heilweil, E. J. Pulsed terahertz spectroscopy of DNA, bovine serum albumin and collagen between 0.1 and 2.0 THz. *Chem. Phys. Lett.*, **320**, 42-48, (2000).
10. Markelz, A., Whitmire, S., Hillebrecht, J., and Birge, R. THz time domain spectroscopy of biomolecular conformational modes. *Phys. Med. Biol.*, **47**, 3797, (2002).
11. Nagel, M., Haring Bolivar, P., Brucherseifer, M., Kurz, H., Bosserhoff, A., and Büttner, R. Integrated THz technology for label-free genetic diagnostics. *Appl. Phys. Lett.*, **80**, 154-156, (2002).
12. Wang, Y., Cheng, G., Elvati, P., Jang, H-J., Kadiyala, U., Altheim, C., VanEpps, J. S., Violi, A., Norris, T. B., and Kotov, N. A. THz Spectroscopy and Computational Study of Amyloid Proteins from Bacterial Biofilms. *in preparation*
13. Costerton, J. W., Stewart, P. S., and Greenberg, E. P. Bacterial biofilms: a common cause of persistent infections. *Science*, **284**, 1318-1322, (1999).
14. Hay, E. D. (Ed.). *Cell biology of extracellular matrix*. Springer Science & Business Media, (2013).
15. Hynes, R. O. The extracellular matrix: not just pretty fibrils. *Science*, **326**, 1216-1219, (2009).
16. Waters, C. M., and Bassler, B. L. Quorum sensing: cell-to-cell communication in bacteria. *Annu. Rev. Cell Dev. Biol.*, **21**, 319-346, (2005).

17. Humphries, Jacqueline, et al. Species-independent attraction to biofilms through electrical signaling. *Cell*, **168**, 200-209, (2017).
18. Reguera, G. When microbial conversations get physical. *Trends in microbiology*, **19**, 105-113, (2011).
19. Scholkmann, F., Fels, D., and Cifra, M. Non-chemical and non-contact cell-to-cell communication: a short review. *Am. J. Transl. Res.*, **5**, 586, (2013).
20. Xu, J., Plaxco, K. W., and Allen, S. J. Absorption spectra of liquid water and aqueous buffers between 0.3 and 3.72 THz. *J. Chem. Phys.*, **124**, 036101, (2006).
21. Franks, F. Freeze-drying of bioproducts: putting principles into practice. *Eur. J. Pharm. Biopharm.*, **45**, 221-229, (1998).
22. Bonner, W. A. The origin and amplification of biomolecular chirality. *Orig. Life Evol. Biospheres*, **21**, 59-111, (1991).
23. Xu, Jing, et al. Terahertz circular dichroism spectroscopy: a potential approach to the in situ detection of life's metabolic and genetic machinery. *Astrobiology*, **3**, 489-504, (2003).
24. Romero, D., Aguilar, C., Losick, R., and Kolter, R. Amyloid fibers provide structural integrity to Bacillus subtilis biofilms. *Proc. Natl. Acad. Sci. U.S.A.*, **107**, 2230-2234, (2010).
25. Schwartz, K., Syed, A. K., Stephenson, R. E., Rickard, A. H., and Boles, B. R. Functional amyloids composed of phenol soluble modulins stabilize Staphylococcus aureus biofilms. *PLOS Pathog.*, **8**, e1002744, (2012).
26. Schwartz, K., and Boles, B. R. Microbial amyloids–functions and interactions within the host. *Current opinion in microbiology*, **16**, 93-99, (2013).
27. Shahnawaz, M., and Soto, C. Microcin amyloid fibrils A are reservoir of toxic oligomeric species. *J. Biol. Chem.*, **287**, 11665-11676, (2012).
28. Wang, Rong, et al. Identification of novel cytolytic peptides as key virulence determinants for community-associated MRSA. *Nat. Med.*, **13**, 1510, (2007).

Chapter 4

Chiral Kirigami Optics for THz Polarization Modulation and THz Circular Dichroism Spectroscopy

4.1 Chapter introduction

Terahertz circular dichroism (TCD) offers spectroscopic capabilities for understanding mesoscale chiral architecture and low-energy vibrations of macromolecules in (bio)materials [1-5]. Even though the THz time-domain polarimetry developed in Chapter 2 is able to provide information about circular dichroism in the THz range, it still has some serious limitations: 1) it requires a sequence of measurements which may take at least a couple of minutes to achieve high enough signal-to-noise ratio, therefore this sequential procedure is not applicable to quickly changing or decaying samples such as chemical solutions/reactions or rapidly drying biomaterials; 2) also due to this sequential nature, it is difficult to integrate this method with high-frequency instrument such as modulators and lock-in amplifiers for very high-sensitivity measurement, therefore it is also not applicable to the materials with very small chiral signals; 3) the polarimetry requires the measurement of electric fields to completely determine the Jones matrix and the derived optical properties, hence it cannot be extended to shorter wavelengths where electric field is difficult to be obtained. The solution to these problems is to directly use a THz circular dichroism spectrometer where a THz polarization modulator can modulate the input THz polarization in real time. However, the lack of such dynamic polarization modulators comparable to polarization optics for other parts of electromagnetic spectrum impedes proliferation of TCD spectroscopy [6-11].

In this chapter, I will show that tunable optical elements fabricated from patterned plasmonic sheets with periodic kirigami cuts make possible polarization modulation of THz radiation under application of mechanical strain. A herringbone pattern of microscale metal stripes enables dynamic range of polarization rotation and ellipticity modulation up to 80° and 40° respectively over thousands of cycles. Upon out-of-plane buckling, the plasmonic stripes function as reconfigurable semi-helices of variable pitch aligned along the THz propagation direction. Several biological materials, exemplified by an elytron of *Chrysina gloriosa*, revealed distinct TCD fingerprints associated with the helical substructure in the biocomposite. Analogous kirigami modulators will also enable other applications in THz optics, such as polarization-based terahertz imaging, line-of-sight telecommunication, information encryption and space exploration.

This work was done in collaboration with Prof. Nicholas Kotov's group in Chemical Engineering. The device design and fabrication and its mechanical characterization were performed by Won Jin Choi from Kotov group. I performed the optical measurements, the resulting data analysis and the major part of the optical simulation. The results of this work are published in *Nature Materials* in 2019 [12].

4.2 Design and fabrication of kirigami modulators

Kirigami, the Japanese art of paper cutting (closely related to the Chinese art of jianzhi), presents a powerful tool to create complex and tunable three-dimensional (3D) geometries from simple 2D cut patterns, which can be scaled across many orders of magnitude to yield macro- to nanoscale structures [13-18]. The ability to achieve out-of-plane deformations and designed 3D shapes, the robustness of the patterns under cyclic reconfiguration and the manufacturing simplicity of kirigami structures together promise untapped possibilities for the efficient modulation of THz optical beams.

The substrate of the kirigami modulators in this study are made from parylene – a stiff polymer (Young's modulus $E = 2.8$ GPa) with high transparency across the THz spectrum [19]. As shown in Figure 4-1 (a), parylene sheets are patterned with straight cuts in a face-centered rectangular lattice. This 2D pattern transforms upon stretching into an array of alternating convex and concave out-of-plane surfaces due to buckling. Our function-defining structural feature is a gold herringbone pattern with D_n symmetry (chiral dihedral point group) [20] deposited on parylene sheets in registry with kirigami cuts to generate plasmonic resonance for incoming light demonstrated in Figure 4-1 (b). When buckled, the double-patterned structures are transformed and topologically equivalent to 3D chiral helices as in Figure 4-1 (d), which enable strong and tunable polarization rotation with real-time modulation capability.

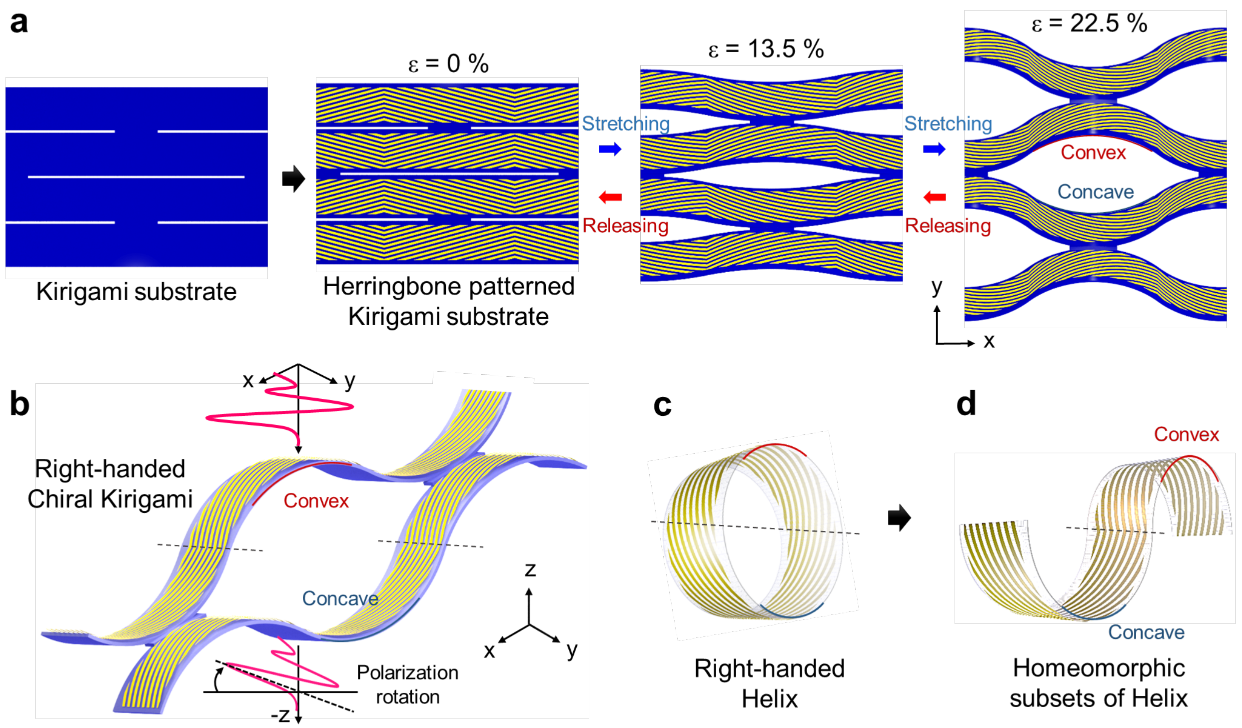

Figure 4-1. Schematic of chiral kirigami topology. (a) Herringbone structured Au strips are deposited on the kirigami substrate. This chiral kirigami topology can tune the polarization rotation angle and ellipticity by mechanical force. (b) Stretched chiral kirigami metamaterial that is topologically equivalent to helix structure. (c) Standard right-handed helix structure whose outside is covered with slanted striations. (d) Geometric structure displaying homeomorphic subsets of right-handed helix. Adapted from Ref [12].

The detailed dimensions of the kirigami design are shown in Figure 4-2. The thickness of parylene substrate is set to ~6 μm and the deposited chromium and gold are ~5 nm and ~45 nm respectively. In order to induce the plasmonic resonance in THz range, the unit cell size is comparable to the THz wavelength with a 600 μm width (W_{unit}) and a 210 μm height (H_{unit}). The length (L_{cut}) and height (H_{cut}) of each cut is 500 μm and 5 μm, respectively. The horizontal and vertical spacings between cuts are set to 100 μm. The width of each Au strip is set to 5 μm. Additionally, the slant angle (φ) is defined as the angle between the cut direction and the longer axial direction of the Au strips as shown in Figure 4-2 (b), and it can be used to adjust the lengths of Au strips therefore tuning the resonant frequencies.

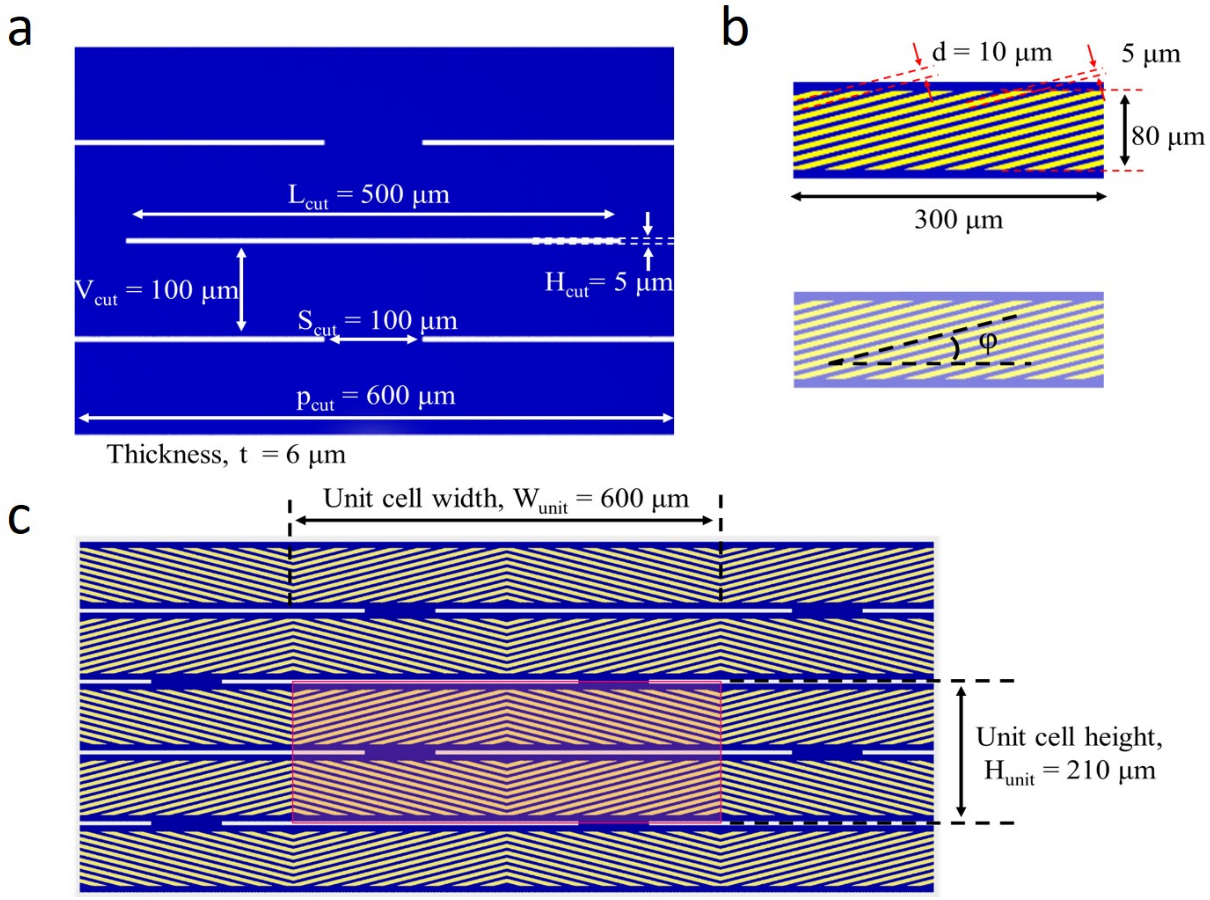

Figure 4-2. Design dimensions and definition of slant angle in chiral kirigami pattern. (a) Top view of kirigami cut pattern. (b) Detailed view of single unit of slanted Au strips. The slant angle (φ) is defined as angle between longitudinal direction of cut and Au strip. (c) Top view image of aligned kirigami cut pattern and Au herringbone pattern. Red box indicates the unit cell of this double pattern. Adapted from Ref [12].

The strict control over the handedness of kirigami sheets is achieved by adding stress concentrators at the end of the kirigami patterns, as shown in Figure 4-3. These stress concentrators are made of thin gold films and this area is more likely to acquire a convex shape under stress due to the residual stress in the film. With these stress concentrators, a kirigami modulator can only be either left-handed or right-handed, while without them a single modulator can be mixed with both L- and R-domains which greatly reduces its overall performance. Moreover, this asymmetric pattern of stress concentrators breaks the symmetry of the 2D kirigami structures and enables very large out-of-plane deformation which is essential for the optimum optical response and tunability.

The fabrication of the chiral kirigami modulators is completed by integrating the kirigami sheet with a compact linear stage controlled by a piezo motor (U-521 PILine, Physik Instrumente)

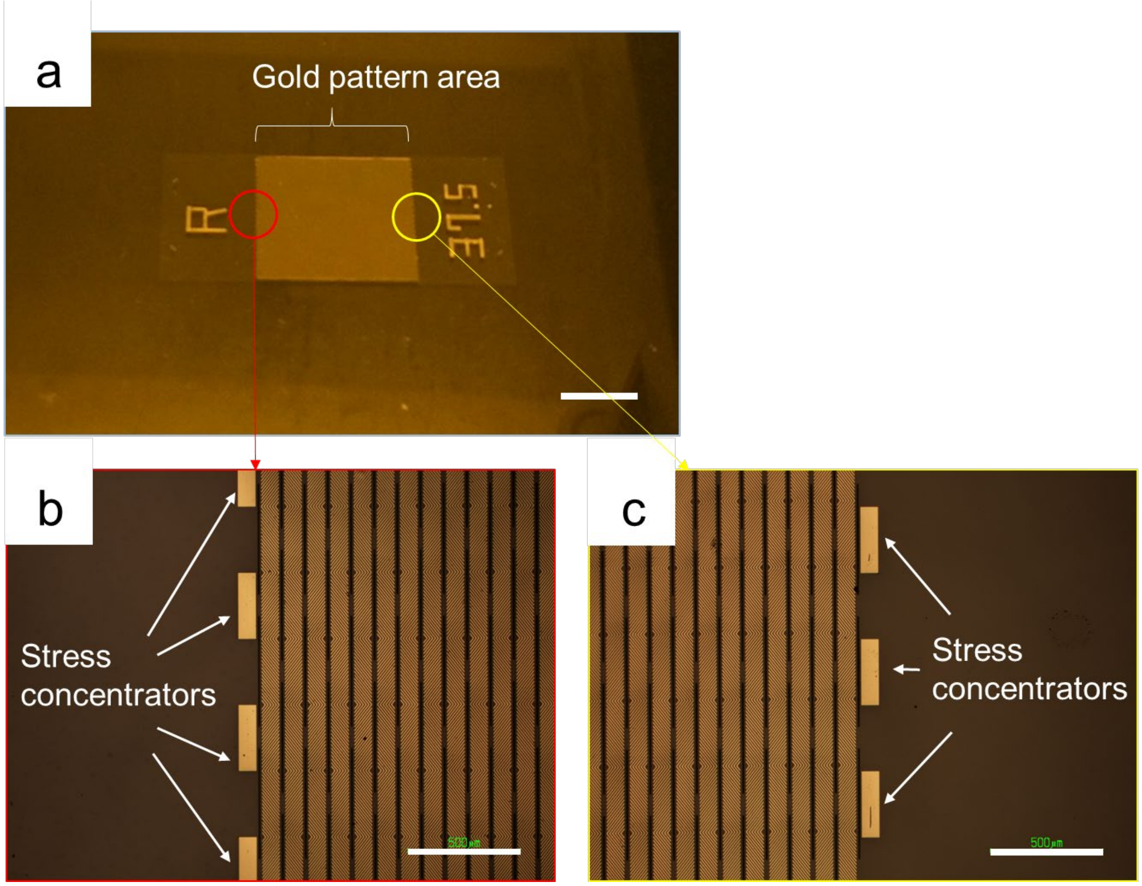

Figure 4-3. Stress concentrators for the handedness control of kirigami sheets. (a) Photo image of kirigami substrate. Scale bar is 1 cm. (b) and (c) show the optical microscope images of the end of the pattern in the red and yellow circled area, respectively. White arrows indicate the asymmetric set of stress concentrators. Scale bars in (b) and (c) are 500 µm. Adapted from Ref [12].

for the application of a well-controlled strain (ε), as shown in Figure 4-4 (a). This piezo controller can be programmed with very high spatial precision of 0.1 µm ($\varepsilon = 0.001\%$). The applied strain values of 2.3, 4.5, 9.0, 13.5, 18, 22.5 % in the measurements presented below are calculated from stretching distances of 0.2, 0.4, 0.8, 1.2, 1.6, 2.0 mm, respectively.

4.3 Experimental setup and data of single kirigami modulators

4.3.1 Optical setup and sample mounting orientations

The experimental setup for the THz characterization of chiral kirigami modulators, as shown in Figure 4-4 (b), is similar to the THz time-domain polarimetry (THz-TDP) described in Chapter 2, except that here collimated instead of focused THz beam is incident onto the kirigami

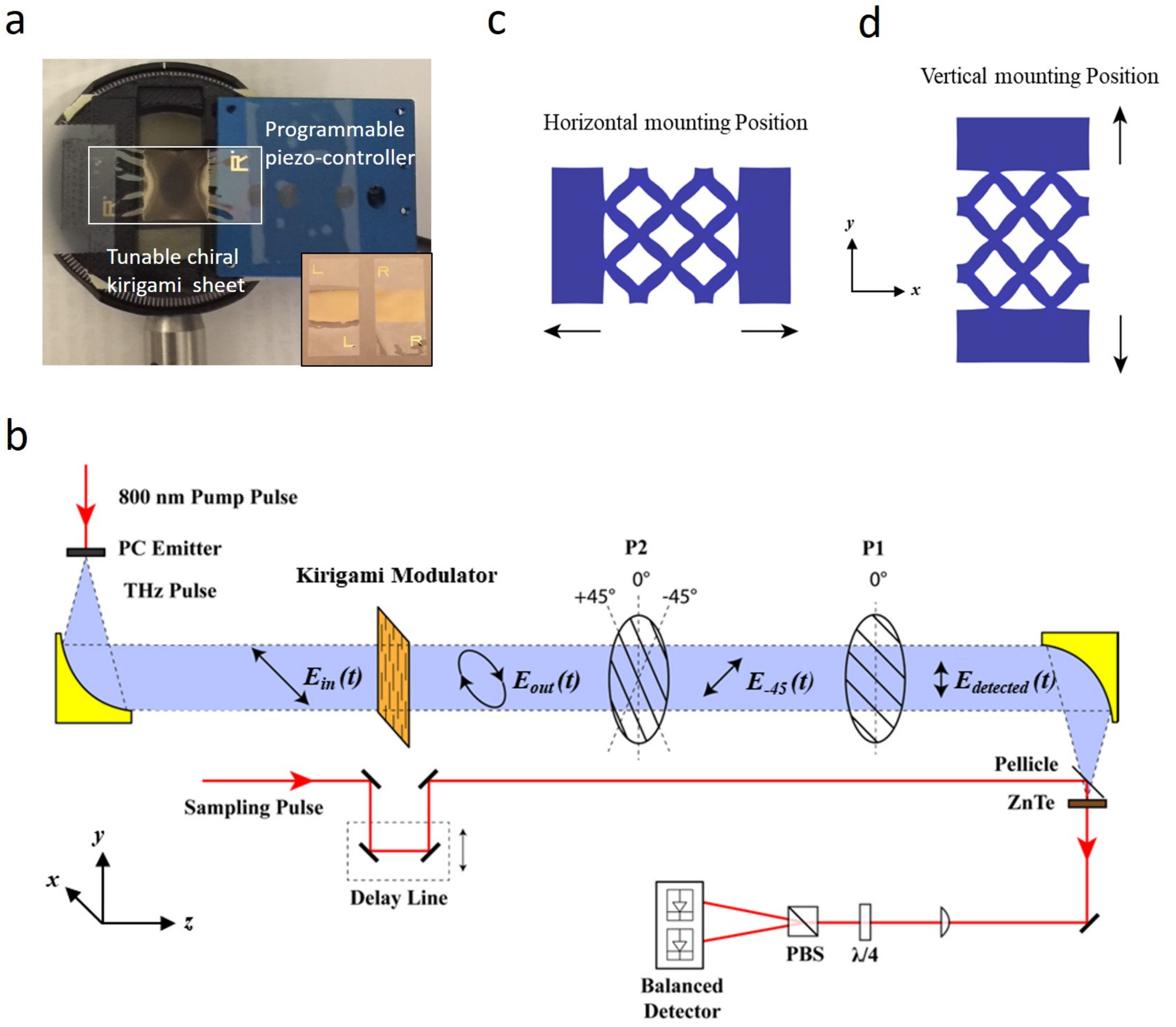

Figure 4-4. Experimental setup for the THz characterization of chiral kirigami modulators. (a) Kirigami sheet mounted on the 3D printed rotatable optical holder with a piezoelectric controller. Inset, photo image of left- and right-handed chiral kirigami substrate. The yellow shiny region is the herringbone-patterned Au zone. (b) Schematic of THz-TDP setup for the kirigami modulator measurements. (c) and (d) show the definitions of horizontal (H) and vertical (V) mounting positions. The thick black arrows indicate the stretching directions actuated by the piezo controller horizontally for (c) and vertically for (d). Adapted from Ref [12].

samples because of their much larger unit cell size and functioning area. Also, the THz field generated by the photoconductive (PC) emitter is measured to have a high degree of linear polarization with an ellipticity angle below 0.3° (shown as the dash-dot lines in Figure 4-6 to Figure 4-8) which is negligible compared to the ellipticity induced by the chiral kirigami modulators, and it is confirmed that use of a linear polarizer immediately after the emitter make no further improvement in linearity, so it is removed in this measurement to save some space on the optical table. In general, the emitter is fixed at an orientation such that the generated THz polarization is horizontal to the optical table (defined here as the x axis). The first polarizer (P1) is placed in front of the ZnTe crystal and its transmission direction (perpendicular to the wire grid orientation) is fixed vertical to the optical table (defined as the y axis). The ZnTe crystal and the sampling pulses are oriented to give the maximum electro-optic sensitivity along y direction. The second polarizer (P2) is placed between the sample and the first polarizer and is rotated to three different orientations (0°, +45° and -45°) to construct the electric field as before.

Since our kirigami pattern is only C_2-symmetric, measurements must be performed for two perpendicular polarizations, i.e. horizontally and vertically polarized THz waves, incident on the kirigami to fully characterize the kirigami sheet's in-plane optical properties, especially circular dichroism [22]. This is accomplished by rotating the samples by 90° because the kirigami structure is highly periodic therefore satisfying the prerequisites of the first THz-TDP described in Section 2.4 for the generalized homogeneous materials. The kirigami modulator is attached to a rotation mount (RSP1, Thorlabs), so the transmitted waves can be measured in both horizontal and vertical orientations (simple rotation by 90°). Here, the horizontal and vertical mounting orientations are defined as follows: horizontal - stretching direction is along with x direction as indicated in Figure 4-4 (c); vertical - stretching direction is along with y direction in Figure 4-4 (d).

There are four possible configurations for the measurements: the kirigami modulator may be designed for either right- or left-handedness, and the modulators may be mounted horizontally or vertically relative to the input linear polarization. The abbreviation used in the following sections is as follows: "HL" for horizontally mounted left-handed kirigami modulator, "HR" for horizontally right-handed, "VL" for vertically left-handed, and "VR" for vertically right-handed.

4.3.2 An example of raw THz-TDP data for kirigami modulators

As an example of the raw data measured directly from THz-TDP setup, Figure 4-5 (a) shows the three time-domain THz electric fields (i.e. with the polarizer P2 rotated to +45°, -45° or 0° position) of a horizontally mounted left-handed (HL) kirigami sample with gold herringbone pattern at $\varphi = 30°$ and stretched with $\varepsilon = 22.5\%$. Figure 4-5 (b) are the electric fields for the same sample under the same measurement conditions but rotated to vertical position (VL). Figure 4-5 (c) and (d) show zoomed views near zero-time delay, and the signals of the 0° component and the appearance of multi-cycle waves compared to single-cycle input pulse (especially for the 0°

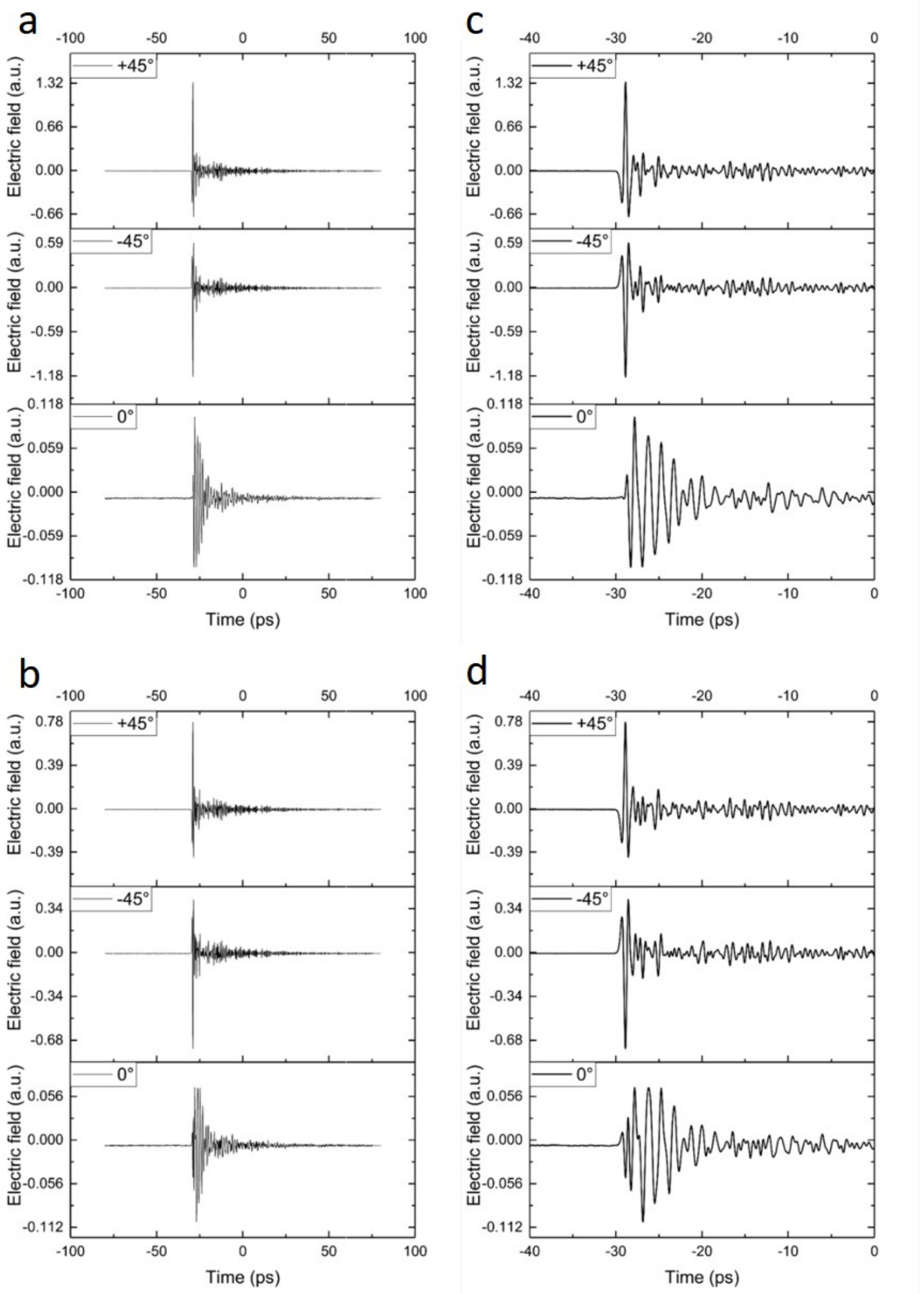

Figure 4-5. An example of raw THz-TDP data of a left-handed (L-) kirigami sample with 30° slant angle ($\varphi = 30°$) and stretched with $\varepsilon = 22.5\%$. (a) Transmitted electric fields of horizontally and (b) vertically mounted sample over the whole scan range. (c) and (d) are zoomed views on the main peaks (near zero time delay) of (a) and (b), respectively. Adapted from Ref [12].

component) are the clear evidence of polarization rotation and THz resonances of chiral kirigami structures. These raw data are then processed following the same mathematical procedures described in Chapter 2 to calculate the electric field transmittances, polarization angles and circular dichroism.

4.3.3 Experimental results of varying slant angle

The detailed data for a single kirigami modulator with three different slant angles of the herringbone patterns (φ = 45°, 30°, 15°) are presented in Figure 4-6 to Figure 4-8. These include the spectra of the magnitudes of the transmission coefficients ($t_{xx}, t_{xy}, t_{yx}, t_{yy}$), the polarization rotation (θ) and ellipticity angles (η) for both horizontal and vertical mountings, and the spectra of the resulting circular dichroism angles.

First, as described in Chapter 2 and mathematically represented by Eq. (2.27), for a general material with an C_2 symmetry with respect to its x axis which is the case for our kirigami structures, the chiral properties can be completely determined by the off-diagonal components of the Jones matrix t_{xy} or t_{yx} which should be equal in magnitude, while the anisotropic properties can be totally determined by the diagonal components t_{xx} and t_{yy}. From the experimental data, we can clearly see that the magnitudes of the diagonal components t_{xx} and t_{yy} are different hence there exists anisotropy in our kirigami structures. On the other hand, the off-diagonal components t_{xy} and t_{yx} are almost identical in terms of the magnitudes and spectrum shapes for each slant angle, because chirality is rotationally invariant and independent of orientation. Moreover, the chirality represented by t_{xy} and t_{yx} increases with applied mechanical strain.

To characterize the modulation effects of our kirigami modulators on THz electric field, the polarization rotation (θ) and ellipticity angles (η) are calculated. As expected, θ and η increase with strain, and kirigami structures with left- and right-handed herringbone patterns exhibit THz responses that are nearly identical but with opposite signs, i.e. enantiomeric. Furthermore, the slant angle determines the positions of the main resonance peaks, which are observed at 0.81 THz for $\varphi = 45°$, 0.62 THz for $\varphi = 30°$ and 0.41 THz for $\varphi = 15°$. For herringbone patterns with φ of 30°, the maximum values of θ and η reach as high as 80° and 40° and are close to those of a half-waveplate and a quarter-waveplate, respectively.

Note that due to anisotropy the magnitudes of θ and η depend on the in-plane orientation, so THz circular dichroism (TCD) spectra are further calculated to explicitly characterize the

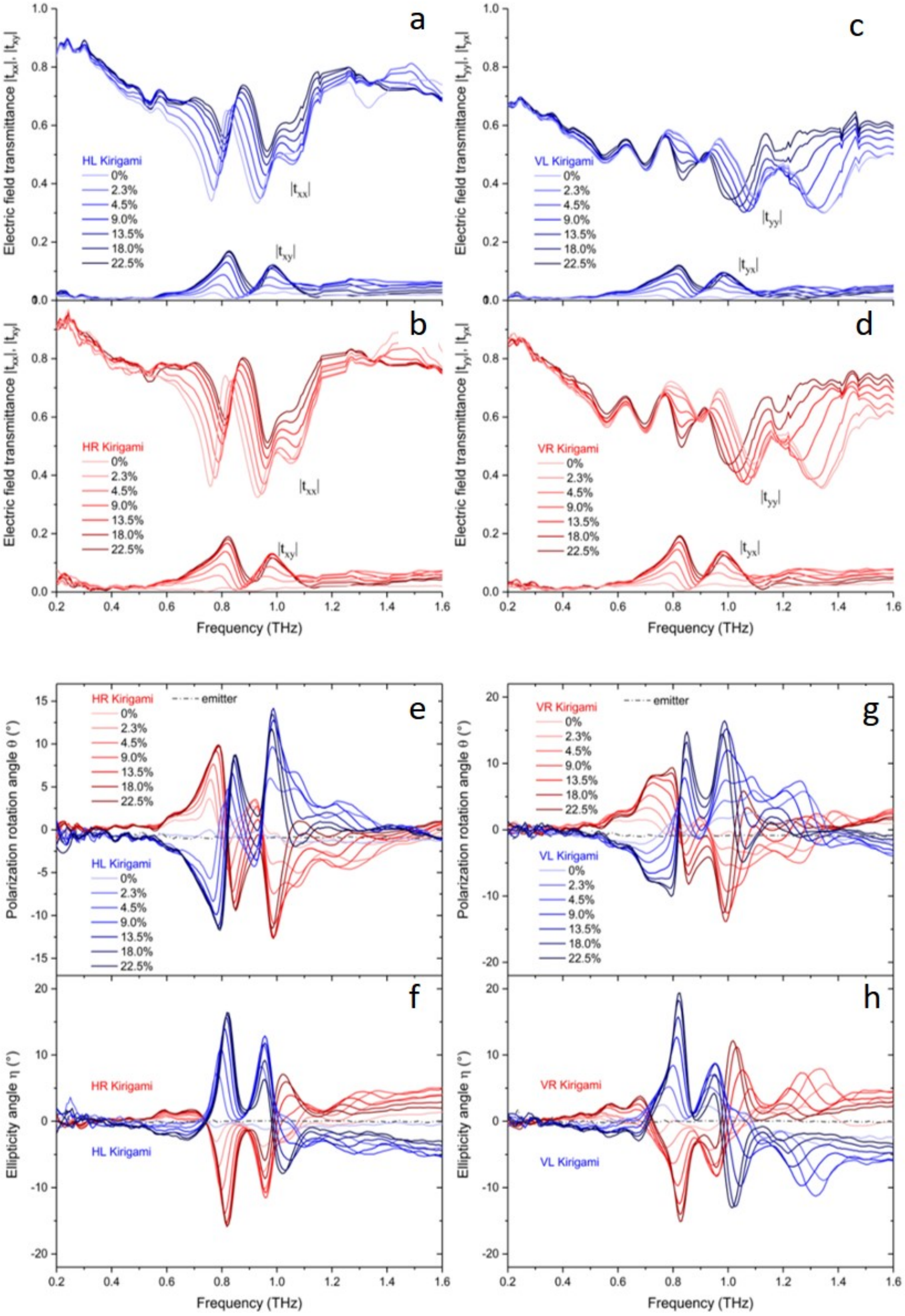

Figure 4-6. Experimental data for kirigami modulators with slant angle of 45°. (a) – (d) the magnitudes of four transmittance coefficients. (e) polarization rotation angle and (f) ellipticity angle induced by the samples mounted horizontally. (g) polarization rotation angle and (h) ellipticity angle induced by the samples mounted vertically. Blue and red curves are for left-handed (L) and right-handed (R) samples respectively. The strains applied are given in the legends and the same for all the subfigures. Adapted from Ref [12].

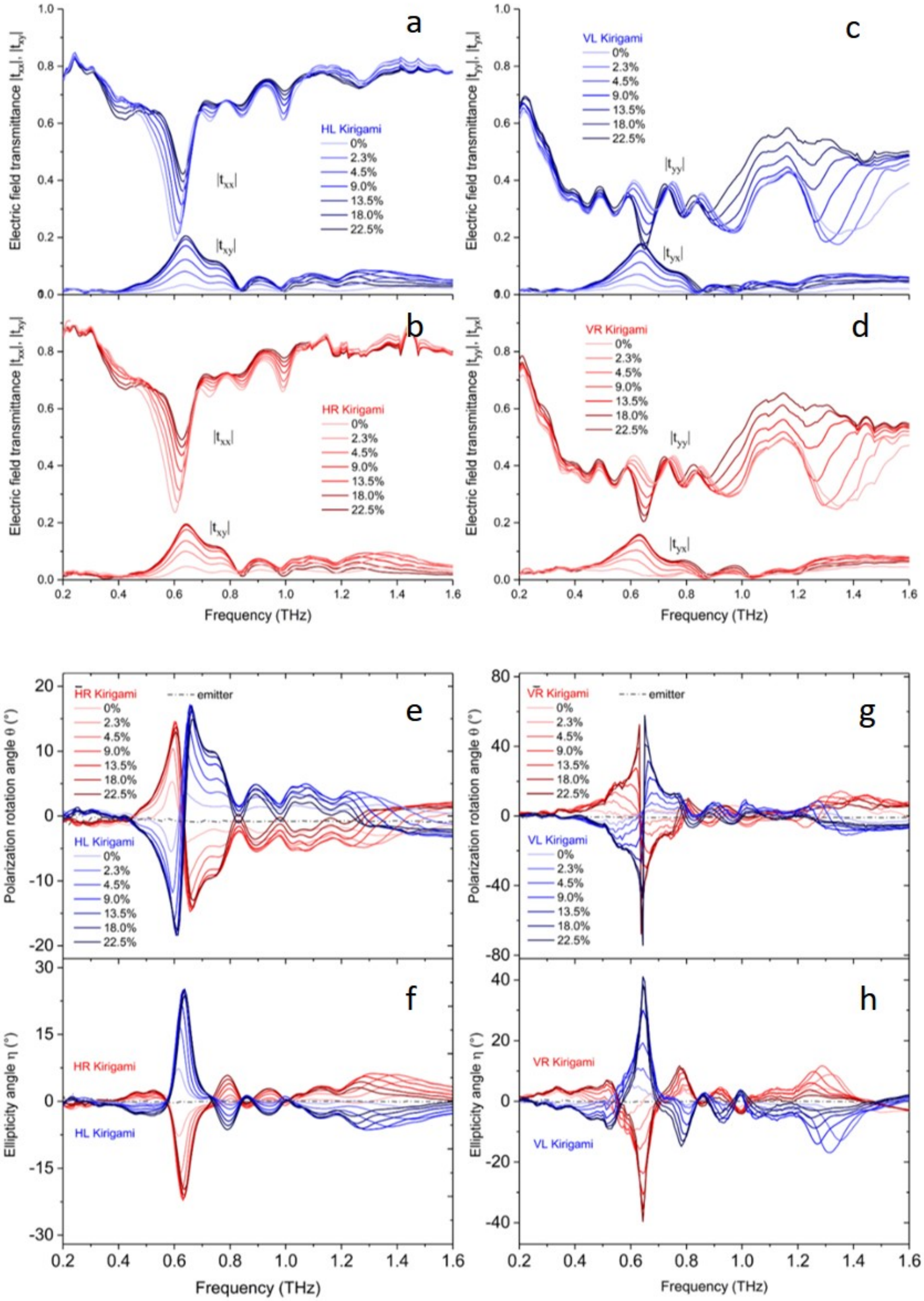

Figure 4-7. Experimental data for kirigami modulators with slant angle of 30°. (a) – (d) the magnitudes of four transmittance coefficients. (e) polarization rotation angle and (f) ellipticity angle induced by the samples mounted horizontally. (g) polarization rotation angle and (h) ellipticity angle induced by the samples mounted vertically. Blue and red curves are for left-handed (L) and right-handed (R) samples respectively. The strains applied are given in the legends and the same for all the subfigures. Adapted from Ref [12].

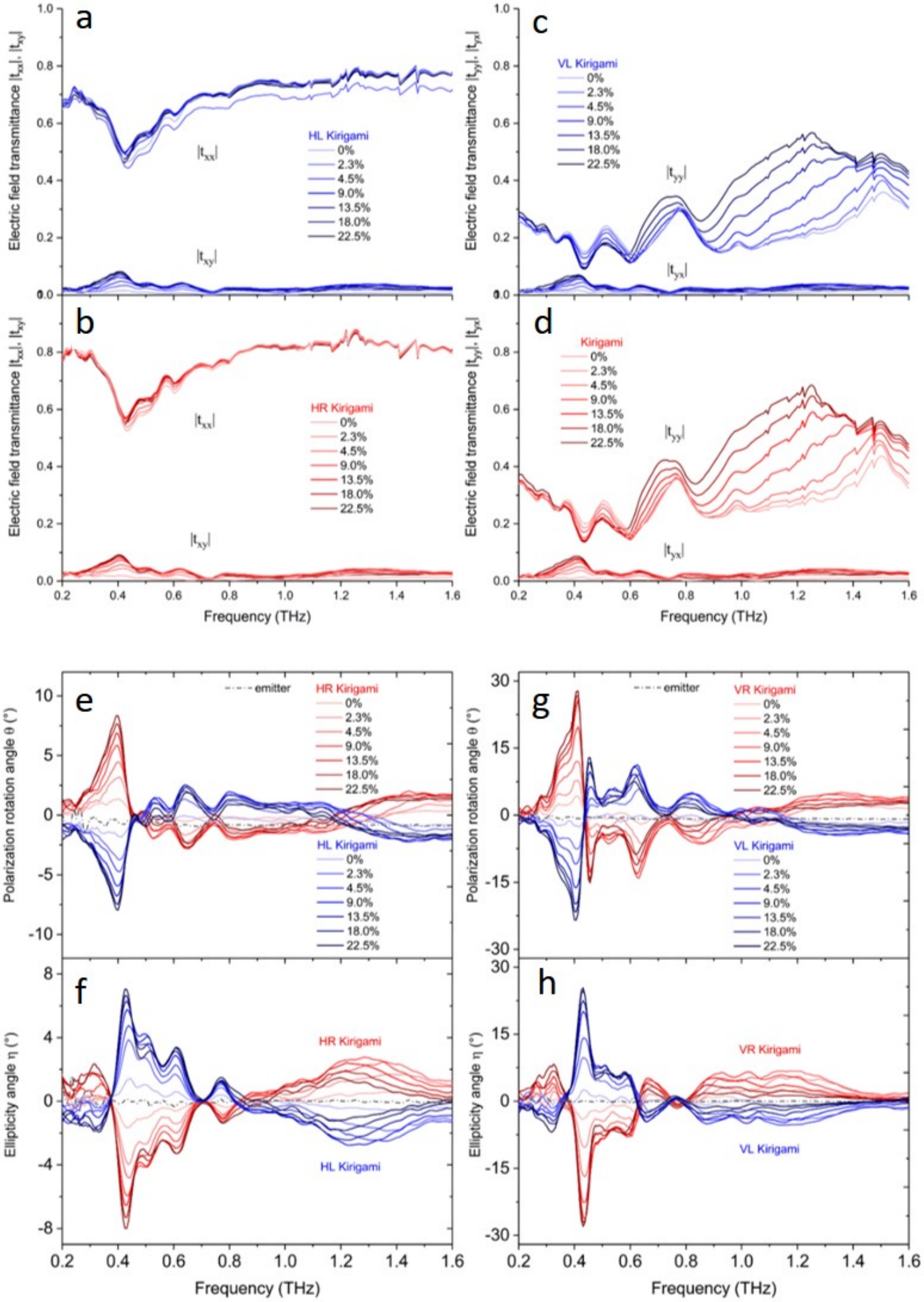

Figure 4-8. Experimental data for kirigami modulators with slant angle of 15°. (a) – (d) the magnitudes of four transmittance coefficients. (e) polarization rotation angle and (f) ellipticity angle induced by the samples mounted horizontally. (g) polarization rotation angle and (h) ellipticity angle induced by the samples mounted vertically. Blue and red curves are for left-handed (L) and right-handed (R) samples respectively. The strains applied are given in the legends and the same for all the subfigures. Adapted from Ref [12].

chirality of these kirigami modulators as shown in Figure 4-9. As a control, an achiral pattern with horizontally aligned ($\varphi = 0°$) Au strips is also measured and shows near-zero values of TCD regardless of the strain, confirming the critical role of the double-pattern design for the strong optical activity.

To test its robustness and repeatability, a kirigami modulator with slant angle $\varphi = 45°$ is stretched and released for 1000 cycles, and as shown by Figure 4-10 its polarization modulations remain nearly identical over the cycles justifying its usefulness as a reconfigurable modulator.

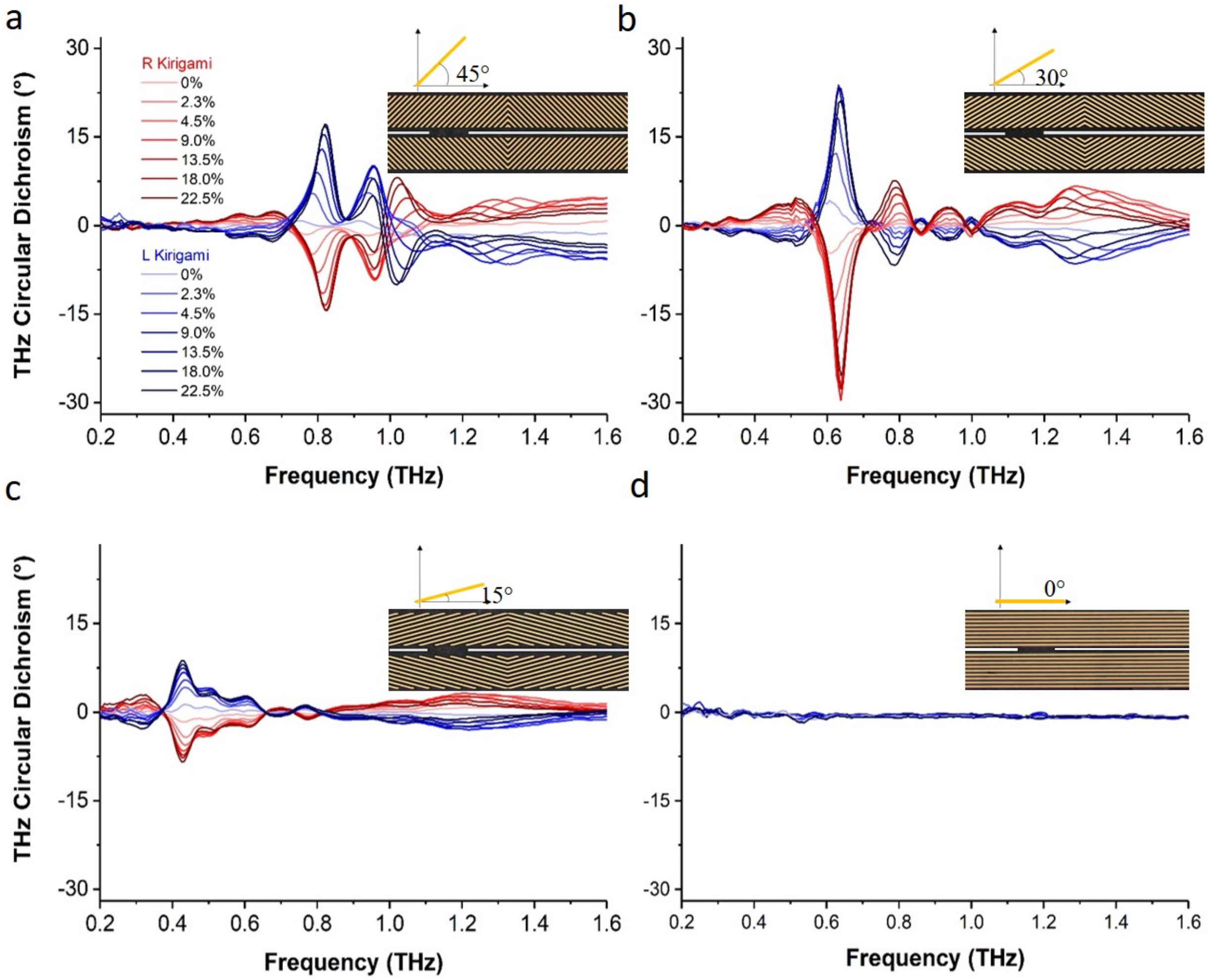

Figure 4-9. Experimental TCD for kirigami modulators with different slant angles. (a) $\varphi = 45°$. (b) $\varphi = 30°$. (c) $\varphi = 15°$. (d) $\varphi = 0°$. Blue and red curves are for left-handed (L) and right-handed (R) samples respectively. The strains applied are given in the legends and the same for all the subfigures. Adapted from Ref [12].

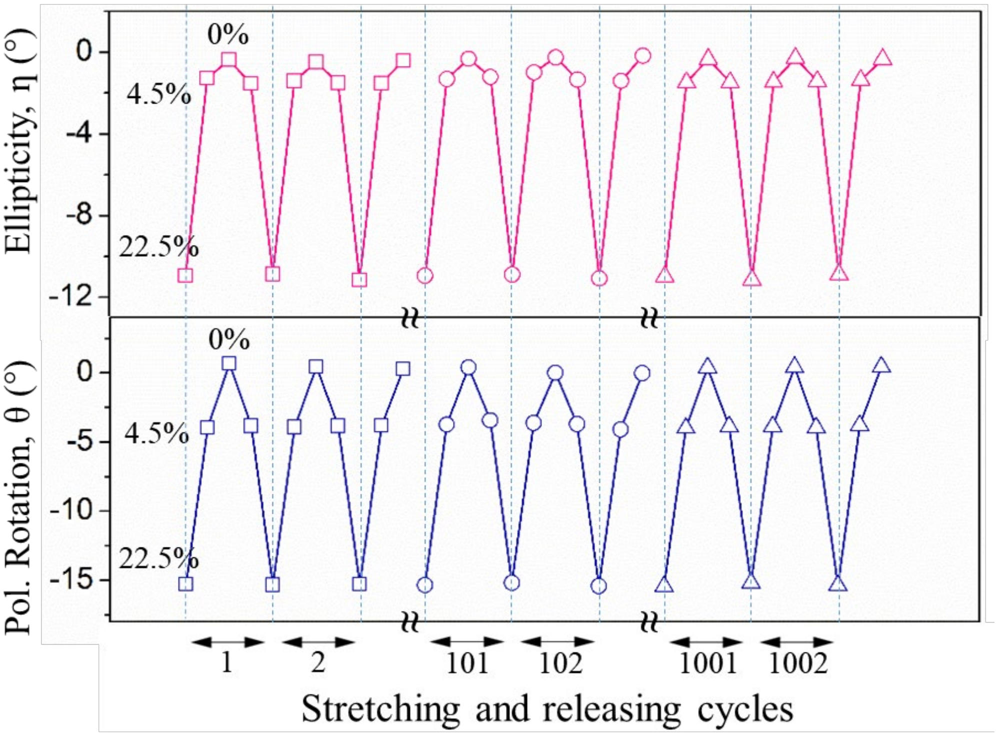

Figure 4-10. Polarization rotation and ellipticity angle of stretching and releasing over 1000 cycles. Both θ and η values are taken at 0.84 THz using a kirigami modulator with slant angle φ of 45°. The percentage values are the applied mechanical strains. Adapted from Ref [12].

4.3.4 Experimental results of varying unit cell size

The effect of the microscale cut pattern on the optical performance of the kirigami polarization modulators is also tested for variable size of the unit cell for a constant slant angle of $\varphi = 30°$. As shown in Figure 4-11, as L_{cut} becomes larger, the main TCD peak shifts to the lower frequencies, indicating that its spectral position is determined by the longitudinal plasmonic resonances of the Au strips. Confirming this, kirigami modulators with Au strips with the same length and φ but narrower width are also measured and display the same positions of the resonance peaks. The resonance wavelength of the kirigami sheets with herringbone patterns can be heuristically assessed as an LC circuit with the resonance frequency of $f_r = (2\pi\sqrt{L_{Au}C_{Au}})^{-1}$ [22]. The inductance L_{Au} and capacitance C_{Au} of Au strips scale linearly with its length, l [22], and therefore f_r becomes inversely proportional to l as shown in Figure 4-11 (d). This relation can be used to provide an approximate guide of the design of herringbone patterns for different applications.

It should also be mentioned that even though frequency tuning can be achieved by changing either the slant angle or the unit cell size, slant angle is more suitable for the fine adjustment of the resonance frequency, while varying the unit cell size is more applicable to scale the design to other frequency ranges such as microwaves with larger patterns and infrared with smaller sizes.

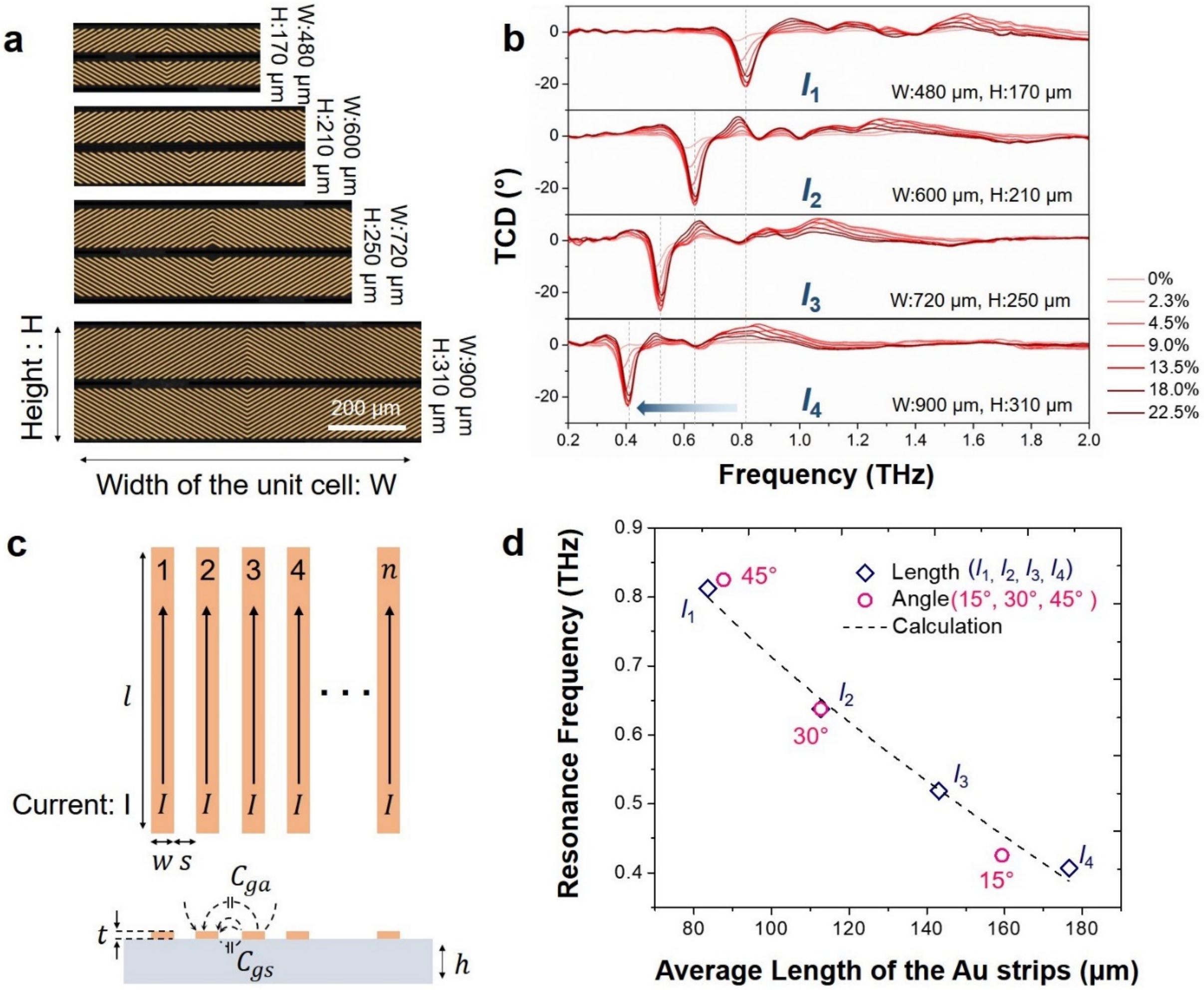

Figure 4-11. Experimental results of varying unit cell size. (a) Optical microscope image of unit cells of various sizes. All samples have *φ* of 30°. (b) Result of measured TCD from an R-kirigami modulators with unit cell of various sizes. (c) Top, parallel conducting strips to obtain total inductance of the configuration. Bottom, parameters for calculating the capacitance of array of strips. (d) Relation between resonance frequency and average length (*l*) of the Au strips. Adapted from Ref [12].

4.4 Modeling and simulation of single kirigami modulators

4.4.1 Modeling of kirigami 3D geometries

The 3D topography of the kirigami sheets under various strains are measured using a laser confocal microscope (OLS 4000 LEXT, Olympus). The kirigami geometries are reconstructed using 3D graphic software packages (Rhino 5, Robert McNeel & Associates and 3D Max 2017, Autodesk) based on the experimentally acquired images from the confocal microscopy. Three projected images captured at different view angles are used to clearly define and reconstruct the radius, angles, shapes and boundaries. Two 3D structures with different applied strains of a right-handed (R) kirigami sheet with 45° slant angle are reconstructed as shown in Figure 4-12 (a) and (b). These models are mirrored by the in-plane reflection to make their corresponding left-handed (L) structures. In addition, an achiral structure with a 0° slant angle is also modeled using the same procedure as shown in Figure 4-12 (c).

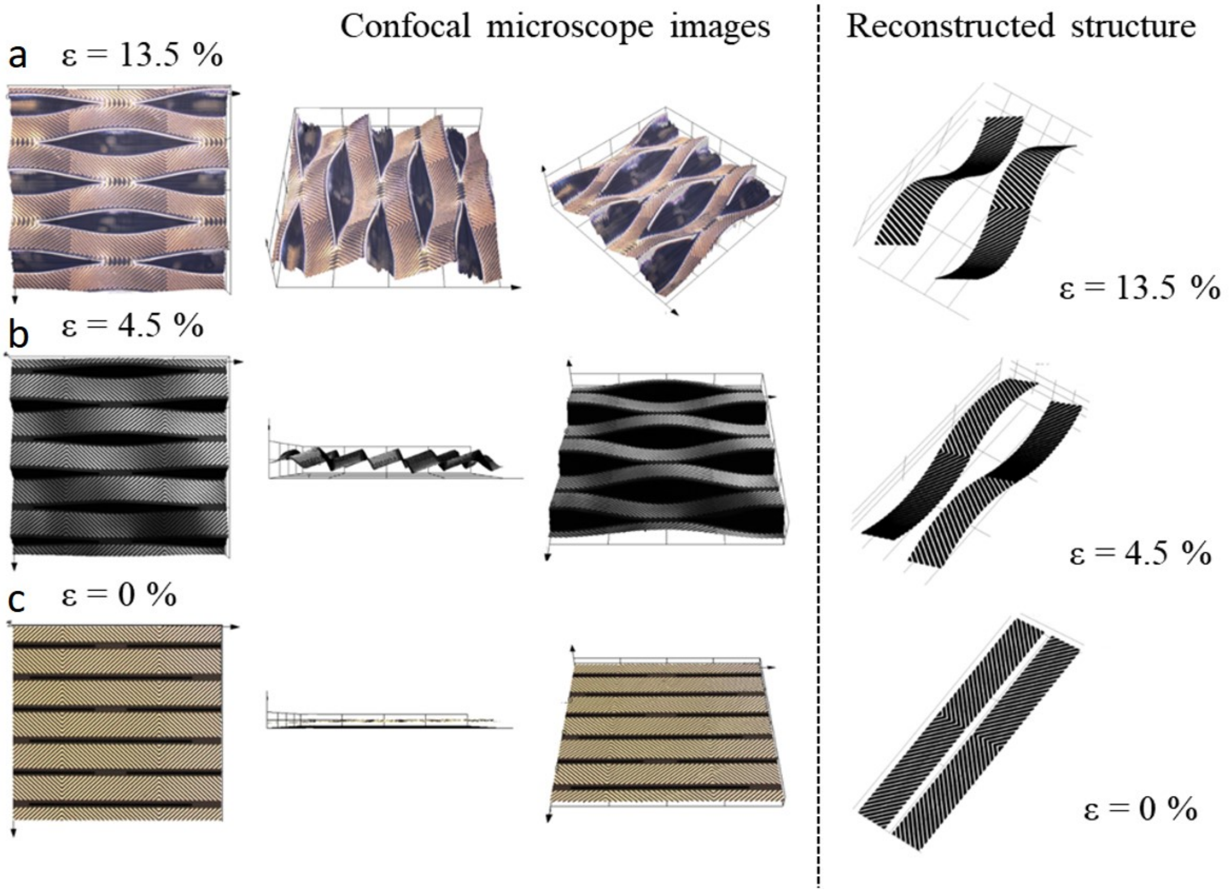

Figure 4-12. Confocal microscopy images and reconstructed 3D models of a kirigami modulator under different strains. The three rows correspond to the same right-handed sample with a 45° wire slant angle under (a) 13.5%, (b) 4.5% and (c) 0% strains, respectively. The first three columns are the images of three different viewpoints from the confocal microscopy under a 20x objective. The last column are the reconstructed 3D models corresponding to each strain. Adapted from Ref [12].

4.4.2 Simulation of kirigami modulators

TCD simulation and surface current norm distributions of illuminated kirigami modulators are numerically investigated with finite element simulation software (COMSOL Multiphysics 5.2a, COMSOL Inc.) using the above reconstructed 3D models for the shape. Because the parylene substrate is very thin and shows low loss tangent over the THz range without chiroptical activity [19], it is omitted from the calculation model. Periodic boundary conditions are applied to the

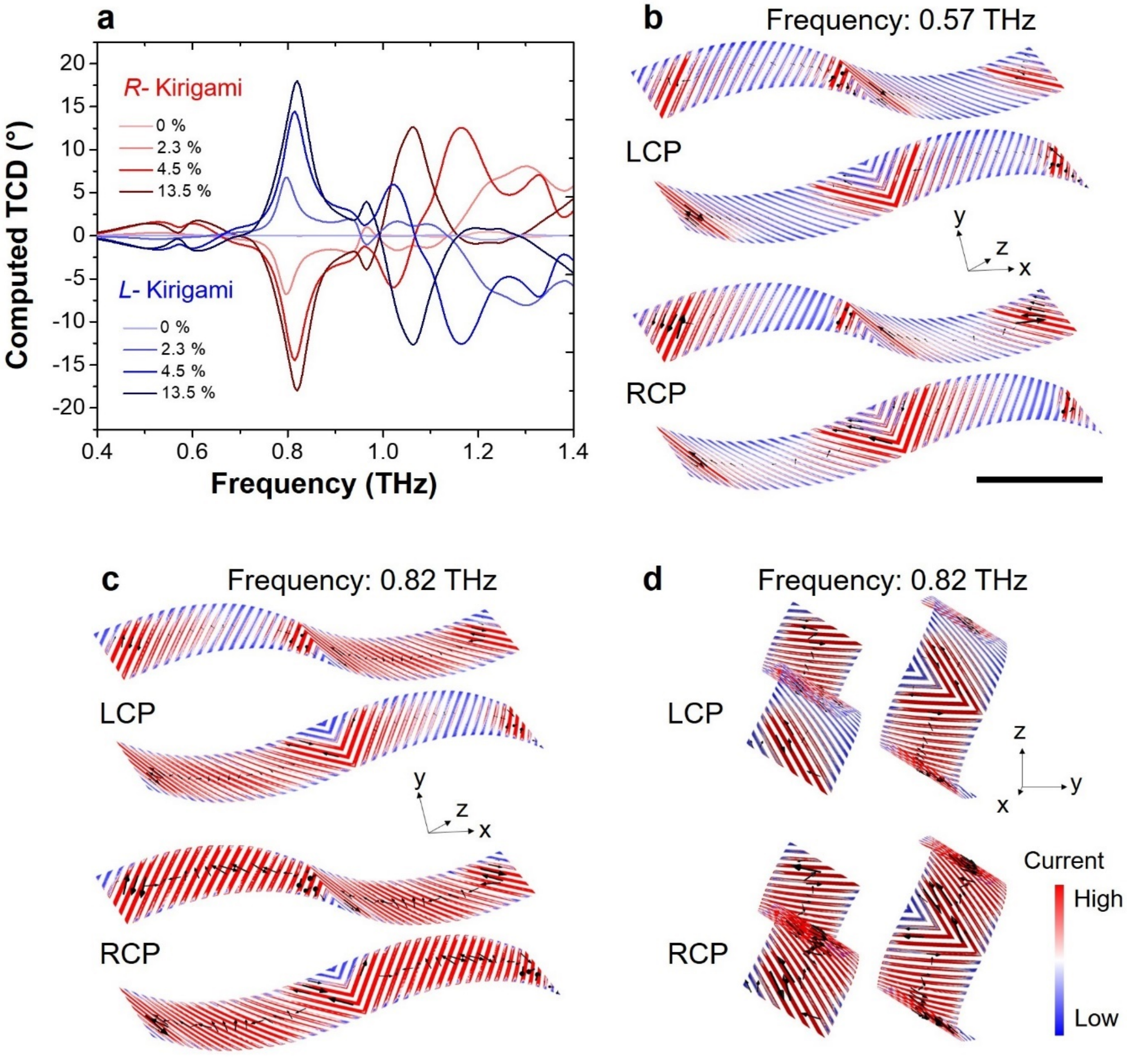

Figure 4

Figure 4-13. Simulated THz circular dichroism and time-averaged current norm distributions on the kirigami modulator with $\varphi = 45°$. (a) Computed TCD spectrum for four deformation states. (b) (c) Tilted view of current norm distributions of R-kirigami at frequencies of 0.57 THz and 0.82 THz. (d) Side view of current norm distributions of R-kirigami at 0.82 THz. Black arrows indicate the current directions. Right and left circularly polarized beams are denoted RCP and LCP, respectively. Scale bar, 200 μm. Adapted from Ref [12].

single unit cell of each model to simplify the simulation and to reduce the required computational power. It should be noted that this could lead to some simulation errors due to the infinite unit cells assumed by periodic boundary conditions. In the experiment, of course, there are a finite number of unit cells defined by diameter of the THz beam; this could be one of the reasons that the magnitudes of the simulation are slightly larger than the experimental data. Apart from this slight difference, as Figure 4-13 (a) shows, the computed TCD spectra match the experimental data very well with respect to the signs of chirality, peak positions, relative peak widths and general amplitudes.

Calculated time-averaged current norm distributions generated on the Au strips for the incident of the circularly polarized beams point to the origin of the plasmonic states responsible for individual peaks [6]. As seen from Figure 4-13 (b), at the off-resonant frequency of 0.57 THz, the induced currents are low for both co- and cross-circularly polarized beams and most of the Au strips are optically inactive. At the resonant frequency of 0.82 THz in Figure 4-13 (c) and (d), however, the incident beam induces strong currents in the Au strips. Simultaneously, the currents excited by the right-handed circularly polarized beam significantly exceed those for the left circularly polarized beam. As a result, the transmittance of the left circularly polarized beam is larger than that of the right circularly polarized beam due to the induced current, which is consistent with the sign of the peaks in Figure 4-13 (a). On the other hand, we can find strong secondary peaks around 1.05 THz and 1.15 THz, and these could come from electromagnetic coupling between adjacent strips [6,22].

4.5 Experimental setup and data of stacked kirigami modulators

4.5.1 Optical setup and sample configurations

The kirigami modulators shown in Section 4.3 can only be either left- or right-handed for a single device. For more practical spectroscopy, it is desired that a single modulator can generate both left and right circular/elliptical polarizations and realize enantiomeric switching [6]. Also, it is usually wanted for the polarization modulations to be as large as possible. Both goals can be achieved by stacking two kirigami sheets as an integrated modulator.

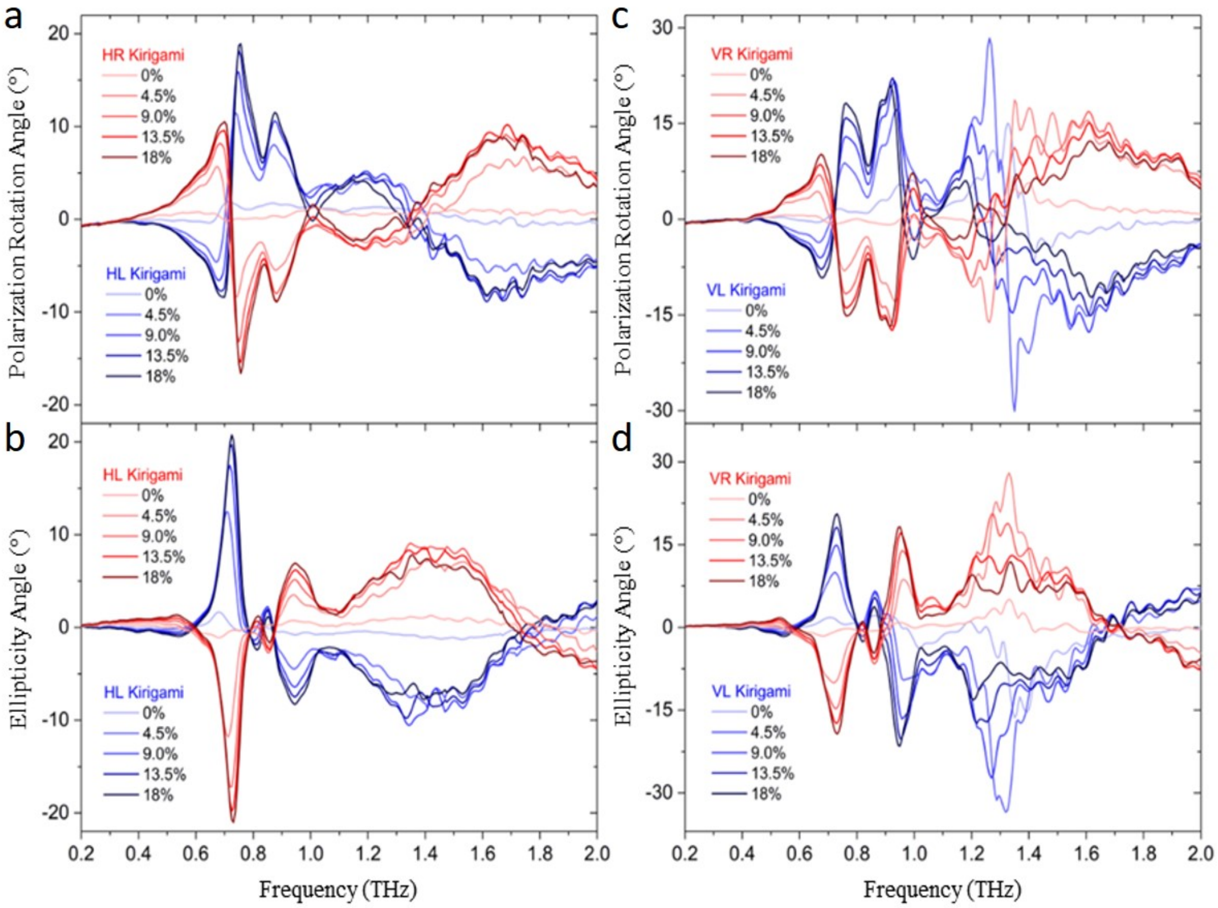

Figure 4-14. Experimental data for kirigami samples with slant angle of 37.5°. (a) polarization rotation angle and (b) ellipticity angle induced by the samples mounted horizontally. (c) polarization rotation angle and (d) ellipticity angle induced by the samples mounted vertically. Blue and red curves are for left-handed (L) and right-handed (R) samples respectively. The strains applied are given in the legends. Adapted from Ref [12].

Kirigami modulators with 37.5^{o} slant angle (φ) are specifically used to characterize and demonstrate the effects of stacking two kirigami layers on the polarization states. Each individual modulator including *HR*, *HL*, *VR* and *VL* is measured separately using the two-polarizer method described above, with results shown in Figure 4-14. Two modulators from these four are then placed longitudinally along the collimated THz propagation (z-axis) direction, with a separation of ~2 cm and actuated by two independent piezo-controllers from 0 % to 18 % strain, as shown by the schematic of the experimental setup in Figure 4-15. Four combinations of two samples (i.e. *VL* and *HL*, *VR* and *HL*, *VL* and *HR*, *VR* and *HR*) are measured and the total effects on the rotation and ellipticity of the polarization are shown in Figure 4-16 to Figure 4-19. These four combinations are chosen to show the *enhancement* of optical activity by stacking kirigami with the *same* chirality and to show *compensation* by stacking kirigami with *opposite* chirality. It turns out that if the mounting orientations for the two kirigami modulators are perpendicular i.e. the first is oriented vertically (*V*) and the second horizontally (*H*), the birefringence cancels. This is an important requirement for the combinations of modulators with opposite chirality to compensate *both* optical activity and birefringence. Also, for each combination there are 25 modulations achieved by 5 different strains applied to each kirigami independently as shown in Figure 4-16 to Figure 4-19.

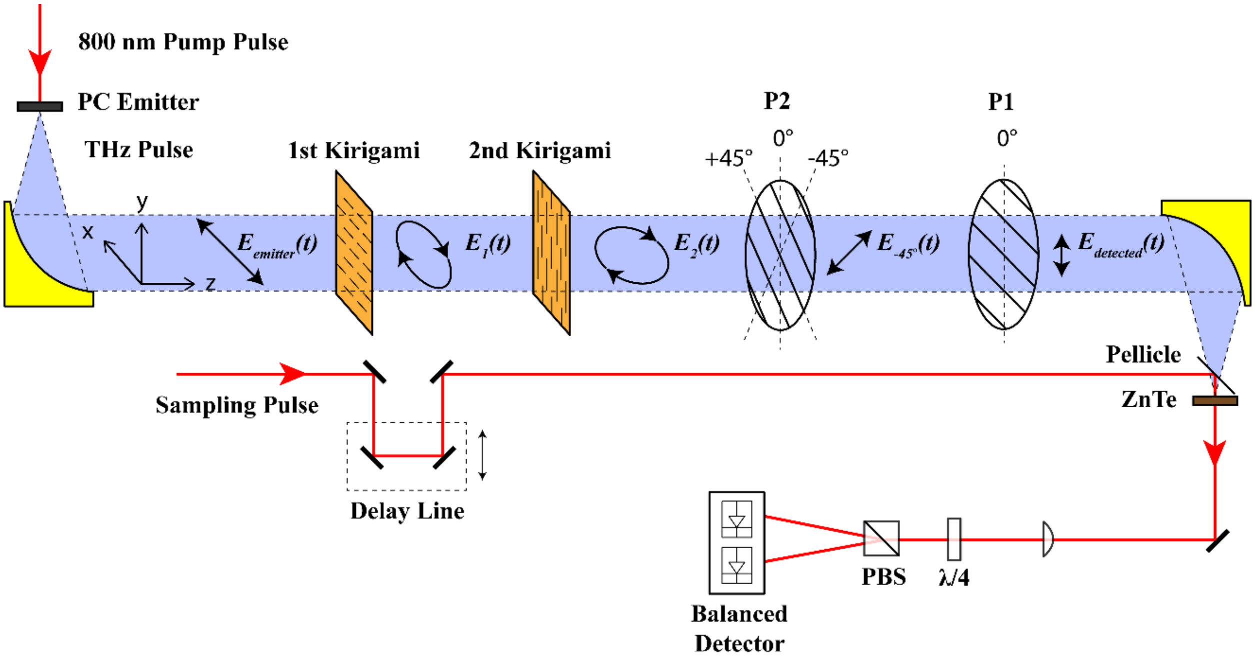

Figure 4-15. Schematic of the experimental setup for stacked kirigami configuration. A second kirigami sheet is inserted behind the first one to form a double stack configuration and they are controlled by two piezo controllers independently. The configuration of the two kirigami sheets shown here is that the first kirigami mounted vertically and the second kirigami mounted horizontally. The distance between the two kirigami layers is about 2 cm. Adapted from Ref [12].

4.5.2 Experimental results of stacked kirigami modulators with opposite chirality

The experimental data in Figure 4-16 (*VR* and *HL*) and Figure 4-17 (*VL* and *HR*) indicate that chirality-switchable modulator can be achieved by stacking two kirigami sheets with opposite handedness. When the left-handed kirigami sheet is stretched while the right-handed sheet is released, the overall integrated modulator is equivalent to a single left-handed modulator; when the left-handed sheet stays released while right-handed sheet is strained then it is equivalent to a single right-handed modulator – this realizes the handedness switching in a single device without the need of changing modulators in a spectrometer.

Moreover, it is only when the strains applied to the two sheets are the same that the output polarization state is the same as the input, i.e. zero polarization rotation and zero ellipticity. The small non-zero values at these strains in the experimental results come from the imperfect matching and alignment between the two samples and can be improved by more careful control of samples or by additional calibration methods. This result can be potentially used for the development of secure THz communication where the first kirigami sheet is used for encryption while the second one for decryption and only when the strains (“keys”) of the two sheets match each other the original polarization information can be restored and measured. Additionally, as mentioned above, since the kirigami sheets are anisotropic they also need to be oriented perpendicularly to totally cancel the polarization change. This orientation requirement (another pair of “keys”) adds another degree of security for the potential THz communication.

4.5.3 Experimental results of stacked kirigami modulators with the same chirality

The experimental data of stacked kirigami sheets with the same chirality shown in Figure 4-18 (*VL* and *HL*) and Figure 4-19 (*VR* and *HR*) indicate that this stacking configuration can produce increased polarization modulation. The magnitudes of both polarization rotation and ellipticity are larger than those of a single kirigami modulator as shown in Figure 4-14. This result shows the possibility that ideal 90° rotation and 45° ellipticity could be achieved by stacking two or more kirigami sheets, especially given that some of our kirigami structures e.g. the ones with slant angle of 30° already have very large polarization modulation.

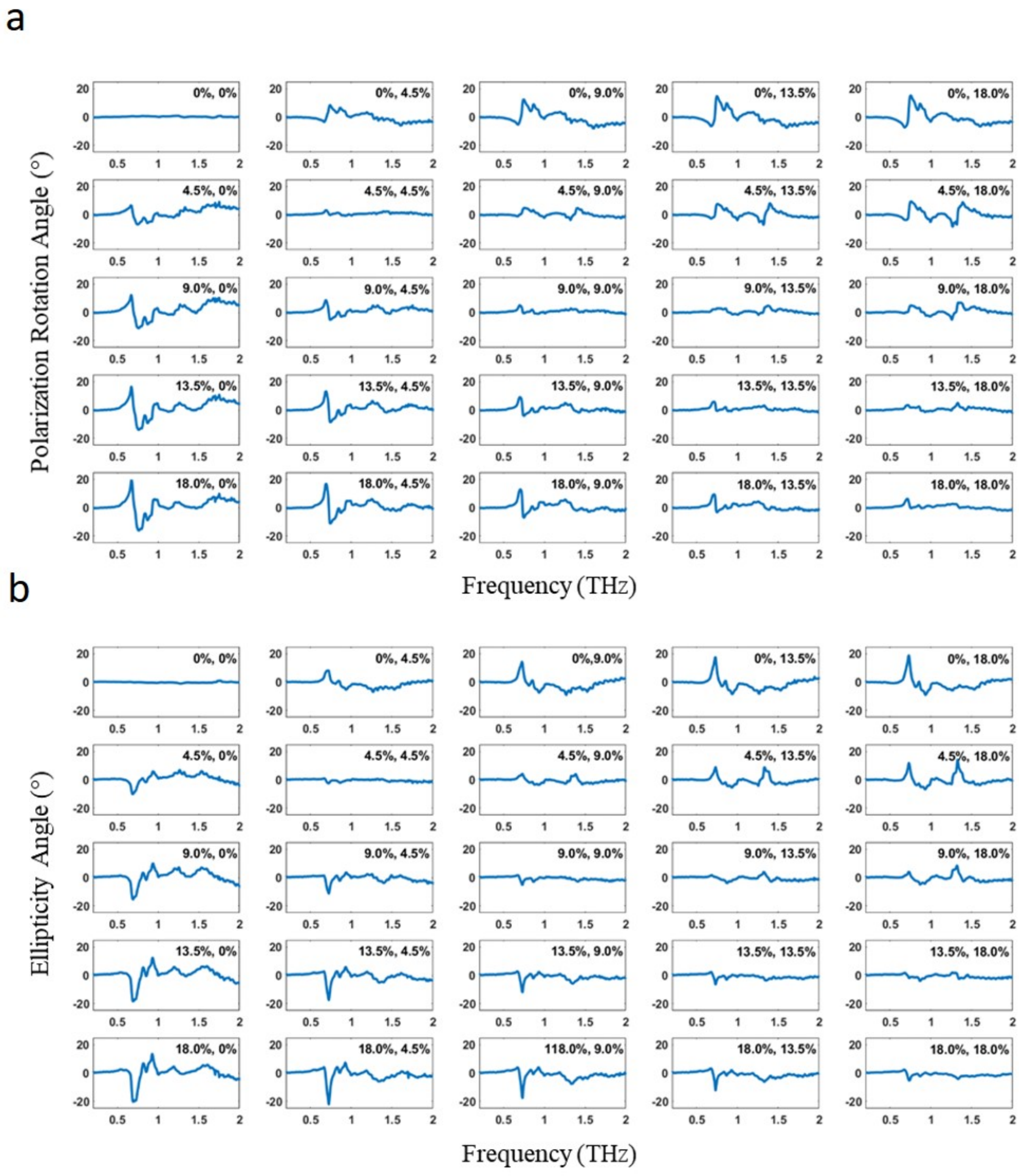

Figure 4-16. Experimental results for vertically positioned right-handed (VR) kirigami and horizontally positioned left-handed (HL) kirigami stack. (a) Polarization rotation angle and (b) ellipticity angle measured from the double stacked kirigami sheets. The first and second number in the legends are the strains applied to the first and second kirigami sheets, respectively. Both kirigami sheets have 37.5° slant angle (φ). Adapted from Ref [12].

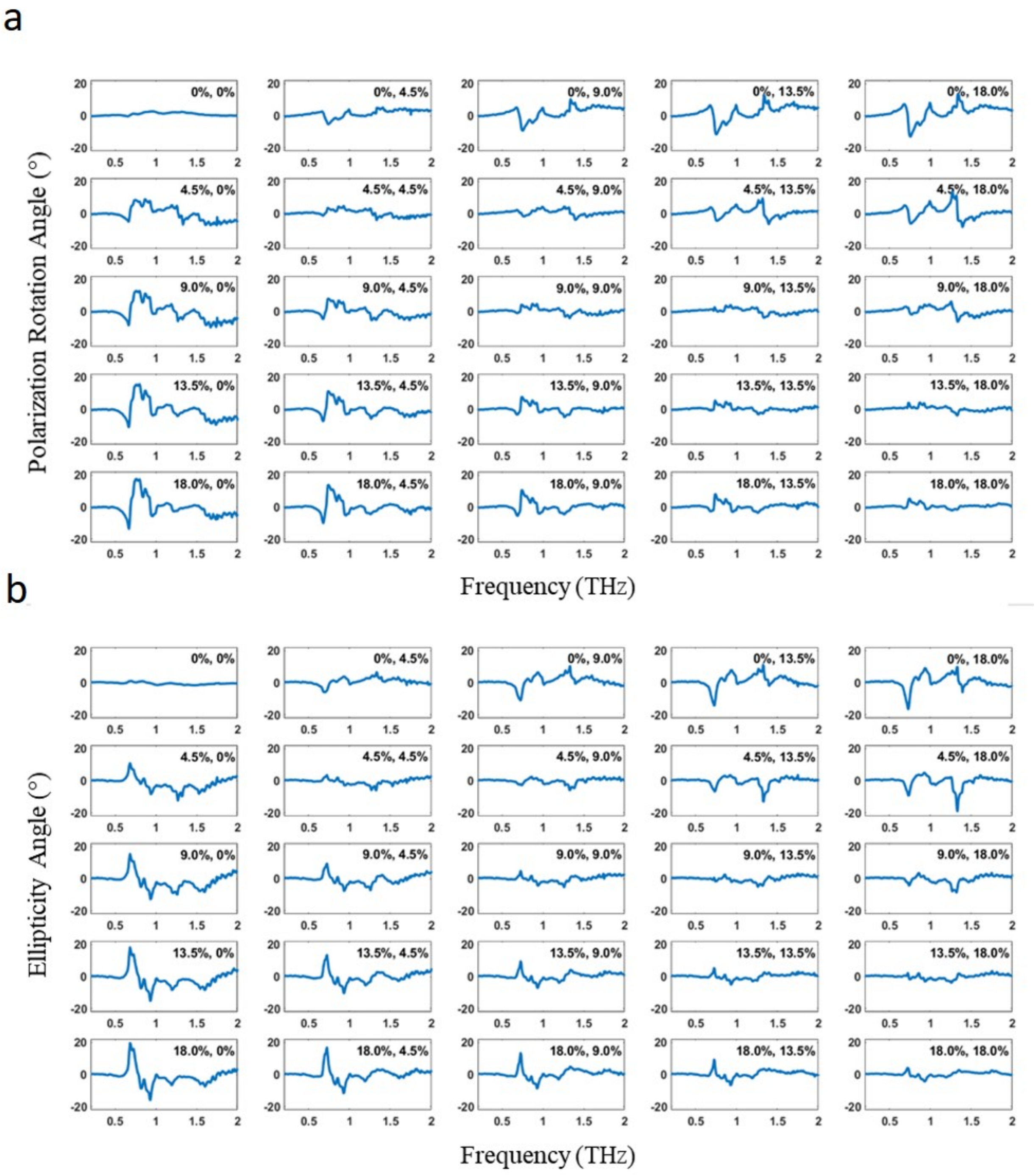

Figure 4-17. Experimental results for vertically positioned left-handed (VL) kirigami and horizontally positioned right-handed (HR) kirigami stack. (a) Polarization rotation angle and (b) ellipticity angle measured from the double stacked kirigami sheets. The first and second number in the legends are the strains applied to the first and second kirigami sheets, respectively. Both kirigami sheets have 37.5° slant angle (φ). Adapted from Ref [12].

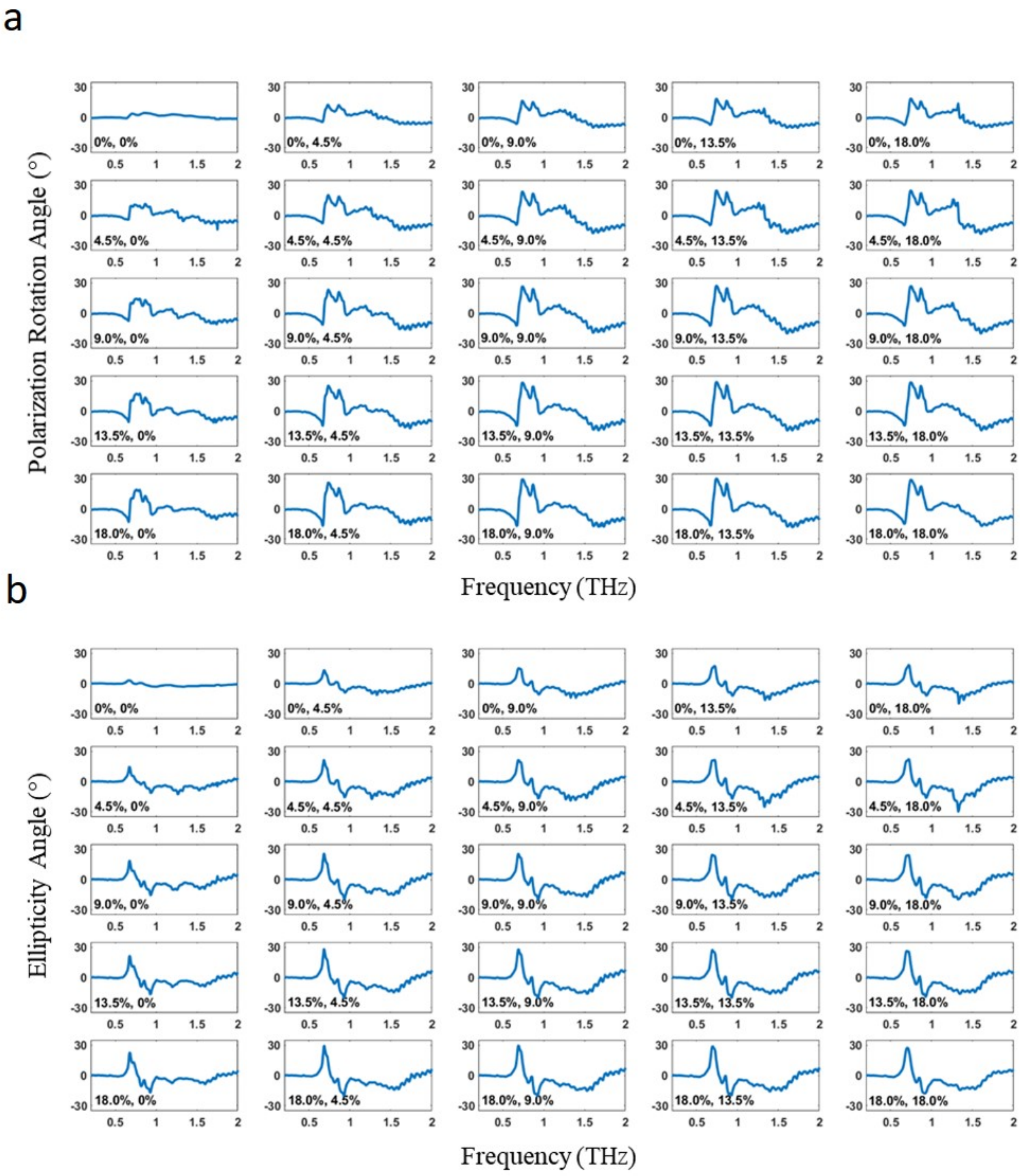

Figure 4-18. Experimental results for vertically positioned left-handed (VL) kirigami and horizontally positioned left-handed (HL) kirigami stack. (a) Polarization rotation angle and (b) ellipticity angle measured from the double stacked kirigami sheets. The first and second number in the legends are the strains applied to the first and second kirigami sheets, respectively. Both kirigami sheets have 37.5° slant angle (φ). Adapted from Ref [12].

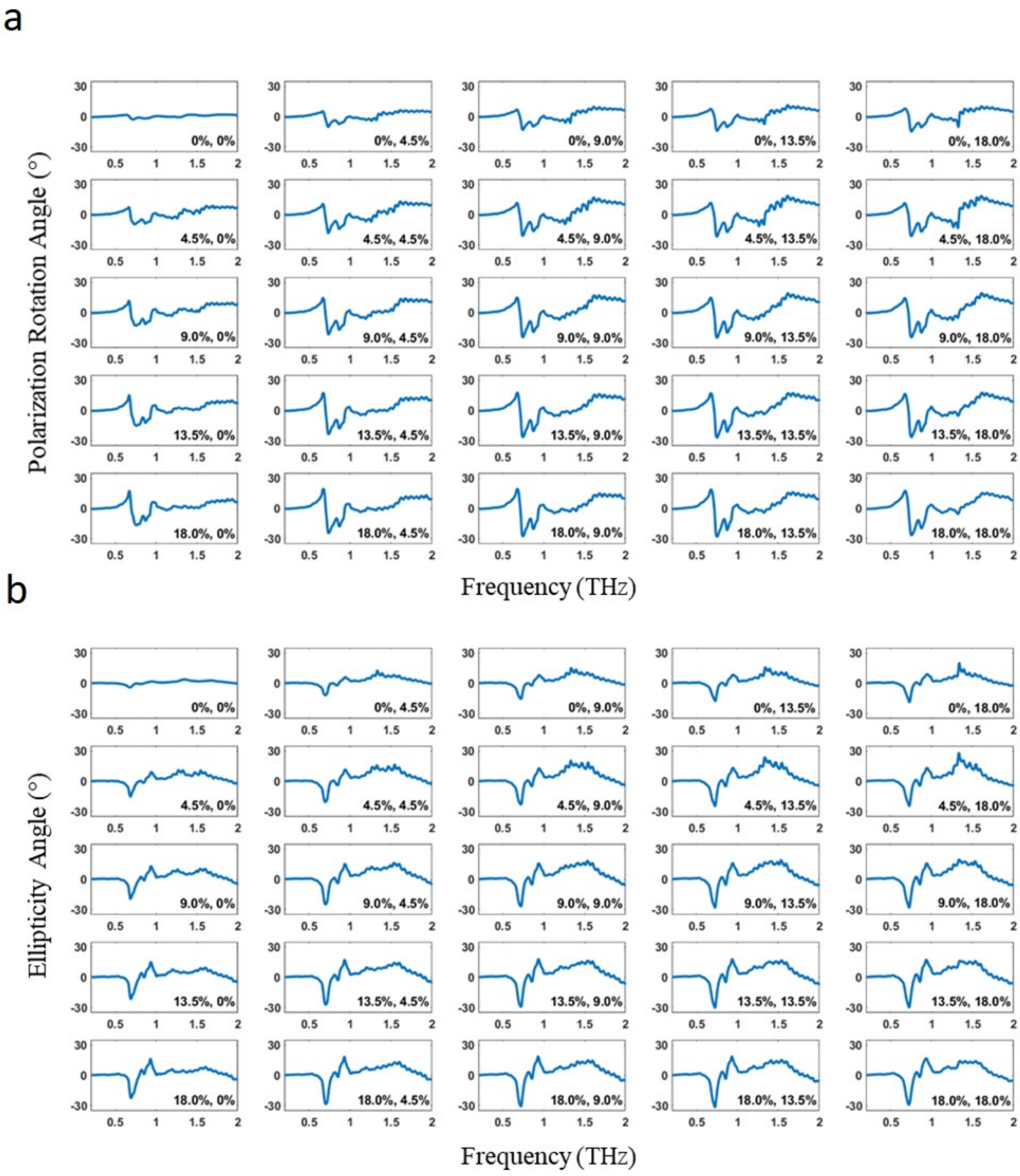

Figure 4-19. Experimental results for vertically positioned right-handed (VR) kirigami and horizontally positioned right-handed (HR) kirigami stack. (a) Polarization rotation angle and (b) ellipticity angle measured from the double stacked kirigami sheets. The first and second number in the legends are the strains applied to the first and second kirigami sheets, respectively. Both kirigami sheets have 37.5° slant angle (φ). Adapted from Ref [12].

4.6 THz circular dichroism (TCD) spectroscopy enabled by kirigami modulators

4.6.1 Concept of TCD spectroscopy with kirigami modulators

The unique combination of high ellipticity and tunability of kirigami optics makes possible its utilization for modulating THz light beams in practical realizations of TCD spectroscopy to investigate biological and other materials that are opaque in the visible range but transparent for THz radiation. The concept of a TCD spectrometer enabled by kirigami modulators is shown in Figure 4-20. Here, the kirigami modulators function similarly to photoelastic modulators (PEMs) in conventional circular dichroism spectrometers [23] by generating left- and right-elliptically/circularly polarized light, and TCD spectra are calculated directly from the difference of transmission intensities between the left and right elliptically polarized THz beam (EPB) generated by kirigami modulators according to

$$TCD\ by\ kirigami\ modulator = tan^{-1}\left(\frac{{I_{LK}}^{1/2} - {I_{RK}}^{1/2}}{{I_{LK}}^{1/2} + {I_{RK}}^{1/2}}\right) \tag{4.1}$$

where I_{LK} and I_{RK} are the intensities of the left and right EPB after passing through the sample, respectively.

The optical quantity that needs to be measured here is intensity, rather than complex electric field as needed for the time-domain polarimetric methods described in Chapter 2. This means that the detector shown in Figure 4-20 is not limited to only electro-optic crystals and instead can be almost any kind of THz detectors such as DTGS (deuterated triglycine sulphate) crystals, liquid helium cooled bolometers, pyroelectric sensors, etc. [24], and therefore this TCD spectrometer does not necessarily requires bulky, expensive and complicated femtosecond laser system and THz-TDP setup. Instead, it is readily compatible to the commercially available THz FTIR spectrometers or even simpler THz setups only consisted of sources, detectors and THz filters or gratings, and therefore this proposed TCD method is more accessible to a wider research communities and laboratories compared to the very specialized ultrafast optics techniques required by the previous THz-TDP methods.

Additionally, unlike the THz-TDP methods in Chapter 2 which require sequential measurements, the TCD spectroscopy proposed here only needs the differential intensity transmission between left and right elliptical polarizations. This allows the kirigami modulator and the detector to be integrated with high-speed and high-frequency instrument such as function generators, modulation controllers and lock-in amplifiers, therefore this differential TCD spectroscopy could be much more sensitive and accurate than the sequential THz-TDP using linear polarizers.

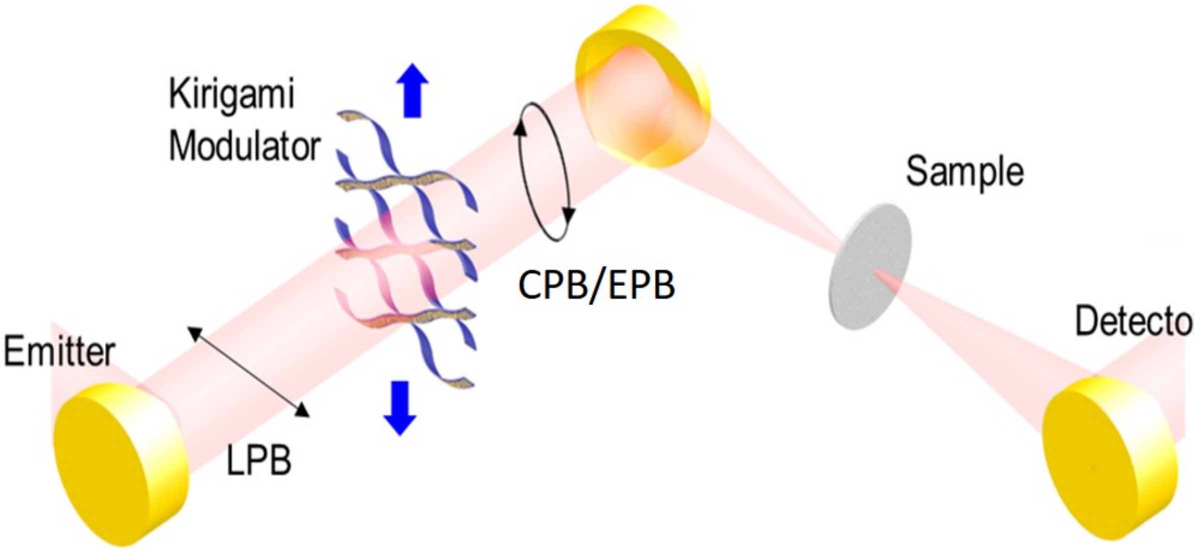

Figure 4-20. Concept of TCD spectroscopy using kirigami modulators. A focused THz beam with ~500 μm spot size after modulated by the kirigami modulators is used to explore biological samples. LPB, CPB and EPB indicate the linearly, circularly and elliptically polarized beams, respectively. Adapted from Ref [12].

4.6.2 Experimental TCD results of kirigami modulators

First, as a demonstration of the concept and verification of our experimental setup, TCD spectra of kirigami sheets are measured using the same stacked configuration shown in Figure 4-15, where the "1st kirigami" functions as a polarization modulator and the "2nd kirigami" acts as a tunable sample. The first kirigami modulator generates left- or right- elliptical/circular polarization beam like a photoelastic modulator (PEM) in a conventional CD spectrometer [23], and the second kirigami sheet is probed and characterized as the sample. Dynamic modulations of the two chiral kirigami sheets are applied independently which translate into individual manipulations of ellipticity of the input beam from 0 to 20.8° and the chiroptical activity of the sample with applied strain from 0% to 18.0%.

The transmitted intensities are obtained directly from the square of the magnitude of the electric field (therefore no complex electric field or Jones matrix is used) and normalized to the transmitted intensity when no strain is applied to the first kirigami modulator to eliminate any inherent mismatch between left-handed and right-handed modulators. Figure 4-21 shows the experimental data of TCD spectra of L- and R- kirigami samples ("2nd kirigami") with 5 strain conditions, for 5 different input elliptical polarizations. As expected, the measured TCD gets larger with increasing strain on the second kirigami samples which induces larger chirality. When the ellipticity of the input beam becomes larger, the measured TCD also increases because the handedness difference between the incident left- and right- elliptically polarized beams is increased. The top row subfigures all have zero TCDs because they are normalized by themselves using the processing method mentioned above.

Validation of our proposed TCD spectroscopy is performed by comparing this TCD measured by kirigami modulator with TCD measured by THz-TDP using linear wire-grid polarizers as shown in Figure 4-22 for a pair of kirigami sheets with slant angle of 37.5°. The TCD spectra measured by kirigami modulator in Figure 4-22 (B) are obtained with a 20.8° ellipticity input generated by the "1st kirigami" i.e. they are the same as the last rows from Figure 4-21 (a) and (b). From the comparison, we can see that the resonance peak positions and general spectrum shapes measured by kirigami modulator are very consistent with those measured by THz-TDP verifying the effectiveness of our proposed TCD spectroscopy using kirigami modulators. There are some small discrepancies, however, between the results measured by these two methods. First, the signs of the resonance peaks at 0.95 THz are reversed. This is because of the different definitions of TCD in the two methods given by Eq. (2.24) and Eq. (4.1) respectively and the left- (right-) handed kirigami modulators actually generate right- (left-) elliptical polarizations at this specific frequency. Second, the magnitudes of TCD peaks measured by kirigami modulator are relatively smaller than those measured by THz-TDP because the polarization produced by the kirigami modulators here is elliptical (maximum ellipticity is 20.8°) rather than perfectly circular (45° ellipticity) while in THz-TDP perfect circular polarizations Eq. (2.23) are used for the derivation of TCD. The accuracy of the absolute magnitudes in the TCD by kirigami modulator method can be improved by either optimizing the kirigami samples or taking into consideration the actual polarization states.

a. *L*-Kirigami

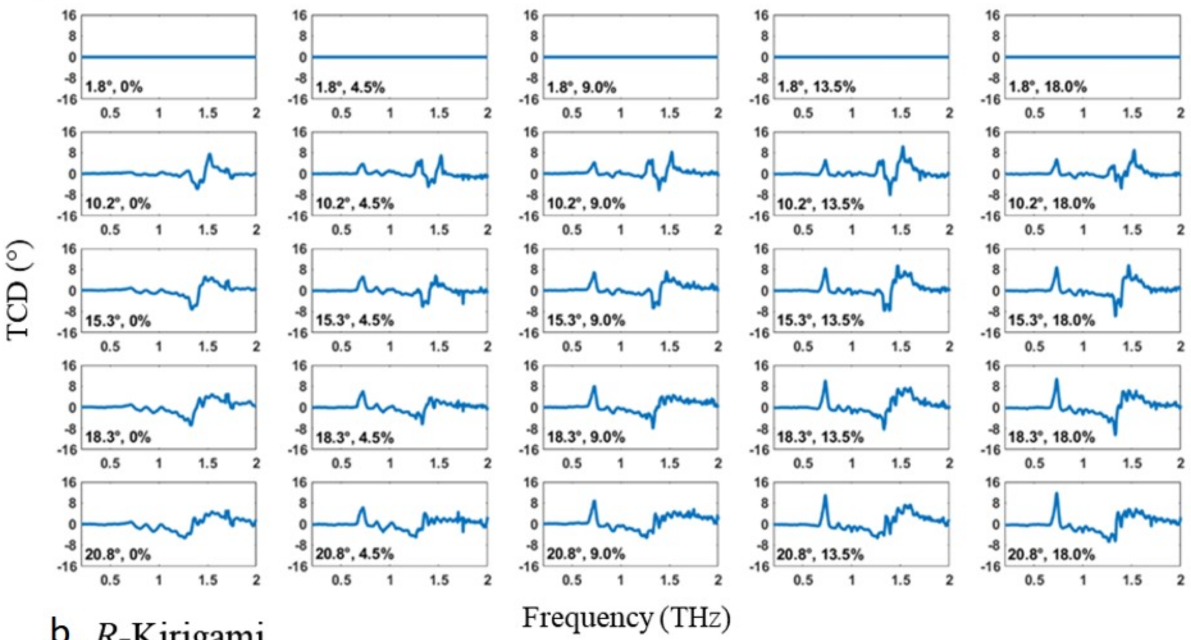

b. *R*-Kirigami

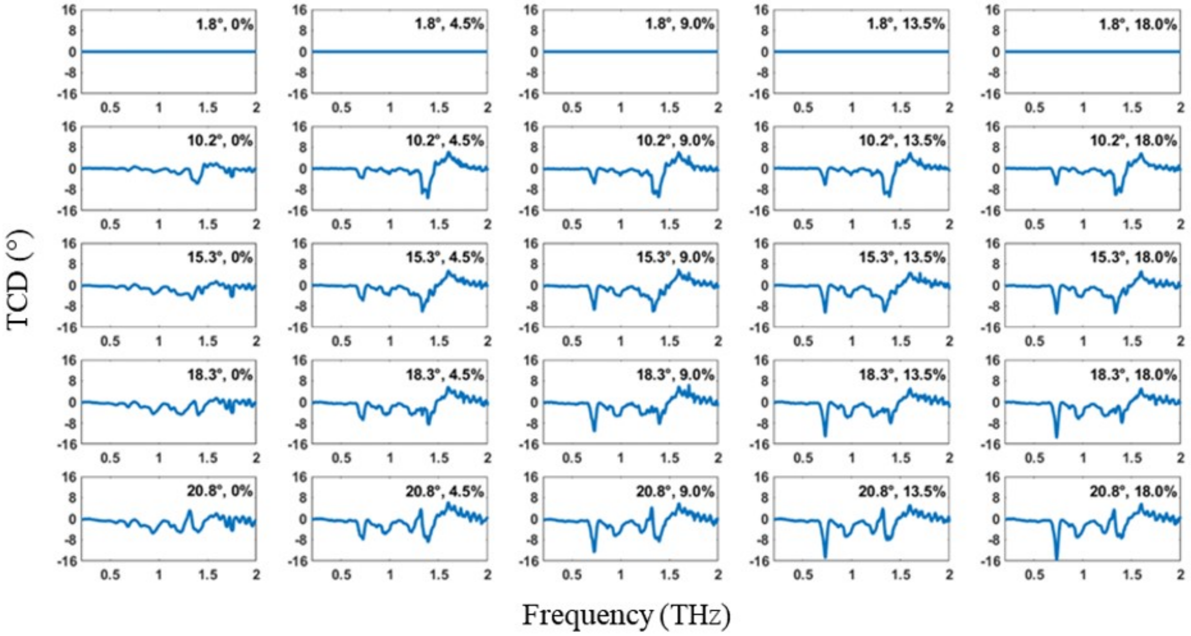

Figure 4-21. Experimental TCD spectra of kirigami sheets measured by kirigami modulators. TCD spectra of left-handed kirigami (a) and right-handed kirigami (b) samples with slant angle φ of 37.5°. The first number in the legends is the ellipticity of incident THz beam generated by the kirigami modulator (first kirigami) at 0.73 THz. The non-zero ellipticity (1.8°) when the first kirigami modulators are not stretched is due to their own residual strains. The second number is the strain applied to the second kirigami sheet which controls the chirality of the probed sample. Adapted from Ref [12].

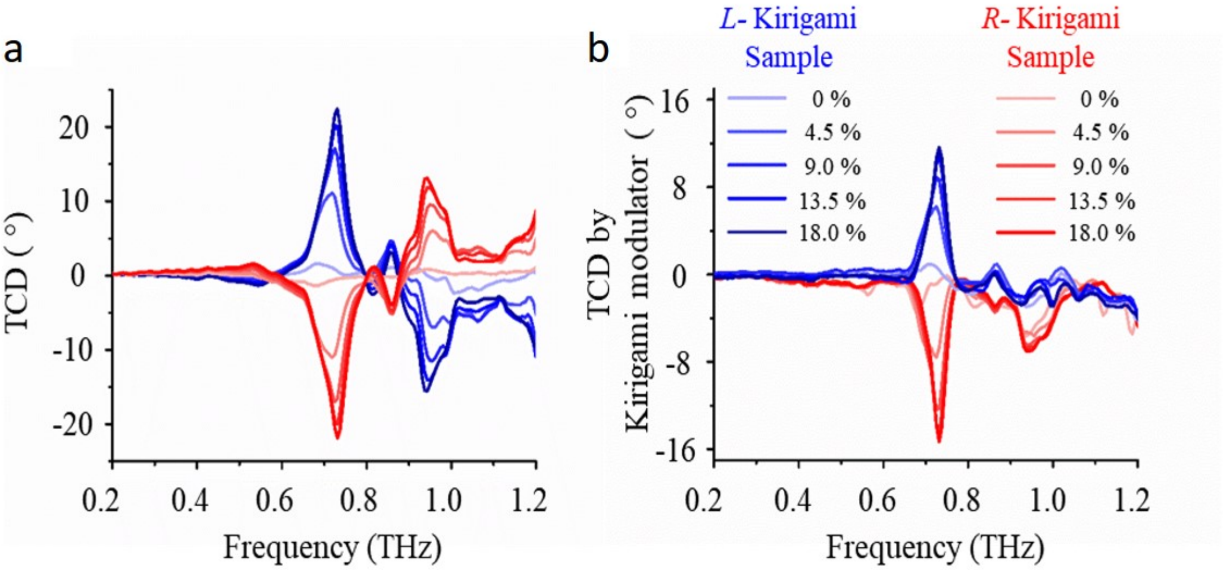

Figure 4-22. TCD spectra of kirigami samples with slant angle of 37.5° using linear-polarizer THz-TDP method and kirigami modulator method. (a) TCD spectra measured by two-polarizer THz-TDP method. (b) TCD spectra measured by kirigami chiral modulator with a fixed 20.8° ellipticity input. Blue and red curves are for left-handed (L) and right-handed (R) samples respectively. The strains applied are given in the legends. Adapted from Ref [12].

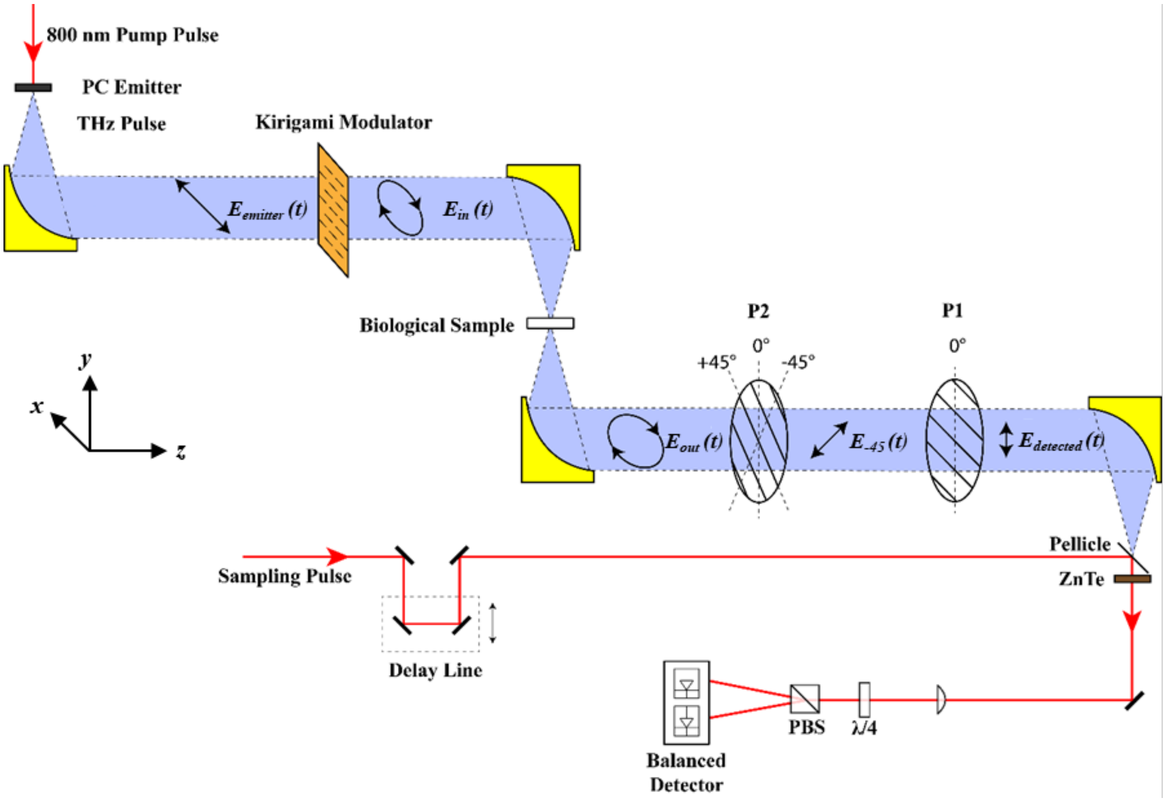

Figure 4-23. Schematic of the experimental TCD setup for biological samples. The elliptically/circularly polarized THz beam generated by the kirigami modulator is focused by an off-axis parabolic gold mirror to a spot size of approximately 500 μm and acts as the input for the biological samples. The transmitted THz beam through the sample is collected and collimated by another off-axis parabolic gold mirror for detection. Adapted from Ref [12].

4.6.3 Experimental TCD results of cystine biomolecules

After a demonstration and verification of our TCD spectroscopy by kirigami modulators, now we can use it to investigate the unknown chiral THz properties of some biological materials. Due to the small size of these biological samples, a focused THz beam with ~500 μm spot size is used and the schematic of the experimental setup is shown in Figure 4-23. The whole setup is enclosed in a box purged by extra-dry nitrogen and the relative humidity is maintained below 3% to minimize the water vapor absorption and to maximize the measurement sensitivity. The kirigami modulators with 37.5° slant angle are used to generate left- and right-handed elliptical polarizations.

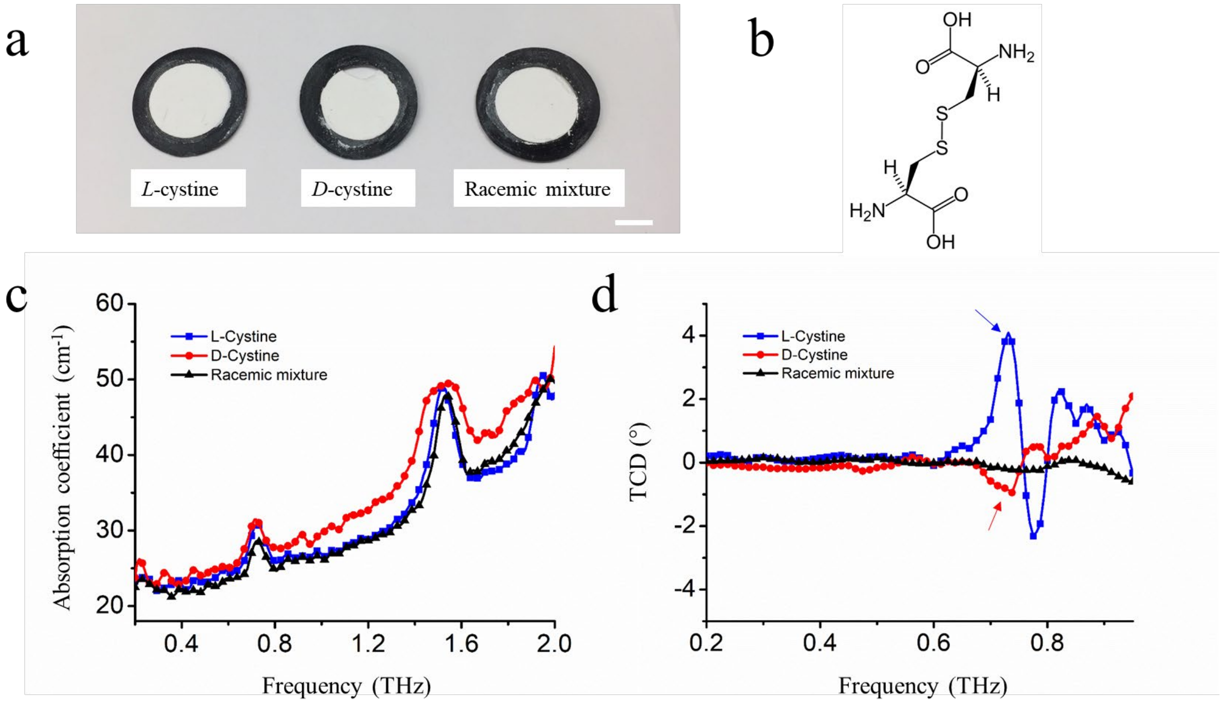

Figure 4-24. Experimental TCD results of cystine biomolecules. (a) Photo image of *L*-, *D*- and racemic cystine pellets. Scale bar, 1cm. (b) Molecular structure of a *L*-cystine molecule. (c) THz absorption spectra of cystine biomolecules. (d) TCD spectra of cystine biomolecules. Adapted from Ref [12].

The first set of samples are cystine biomolecules [25] which are made from powders pressed to self-standing pellets with a diameter of 35 mm and thickness of 4 mm and then subjected to one-hour acid treatment by HCl (hydrochloride acid) to improve their crystallinity. Figure 4-24 shows the absorption coefficients and TCD spectra of the *L*-, *D*-cystine and its racemic mixture. We can clearly see the mirror-like TCD peaks between *L*- and *D*-cystine in the range of 0.7 to 0.8

THz indicating opposite chirality, and the signal vanishes for the racemic mixture which is expected to be achiral. There is a small discrepancy in magnitude and shape between *L*- and *D*-cystine which may originate from the fact that the *L*-cystine can be obtained by hydrolysis of animal materials in nature but *D*-cystine can only be artificially synthesized therefore their secondary and tertiary structures may not be exactly same.

4.6.4 Experimental TCD results of beetle elytron

As a more complicated biological material, an elytron of *Chrysina gloriosa* beetle, which is known to have the selective reflection of circularly polarized light in the visible range [26] as shown in Figure 4-25 (a) and (b), is investigated using our TCD spectroscopy for its potential THz chiral properties. First, the noise level of our method is established by a reference measurement without any sample as shown in Figure 4-25 (f) with RMS noises of 0.008°, 0.068°, 0.098° and 0.149° for the four applied strains within the frequency range of our interest. The increasing noise level with the strain is mainly due to the difficulty of exactly matching the left-handed and right-handed modulators when they are stretched. Then, for the beetle elytron sample, as can be seen from Figure 4-25 (g), a positive peak in TCD as large as ~3° (i.e. a SNR over 20) at 0.68 THz is observed in the red circled area as shown in Figure 4-25 (e). To eliminate the possible contribution of anisotropy, two more areas on the same elytron with different random orientations are also measured. All the results have similar curve shapes and magnitudes and TCDs are all positive around the main peak at 0.68 THz. Moreover, these spectra show the same increasing trend as the ellipticity of the input polarization gets larger. All these experimental results confirm the strong chiroptical activity in the THz range for beetle elytron, and can be associated with the chiral conical structures with dimensions of ~10 μm shown in Figure 4-25 (c) which can be schematically represented by cholesteric liquid crystals as in Figure 4-25 (d) [26].

4.6.5 Experimental TCD results of other biological materials

Some other biological materials, including a leaf of sugar maple tree (*Acer saccharum*), a dandelion petal (*Taraxacum officinale*) and a piece of pig fat, are also investigated with their results shown in Figure 4-26: the reference in Figure 4-26 (d), with no biological sample in place, shows near zero TCD indicating the intensity transmissions of the two kirigami modulators are almost the same; the sample of a maple leaf in Figure 4-26 (e) shows a very small chiral response with larger noise which is mainly due to the lower signal-to-noise ratio (SNR) caused by the THz

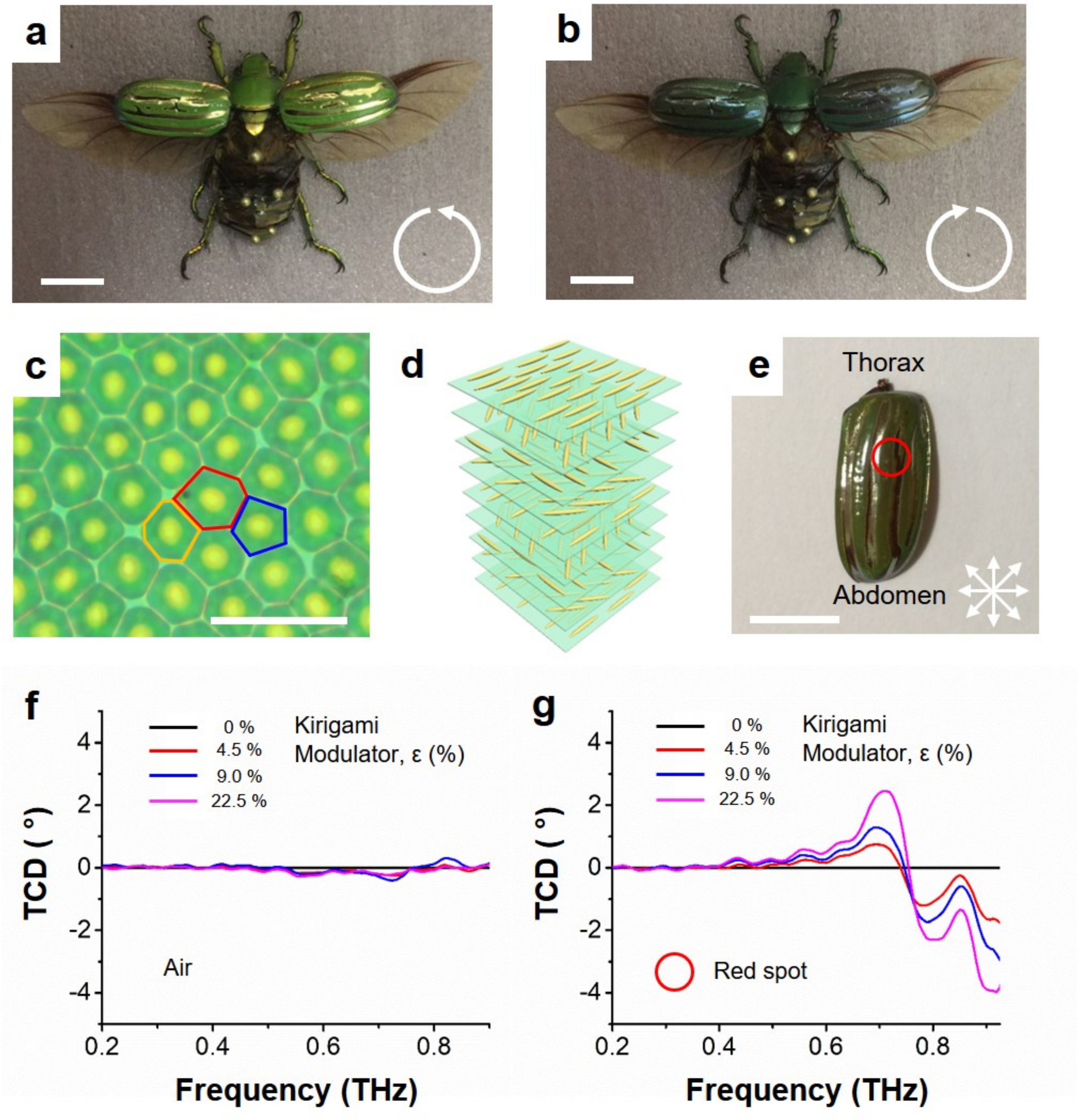

Figure 4-25. Experimental TCD results of beetle elytron. Photographs of the beetle *C. gloriosa* with a visible left (a) and right (b) circular polarizer in front of the camera, respectively. (c) Optical microscopy image of the exoskeleton of the beetle *C. gloriosa* elytron. The shapes of the cells are pentagonal (blue), hexagonal (red) and heptagonal (orange). Scale bar, 20 µm. (d) Schematic representation of Bouligand structure. (e) Image of an elytron of *C. gloriosa* without a polarizer. The red circle indicates the spot for the TCD measurements. (f) TCD spectrum without sample as a reference for the noise level of the system. The RMS noises are 0.008°, 0.068°, 0.098° and 0.149° for the four strains respectively. (g) TCD spectrum for *C. gloriosa* elytron measured by a kirigami modulator for four different values of strain (%). Scale bars in (a,b,e), 1 cm. Adapted from Ref [12].

absorption by the leaf; a petal of a dandelion flower in Figure 4-26 (f) shows negative TCD signals between 0.3-0.8 THz with increasing magnitudes as the input ellipticity gets larger; and the sample of pig fat in Figure 4-26 (g) shows negligible TCD. These characterizations through kirigami TCD spectroscopy could be the starting point for the further study of their underlying microstructures and biomolecules. Further theoretical and numerical investigations are also needed.

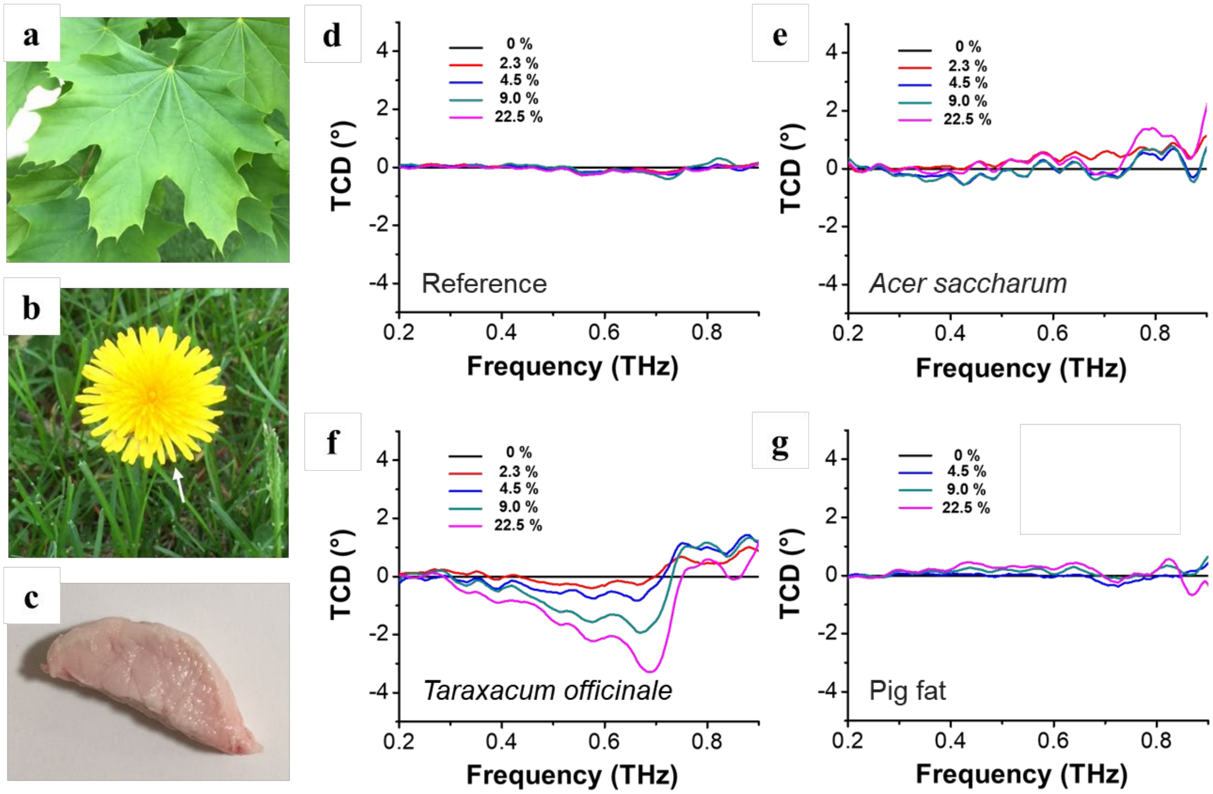

Figure 4-26. Experimental TCD results of other biological materials. Photographs of (a) a leaf of maple sugar tree, (b) a petal of dandelion and (c) a piece of pig fat. The arrow in the dandelion image in (b) indicates the actual sample for the measurement. (d) to (g) are TCD spectra of reference, a leaf (*Acer saccharum*), a petal (*Taraxacum officinale*) and a piece of pig fat, respectively. The legend shows the strains applied to the kirigami modulators. Adapted from Ref [12].

4.7 Summary

We have developed a set of kirigami modulators for the THz polarization modulation. The double-pattern design of kirigami materials combining submillimetre cuts and micrometre-scale plasmonic stripes affords real-time tunability of helical structures oriented perpendicularly to the propagation of the THz beam. Kirigami optical elements make possible the realization of TCD spectroscopy and a better understanding of complex biological materials. The lightweight capabilities and high polarization efficiency of kirigami optics open the possibility of portable and compact THz spectrometers and imagers. The realization of real-time polarization modulation of THz beams also enables advances in secure high-bandwidth communication and non-invasive imaging. Biomedical images distinguishing the tissues in respect to multiple scales of chirality characteristic for TCD can be particularly suitable to gain high contrast in soft tissues.

Reference

1. Acbas, G., Niessen, K. A., Snell, E. H. and Markelz, A. G. Optical measurements of long-range protein vibrations. *Nat. Commun.* **5**, 3076 (2014).
2. Plusquellic, D. F., Siegrist, K., Heilweil, E. J. and Esenturk, O. Applications of terahertz spectroscopy in biosystems. *ChemPhysChem*. **8**, 2412–2431 (2007).
3. Wilmink, G. J. and Grundt, J. E. Current state of research on biological effects of terahertz radiation. *J. Infrared Millim. Terahertz Waves.* **32**, 1074–1122 (2011).
4. Choi, J. H. and Cho, M. Terahertz Chiroptical Spectroscopy of an α-Helical Polypeptide: A Molecular Dynamics Simulation Study. *J. Phys. Chem. B.* **118**, 12837–12843 (2014).
5. King, M. D., Buchanan, W. D. and Korter, T. M. Understanding the terahertz spectra of crystalline pharmaceuticals: Terahertz spectroscopy and solid-state density functional theory study of (S)-(+)-ibuprofen and (RS)-ibuprofen. *J. Pharm. Sci.* **100**, 1116–1129 (2011).
6. Kan, T. et al. Enantiomeric switching of chiral metamaterial for terahertz polarization modulation employing vertically deformable MEMS spirals. *Nat. Commun.* **6**, 8422 (2015).
7. Cong, L., Pitchappa, P., Wang, N. and Singh, R. Electrically programmable chiral MEMS photonics. Preprint at https://arxiv.org/abs/1807.02914 (2018).
8. Zhang, S. et al. Photoinduced handedness switching in terahertz chiral metamolecules. *Nat. Commun.* **3**, 942 (2012).
9. Oh, S. S. and Hess, O. Chiral metamaterials: enhancement and control of optical activity and circular dichroism. *Nano Converg.* **2**, 24 (2015).
10. Qui, J. et al. Introducing quasi-optical terahertz circular dichroism spectroscopy. *Proc. 2017 11th Int. Conf. Antenna Theory Tech. ICATT* **11**, 26–29 (2017).
11. Dhillon, S. S. et al. The 2017 terahertz science and technology roadmap. *J. Phys. D* **50**, 043001 (2017).
12. Choi, W. J., Cheng, G., Huang, Z., Zhang, S., Norris, T. B. and Kotov, N. A. Terahertz circular dichroism spectroscopy of biomaterials enabled by kirigami polarization modulators. *Nat. Mater.* **1**, (2019)
13. Xu, L. et al. Kirigami nanocomposites as wide-angle diffraction gratings. *ACS Nano* **10**, 6156–6162 (2016).
14. Blees, M. K. et al. Graphene kirigami. *Nature* **524**, 204–207 (2015).
15. Rafsanjani, A. et al. Buckling-induced kirigami. *Phys. Rev. Lett* **118**, 084301 (2017).
16. Liu, Z. et al. Nano-kirigami with giant optical chirality. *Sci. Adv.* **4**, eaat4436 (2018).
17. Callens, S. J. P. & Zadpoor, A. A. From flat sheets to curved geometries: origami and kirigami approaches. *Mater. Today* **21**, 241–264 (2018).

18. Zhang, Y. et al. A mechanically driven form of kirigami as a route to 3D mesostructures in micro/nanomembranes. *Proc. Natl Acad. Sci. U.SA* **112**, 11757–11764 (2015).
19. Liu, X. et al. Metamaterials on parylene thin film substrates: design, fabrication, and characterization at terahertz frequency. *Appl. Phys. Lett.* **96**, 011906 (2010).
20. Mislow, K. *Molecular Chirality, in Topics in Sterochemistry* Vol. 22 (Topics in Stereochemistry, Wiley, 1999).
21. Menzel, C., Rockstuhl, C. and Lederer, F. Advanced Jones calculus for the classification of periodic metamaterials. *Phys. Rev. A* **82**, 053811 (2010).
22. Neu, J., Aschaffenburg, D. J., Williams, M. R. C. and Schmuttenmaer, C. A. Optimization of terahertz metamaterials for near-field sensing of chiral substances. *IEEE Trans. Terahertz Sci. Technol.* **7**, 755–764 (2017).
23. Tranter, G. E. in *Encyclopedia of Spectroscopy and Spectrometry* (2nd ed. Lindon, J. C.) 325–336 (Academic Press, 2010).
24. Tonouchi, M. Cutting-edge terahertz technology. *Nat. Photonics* **1**, 97-105 (2007).
25. Yamamoto, K., Kabir, M. H., and Tominaga, K. Terahertz time-domain spectroscopy of sulfur-containing biomolecules. *JOSA B*, **22**, 2417–2426 (2005).
26. Sharma, V., Crne, M., Park, J. O. and Srinivasarao, M. Structural origin of circularly polarized iridescence in jeweled beetles. *Science* **325**, 449–451 (2009).

Chapter 5

Optical Properties of Epitaxial Graphene Buffer Layer

5.1 Chapter introduction

Graphene, since its first isolation in 2004 [1,2], has been an emerging material for the realization of next-generation electronic and photonic devices, due to its many unique properties including ultimate atomic thickness, extremely high intrinsic carrier mobility and thermal conductivity [3]. Moreover, it has found promising applications in biochemistry [4] and biomedical engineering [5], and kirigami structures made of graphene have also been demonstrated [6]. Therefore, it is possible for us to use graphene to enhance the light interaction in the biological materials investigated in the previous chapters and integrate graphene with our existing kirigami modulators for improved spectroscopic performance.

However, one of the biggest hurdles for graphene for practical applications, especially as an electronic and optical material, is its lack of a bandgap [7]. Although many proposals, such as graphene quantum dots [8], graphene nanoribbons [9], strained graphene [10] and biased bilayer graphene [11], have been made to open such energy gap, they all require complex engineering of the graphene layer and have not been developed to produce a workable semiconducting form of graphene. More recently, new progress on the methods of the much simpler epitaxial growth has been shown to produce semiconducting graphene with a band gap larger than 0.5 eV [12,13]. Although some standard material characterization measurements and THz spectroscopy [14] have been performed for the preliminary investigation, the detailed optical properties and electron dynamics are still unknown, and ultrafast infrared spectroscopy is a more direct approach to determining the exact band gaps and other optical properties in these novel semiconductors.

In this chapter, I will describe the application of ultrafast infrared spectroscopy to the characterization of epitaxial graphene buffer layer on silicon carbide (SiC). The fabrication and the general properties of epitaxial graphene and buffer layer will be briefly introduced, followed by the description of self-built ultrafast time-resolved infrared spectrometer verified by the measurements of well-studied samples. The differential transmission and ultraviolet-visible (UV-Vis) absorption data of buffer layer graphene at room temperature are then presented as a potential evidence for the bandgap opening in this novel material. The further experiment at high temperature leads to the hypothesis that the bandgap opening in the buffer layer is induced by its interaction with SiC substrate and raising the temperature results in its phase transition from semiconducting form to a pristine graphene sheet.

This work was done in collaboration with Prof. Walter de Heer's group in the School of Physics at the Georgia Institute of Technology. The epitaxial graphene buffer layer samples were grown, and the high-temperature heating device was designed by Jean-Philippe Turmaud from de Heer group. I performed the UV-Vis absorption measurement, and the ultrafast infrared pump-probe measurements at both room temperature and high temperature.

5.2 Graphene and epitaxial graphene buffer layer

5.2.1 Brief introduction to graphene

Graphene is a monolayer of carbon atoms arranged in a two-dimensional (2D) hexagonal honeycomb lattice. Figure 5-1 (a) and (b) [15] show the physical lattice in real space and the corresponding Brillouin zone of graphene, respectively. The honeycomb lattice in real space can be decomposed into two equivalent triangular lattices, A and B, with a basis of an A-B pair of atoms per unit cell. The corresponding reciprocal lattice in wavevector space is also hexagonal with two sets of equivalent points, K and K', which are called Dirac points, at the corners of the graphene Brillouin zone (BZ). This equivalence gives rise to a valley degeneracy of two for the electrons, which is often referred to as pseudo-spin degeneracy. Combined with the real spin degeneracy of two, this gives a total degeneracy of four for the electrons in graphene.

In a conventional tight-binding model calculation [15,16], which includes both nearest and next-nearest neighbor atoms, the energy band structure has the form

$$E_{\pm}(\boldsymbol{k}) = \pm t\sqrt{3 + f(\boldsymbol{k})} - t' f(\boldsymbol{k}) \tag{5.1}$$

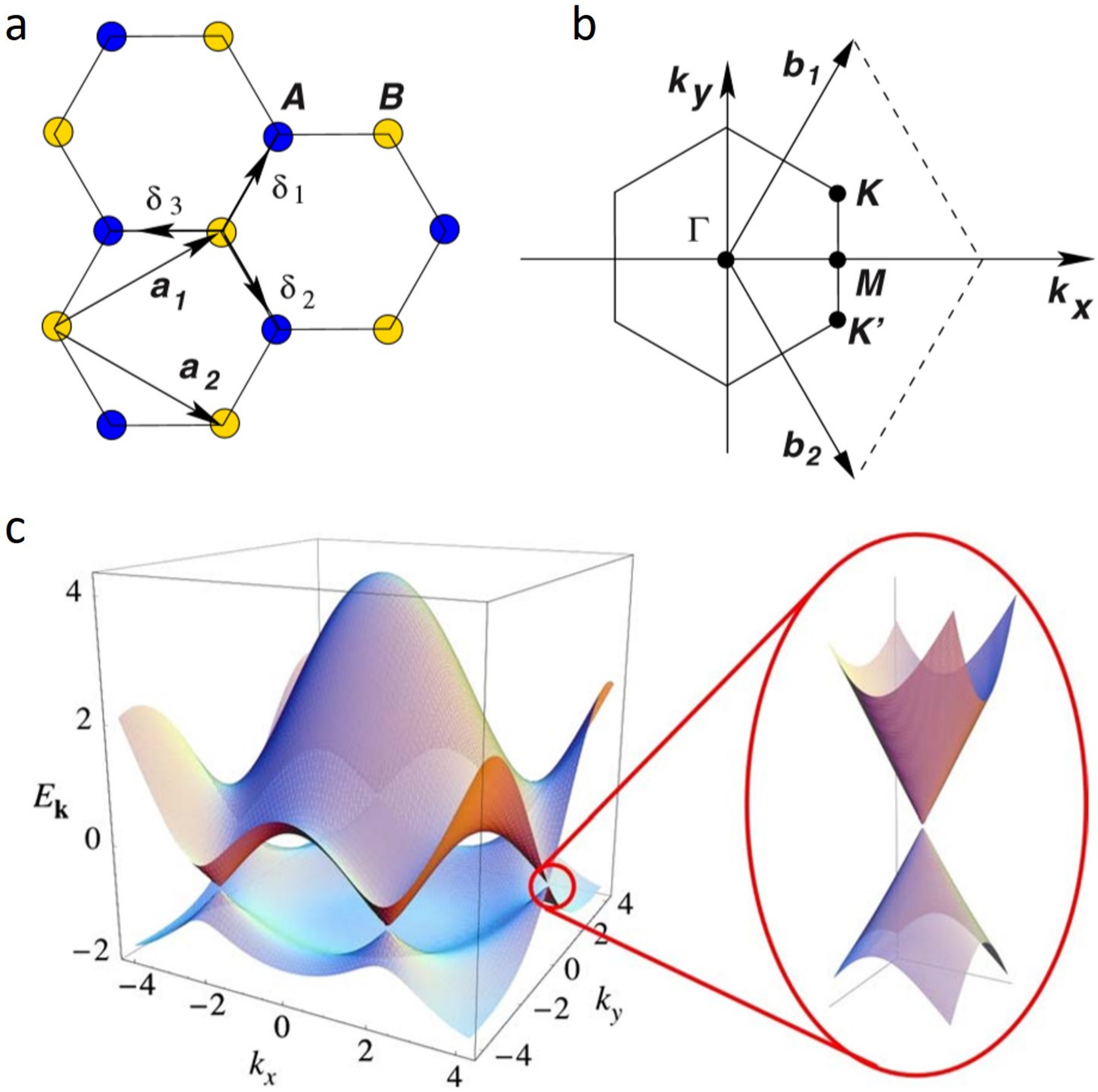

Figure 5-1. Structure and electronic dispersion of graphene. (a) Physical lattice in real space and (b) reciprocal lattice in wavevector space of graphene. (c) Energy band structure of graphene. Adapted from Ref. [15].

$$f(\boldsymbol{k}) = 2cos(\sqrt{3}k_y a) + 4cos(\frac{\sqrt{3}}{2}k_y a)cos(\frac{3}{2}k_x a) \tag{5.2}$$

where the plus and the minus sign applies to the upper (π or conduction) and the lower (π^* or valence) band, respectively, t($\approx$2.8 eV) and t' are the nearest and the next-nearest neighbor hopping energies, respectively, and $a\approx$1.42 Å is the carbon-carbon distance. The full calculated band structure is shown in Figure 5-1 (c). The most interesting feature of the band structure is that the conduction and valences bands touch at the Dirac points and the band structure is linear in the vicinity as shown in the red circle in Figure 5-1 (c). This makes graphene equivalent to a semi-metal with zero bandgap. The energy dispersion in the vicinity of the Dirac point is approximately given by

$$E_{\pm}(\boldsymbol{k}) = \pm v_F \boldsymbol{k} \tag{5.3}$$

where $v_F = 3ta/2 \approx 1 \times 10^6\ \mathrm{m/s}$ is the Fermi velocity. Consequently, the electrons in graphene move at the remarkably high (relativistic) Fermi velocity, which is only ~1/300 of the speed of light in vacuum, c, much like photons move in vacuum. The important implication is that the electron wavefunction in the vicinity of the Dirac point obeys the 2D Dirac equation

$$-iv_F \boldsymbol{\sigma} \cdot \nabla \varphi(\boldsymbol{r}) = E\varphi(\boldsymbol{r}) \tag{5.4}$$

Hence, the electrons in graphene are also termed Dirac electrons or Dirac fermions. Another interesting consequence of the linear energy dispersion in the vicinity of the Dirac point is that the light absorption of graphene is determined only by the fine structure constant, α=$e2/\hbar c$, and is completely independent of the light frequency [17].

5.2.2 Epitaxial graphene on SiC

Several techniques have been demonstrated for the synthesis of high-quality graphene, including mechanical exfoliation of graphite [2], chemical reduction of graphene oxide [18], chemical vapor deposition (CVD) [19] and thermal decomposition of silicon carbide [20]. The details of the fabrication methods and properties of exfoliated, chemically reduced and CVD graphene can be found in many resources, and this section only provides a general overview to epitaxial graphene on silicon carbide (SiC) which is related to the buffer layer samples studied in this chapter.

Silicon carbide is a wide band gap semiconductor with an indirect band structure and can be found in many different crystal structures which are also called polytypes [21]. The most commonly used polytypes for graphene growth are 4H and 6H hexagonal SiC with a band gap of 3.3 eV and 3.0 eV respectively. Cutting SiC perpendicular to the [0001] direction breaks the bonds between carbon and Si atoms, resulting in two inequivalent faces – the (0001) face, also known as Si-face, terminated by Si atoms and the $(000\overline{1})$ face, or C-face, terminated by C atoms. On both surfaces, epitaxial graphene can be formed by heating a piece of SiC substrate above 1000 °C in ultrahigh vacuum (UHV), causing preferential sublimation of silicon atoms from the surface and leaving behind carbon atoms rearranging themselves into graphene layers. However, the growth mechanisms and the graphene properties are very different between these two surfaces.

As the rate of sublimation of Si atoms is very high on the C-face of hexagonal SiC, it is difficult to control the growth of C-face epitaxial graphene even with improved methods. Therefore, most graphene films grown on the C-face are multilayer epitaxial graphene (MEG) ranging from a few up to a hundred layers. Unlike graphite whose layers are Bernal stacked [22], the individual layers in MEG are electronically decoupled due to their unique rotational stacking and each layer preserves the electronic structure of a monolayer graphene [23]. Monolayer C-face graphene can also be carefully produced with special fabrication process and it has no or minimal interaction with the substrate [24].

On the contrary, the growth of graphene on the Si-face happens at a much slower rate and layer by layer growth can be controlled very well [25]. In contrast to C-face graphene, the layers on the Si-face are Bernal stacked and therefore present the characteristics of thin graphite. The first layer is referred to as the “buffer layer”, as it does not display the properties of graphene. The layer growing on top of the buffer layer behaves as a single sheet of graphene, but its properties are still influenced by the substrate and the underlying buffer layer [26].

5.2.3 Graphene buffer layer on SiC(0001)

Buffer layer is the first graphene layer grown on the SiC(0001) Si-terminated surface and has its own unique characteristics. Recent studies on its atomic and electronic structures, as briefly summarized in Figure 5-2, indicate that it may be the long awaited ordered semiconducting form of graphene: first, by converting the buffer layer into a quasi-free-standing graphene layer using hydrogen intercalation, it is confirmed that the buffer layer is indeed structurally a continuous graphene layer [27,28]; X-ray reflectivity (XRR) and X-ray standing waves (XSW) measurements indicate a large hexagonal corrugation of 2.4 Å of the buffer layer possibly induced by the periodic interaction with the underlaying SiC [29]; with such interaction, scanning tunneling spectroscopy (STS) measurements consistently observe the presence of a ~1 eV gap in the density of states around the Fermi level [28,30]; the valence band dispersions have been resolved by angle-resolved photoemission spectroscopy (ARPES), showing a gap of ~0.5 eV between the Fermi level and the band maximum [12,31].

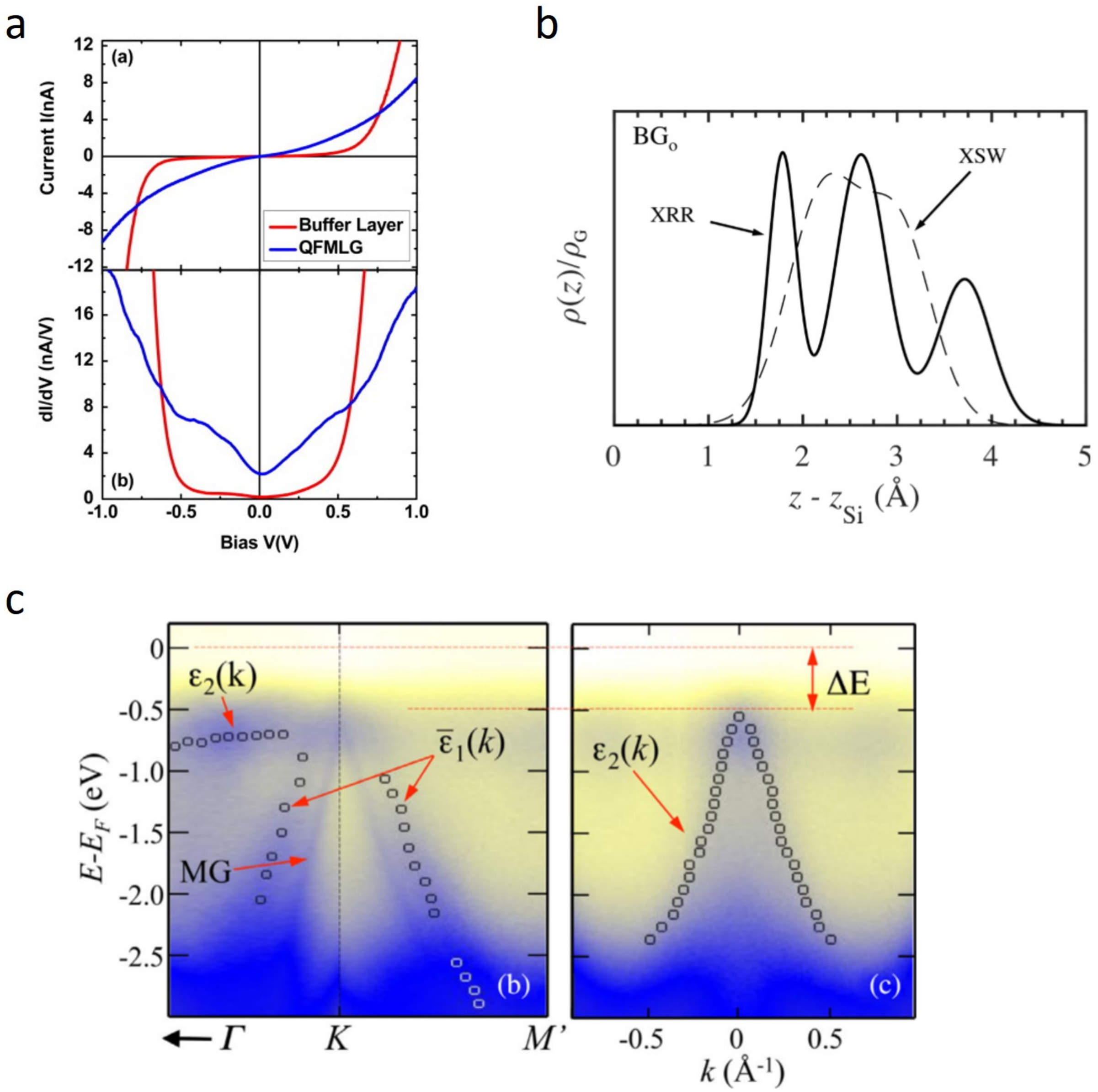

Figure 5-2. Atomic and electronic structures of graphene buffer layer. (a) Current vs. voltage (I–V) curves (top) and differential conductance spectra (bottom) acquired on the buffer layer (red line) and on quasi-free-standing monolayer graphene (QFMLG) obtained by hydrogen intercalation (blue line). Adapted from Ref. [28]. (b) buffer layer's vertical density distribution normalized to the density of a graphene layer, derived from XSW (dashed line) and XRR (solid line). Adapted from Ref. [29]. (c) valence band structures of buffer layer. Circles mark the peak positions of energy bands. A Dirac cone from a partial monolayer graphene (MG) on the top of the buffer layer is also shown. Adapted from Ref. [12].

Although these results provide some important insights on the structural and electronic properties of the epitaxial buffer layer, the research into this novel 2D material is still at its early stage: the conduction band structure and its position to the Fermi level (and hence the accurate bandgap) remain unknown; the origin of the bandgap opening and the nature of the interaction between buffer layer and SiC substrate are still controversial; and its optical properties and electron dynamics have not been studied at all. To shed more light on these problems, advanced optical characterization techniques are needed, and ultrafast infrared spectroscopy is one of the most powerful tools.

5.3 Ultrafast infrared spectroscopy

5.3.1 Ultrafast pump-probe spectroscopy

Ultrafast pump-probe spectroscopy is one of the most common ultrafast spectroscopic methods that measures the transient optical properties of materials, where carriers are excited from their equilibrium distribution by a pump pulse and then probed by a much weaker pulse at a variable time-delay achieved by a motorized linear stage. It provides insights not only on carrier dynamics with femtosecond temporal resolution but also on band structures and/or Fermi level with tunable photon energies. Time-resolved differential transmission $\Delta T/T$ and differential reflectivity $\Delta R/R$ are the two possible measurements, which respectively measure the induced transmission and reflection changes by the pump pulse and together permit the determination of the changes to the full complex refractive index or, equivalently, the complex dielectric constant, complex conductivity, and complex susceptibility [32].

Differential transmission is specifically used in this chapter, mainly because: 1) experimentally transmission setup is easier to build and align than reflection setup; 2) the experimental data of differential transmission is much easier to interpret as it is more directly related to the change in absorption caused by carrier population perturbation; and 3) it is totally compatible and works very well with the graphene samples on transparent substrates.

Quantitatively, the differential transmission $\Delta T/T(\hbar\omega_{probe}, t)$, as a function of both probe energy and time delay, is dependent on the initial and final wave function parities (i.e. the dipole matrix element M_{if}), the joint density of states (ρ_j), the electron occupancy of the initial subband (f_i) and the absence of an electron in the final subband ($1 - f_f$) where f is the Fermi-Dirac distribution function. Assuming the differential transmission is totally caused by the change in absorption, which is given by [32]

$$\Delta\alpha(\hbar\omega_{probe}) = |M_{if}|^2 \times \rho_j(\hbar\omega_{probe}) \times \{f_i(t)[1 - f_f(t)]\} \tag{5.5}$$

the resulting differential transmission for a thin film of thickness d is [33]

$$\Delta T/T(\hbar\omega_{probe}, t) \approx -\Delta\alpha \times d_{sample}$$
$$= -d_{sample} \times |M_{if}|^2 \rho_j(\hbar\omega_{probe}) f_i(t)[1 - f_f(t)] \tag{5.6}$$

where the first approximation is valid under the condition that $\Delta T/T$ for thin samples, such as graphene, is usually on the order of 10^{-4} to 10^{-3}. The negative sign indicates that an increase (decrease) in absorption results in a decrease (increase) in transmission i.e. a negative (positive) $\Delta T/T$ signal. As shown by the equation, the time dependence of the differential transmission signal originates in the time-dependent occupancy of the initial $f_i(t)$ and final $f_f(t)$ subbands probed by $\hbar\omega_{probe}$, therefore resolving the temporal dynamics of the carriers.

5.3.2 Experimental setup of infrared pump-probe spectroscopy

Figure 5-3 shows the schematic of our self-built non-degenerate infrared (IR) pump-probe spectrometer using the femtosecond pulses generated from the ultrafast laser system operating at 250 kHz repetition rate as previously discussed in Section 1.2. The remnant 800 nm from the optical parametric amplifier (OPA) functions as the pump and is recompressed to ~100 fs pulse duration by a pair of prisms. The probe beam is either the signal (1.2 μm – 1.6 μm) or idler (1.6 μm – 2.4 μm) generated by OPA with a pulse duration of ~200 fs after passing all the optical elements. The exact probe energy/wavelength is selected and tuned by a wheel of bandpass filters with 10 nm to 20 nm FWHM (filters below 1.7 μm from Thorlabs, above 1.7 μm from Spectrogon US). The pump and probe beams are combined and spatially overlapped by a long-pass dichroic mirror (DMLP1180, Thorlabs), and focused by two separate lenses to spot sizes of 300 μm and 80 μm respectively at the sample position. Their fluences are controlled by two attenuators to be ~60 μJ/cm^2 for the pump and ~5 μJ/cm^2 for the probe. A motorized linear stage (ILS100HA, Newport) is in the pump path to adjust the relative time delay between the two pulses. After the sample a long-pass filter (FELH1150, Thorlabs) blocks the 800 nm pump beam and is followed by an InGaAs photodetector (DET10D, Thorlabs) which measures the intensity of the transmitted IR probe pulse. A lock-in detection scheme is applied to achieve high signal-to-noise ratio for the sensitive measurement, with a mechanical chopper system (MC1000, Thorlabs) modulating the power of the pump beam to be “on” and “off” at 1 kHz and synchronizing the reference frequency to a lock-in amplifier (SR850, Stanford Research Systems) for the differential transmission measured by the detector. The probe beam can also be redirected into an infrared spectrometer (Acton SP2300, Princeton Instruments) for the measurement of the OPA spectrum.

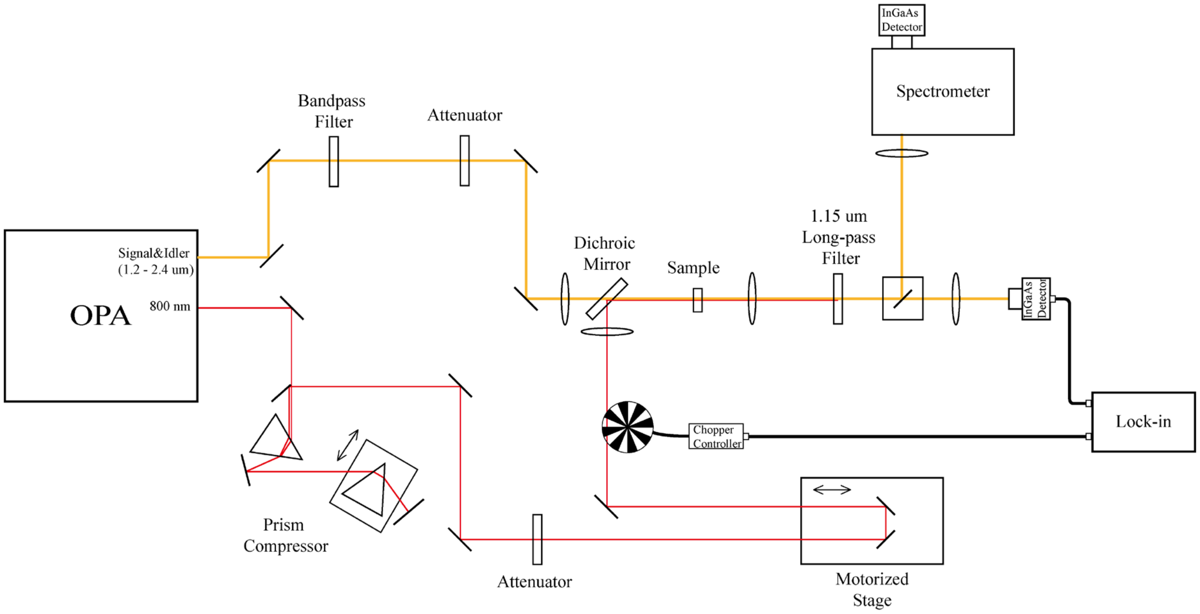

Figure 5-3. Schematic of non-degenerate ultrafast infrared pump-probe setup. An additional beam path directed into a spectrometer is also included for the measurement of the OPA spectrum.

5.3.3 Verification of pump-probe setup

To verify the effectiveness of the experimental setup on resolving the carrier dynamics and determining the Fermi levels and/or bandgaps, as well as to initially check the temporal and spatial alignment, time-resolved differential transmission measurements are performed on several graphene samples that have already been well studied, including epitaxial multilayer graphene and CVD graphene.

The first test sample is a 30-layer epitaxial graphene grown on C-face of SiC, and the exactly same sample measured and published by former group members [34,35]. Figure 5-4 shows the experimental results of its differential transmission with two different probe wavelengths – 1300 nm for (a) and 1811 nm for (b). The important features in these curves, including the double peaks due to the substrate reflection and the fitted relaxation times in Figure 5-4 (a) and the sign change at ~1 ps caused by the interlayer energy transfer in Figure 5-4 (b), are very consistent with the previous data measured with other pump-probe spectrometers [34,35].

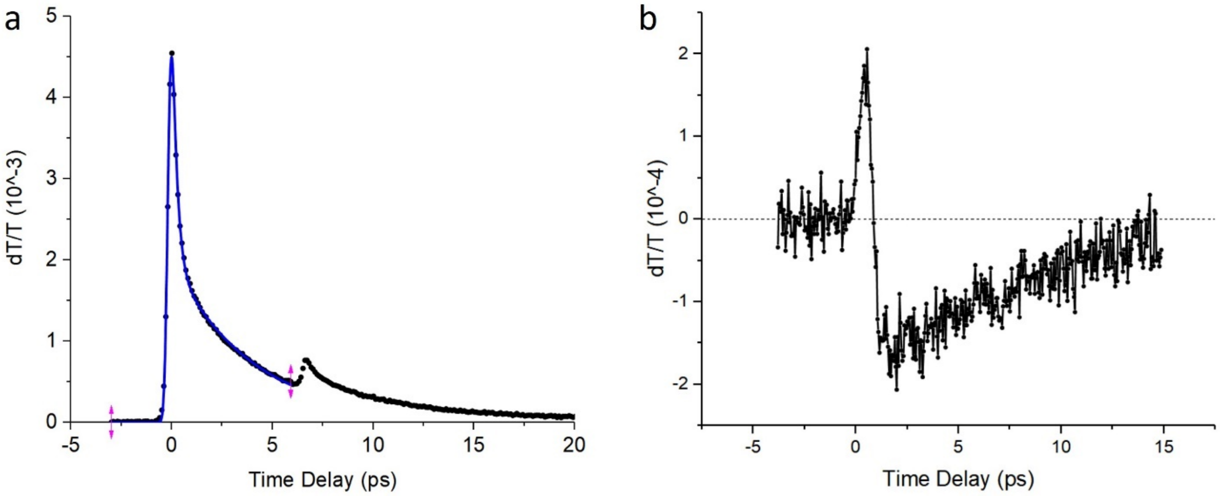

Figure 5-4. Experimental results of the differential transmission for an epitaxial graphene sample with ~30 layers. (a) 1300-nm probe. The black circles are experimental data and the blue curve is biexponential fit up to 6 ps with a 234-fs short delay and a 4-ps long delay. The second small peak at ~7 ps is due to the reflection of the pump pulse inside the SiC substrate. (b) 1811-nm probe. The sign changes in the differential transmission at ~1 ps due to the interlayer energy transfer [35].

The second test sample is a chemically p-doped CVD monolayer graphene, the same sample used in [36]. Figure 5-5 shows the experimental results of its differential transmission with probe wavelengths tuned from 1200 nm to 1500 nm. The biexponential fits give a decay time of ~2 ps after the first a few hundred femtosecond thermalization, which is the characteristic timescale for carrier relaxation in monolayer graphene [37,38]. The sign of the differential transmission changes from positive at 1300 nm to negative at 1400 nm because the interband transition caused by the probe pulse crosses the Fermi level [38]. Combined with the result that the peak magnitude at 1300 nm is much smaller than that at 1400 nm, it can be deduced that the Fermi level of this graphene sample is slightly less than 477 meV (half of the photon energy with 1300 nm) below the Dirac point, which is matching the value 530 meV measured by ellipsometry [36] considering the doping decays over the time between these two measurements.

These two sets of test measurements are both consistent with the published work, therefore can confirm the alignment of the setup and verify its effectiveness of resolving the carrier dynamics and determining Fermi levels and/or bandgaps of novel materials.

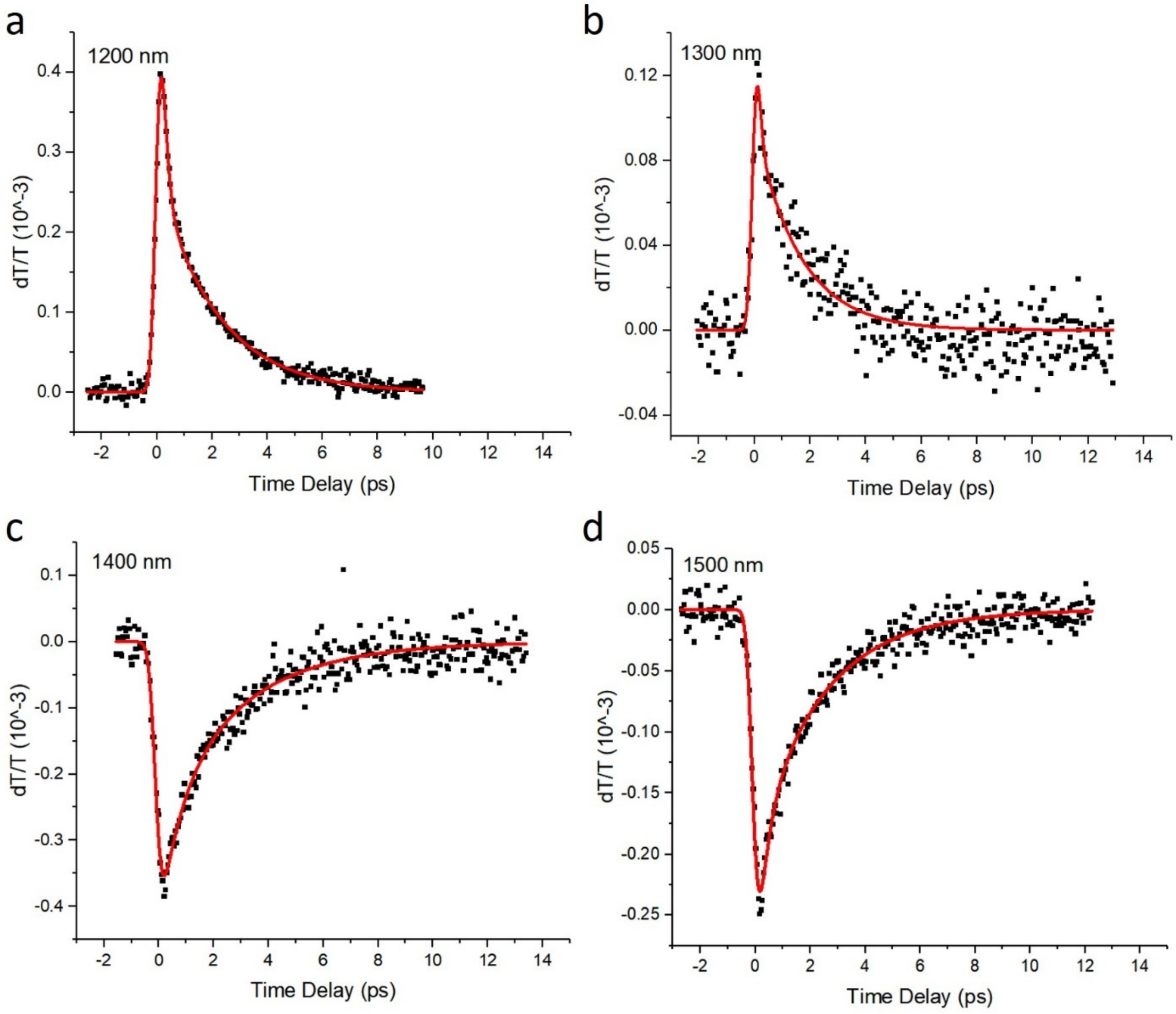

Figure 5-5. Experimental results of the differential transmission for a heavily p-doped CVD monolayer graphene with different probe wavelengths – (a) 1200 nm, (b) 1300 nm, (c) 1400 nm and (d) 1500 nm. Black squares are experimental data and the red curves are biexponential fits with a short decay time of a few hundred fs and a long decay time of ~2 ps for all wavelengths.

5.3.4 Heating system for high-temperature experiment

As an attempt to convert the buffer layer into a quasi-free-standing graphene layer and to test the hypothesis that the bandgap opening is induced by the interaction between buffer layer and the substrate, a heating system is designed and built to elevate the sample temperature to above 1000 °C. The system is compatible with the optical pump-probe setup and is shown in Figure 5-6. The buffer layer sample is held vertically inside a graphite crucible with openings of ~3 mm diameter on both sides to let laser beams through. The crucible and sample are heated by induction coil which together with the power supply is cooled down through water lines. The crucible is placed inside a quartz tube which can be connected to helium gas tank and vacuum pumps to provide a clean and inert environment for the sample. A small fan keeps the quartz tube, brass connector and silicone sealant cool to prevent the sealed chamber cracking. A handheld pyrometer reads the temperature of the heated sample.

The first step of the experiment is to pump down the tube by a turbo pumping system to ~10^{-6} Torr and anneal the sample at 300 °C for about 30 min. Then grade 6.0 (purity 99.9999%) helium gas is bled into the chamber and subsequently pumped away to flush out the contaminants released from the sample, crucible and tube during annealing. This "pump-and-flush" process is repeated for a couple of times while the sample is kept at 300°C to ensure a clean environment inside the chamber. After that the chamber is filled with helium gas with a slight overpressure and cooled down for the room-temperature measurement. Then, the induction power is gradually turned up with the sample temperature monitored by the handheld pyrometer to about 1000 °C for the high-temperature measurement.

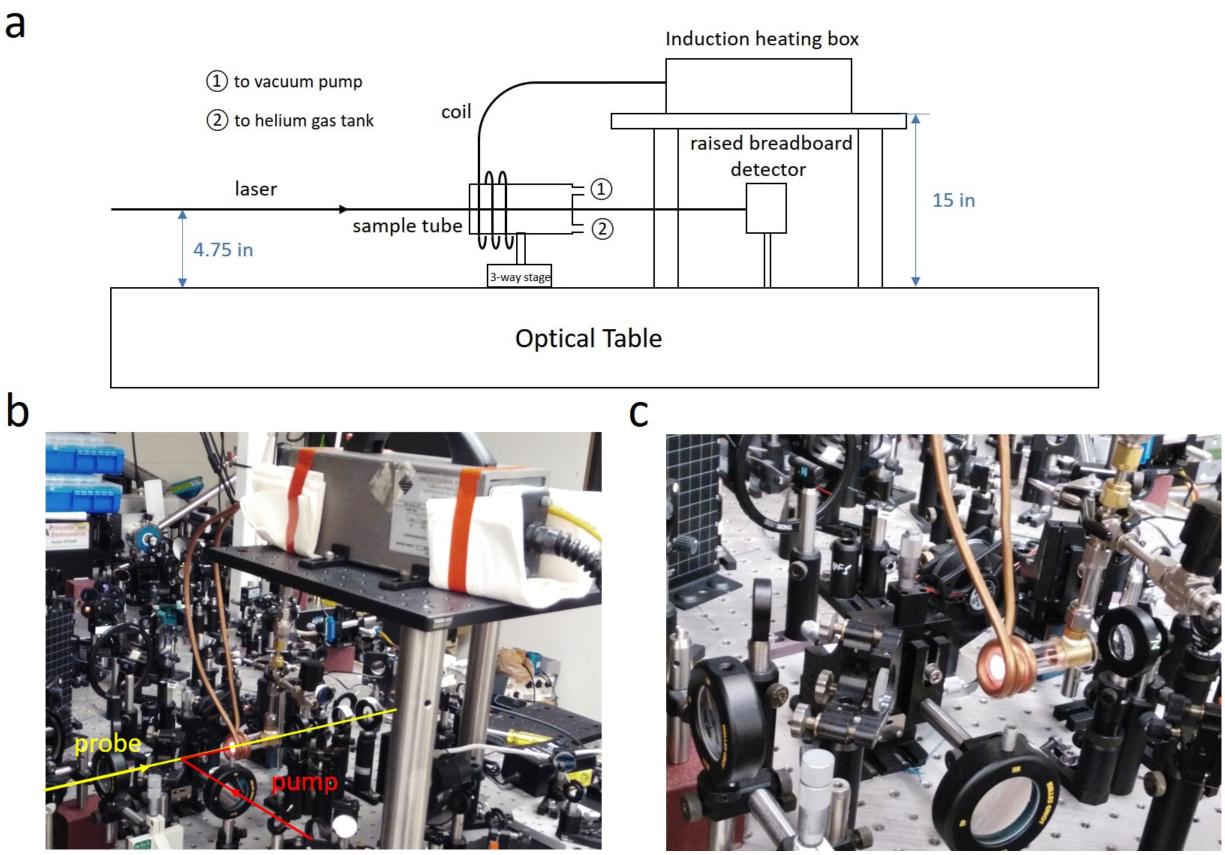

Figure 5-6. Sample heating system integrated with infrared pump-probe spectrometer. (a) Schematic of the heating system. (b) and (c) Photos of the actual system. The glowing part at the center of the tube is the heated graphite crucible.

5.4 Experimental results of graphene buffer layer

The graphene buffer layer samples used in this study are grown by the confinement controlled sublimation (CCS) process, an improved growth method developed and used at Georgia Institute of Technology [39], on the Si-face of undoped 4H SiC substrate. The C-face graphene at the back of the samples are removed via O2 etching. The structural and electrical characterization are carried out by my collaborator Jean-Philippe Turmaud, and the experimental results are presented in [40]. Here we discuss the optical experimental results. All the following experiments are performed on two samples and they generate reproducible results.

5.4.1 Infrared pump-probe measurement at room temperature

Infrared pump-probe spectroscopy is first performed on the samples at room temperature both before and after annealing with several different probe wavelengths. Figure 5-7 shows the summary of these experimental results. Strikingly, no conventional "graphene-like" signals as those shown in Figure 5-4 and Figure 5-5 are observed. Instead, the buffer layer samples at room temperature exhibit a negative sharp peak around zero-time delay for probe wavelengths shorter than 1500 nm both before and after annealing. To have a closer look at this peak, a finer scan with much smaller step size is performed. As shown in Figure 5-7 (b), the negative peak is symmetric and can be well fitted by a Gaussian function with FWHM of 295 fs. Based on this, we believe this differential transmission signal comes from a two-photon absorption (one 800 nm pump photon and one IR probe photon) by the buffer layer sample resulting in a cross-correlation between the pump and probe pulses. A measurement with longer probe wavelength of 2400 nm shows just noises with no such negative peak as shown in Figure 5-7 (c). This leads us to hypothesize the existence of separated image potential states [40,41] or a bandgap opening of 2 eV (total energy of a 800 nm photon and a 2400 nm photon) to 2.4 eV (total energy of a 800 nm photon and a 1500 nm photon) in the buffer layer.

It should also be noted that the signal after annealing in Figure 5-7 (d) is smaller than that before annealing in Figure 5-7 (a), whose underlying reason – either that the defects contribute a part of the signal or that the laser alignment shifts during the annealing process (especially influenced by the vibrations of pumping process) – remains unclear and requires more measurements and further investigation.

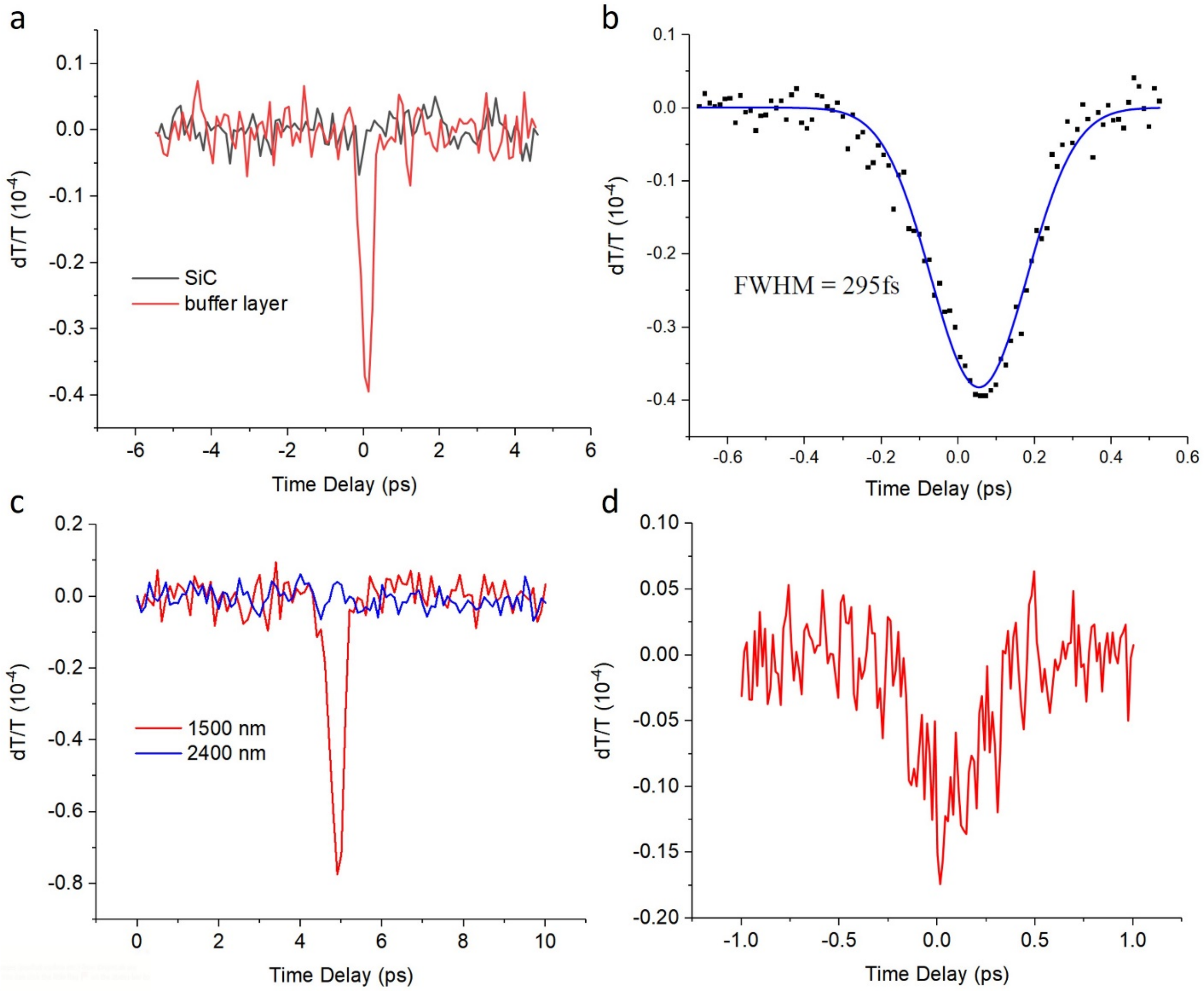

Figure 5-7. Experimental results of differential transmission of graphene buffer layer at room temperature. (a) Coarse scans of SiC substrate and buffer layer sample before annealing with probe wavelength of 1300 nm. (b) Fine scan of buffer layer before annealing with probe wavelength of 1300 nm. The black squares are experimental data and the blue curve is the Gaussian fit with FWHM of 295 fs. (c) Coarse scans of buffer layer before annealing with two different probe wavelengths – 1500 nm and 2400 nm. (d) Fine scan of buffer layer after annealing with probe wavelength of 1300 nm. The step sizes for coarse scan and fine scan are 100 fs and 13.3 fs, respectively. All experimental data are averaged over 10 measurements.

5.4.2 UV-Vis absorption at room temperature

A more straightforward and simpler method to check if a visible transition exists is ultraviolet-visible (UV-Vis) spectroscopy which measures the transmission or absorption of a sample in part of the ultraviolet and the full, adjacent visible spectral regions. The experimental results of our buffer layer samples at room temperature, as shown in Figure 5-8, are obtained by a commercial UV-Vis spectrometer with spectral range from 190 nm to 1100 nm (UV-1601, Shimadzu). As can be seen from Figure 5-8 (a), the absolute absorptions of the buffer layer sample and the SiC substrate are almost identical for wavelengths above 600 nm; below 600 nm, however, the absorption of buffer layer becomes larger than that of the SiC substrate. It should also be pointed out that the huge absorption below ~380 nm in both samples is due to the interband transition of the 4H SiC substrate with a bandgap of 3.23 eV, therefore not of interest to us. To make the comparison more direct, relative absorption is calculated by taking the ratio of the absolute absorptions of buffer layer and pure SiC substrate, and is shown in Figure 5-8 (b). As expected, an increasing absorption appears with shorter wavelengths starting from ~600 nm. All these results potentially indicate that a transition or a bandgap larger than 2 eV may exist in the graphene buffer layer, which is consistent with the result obtained from the above pump-probe measurement.

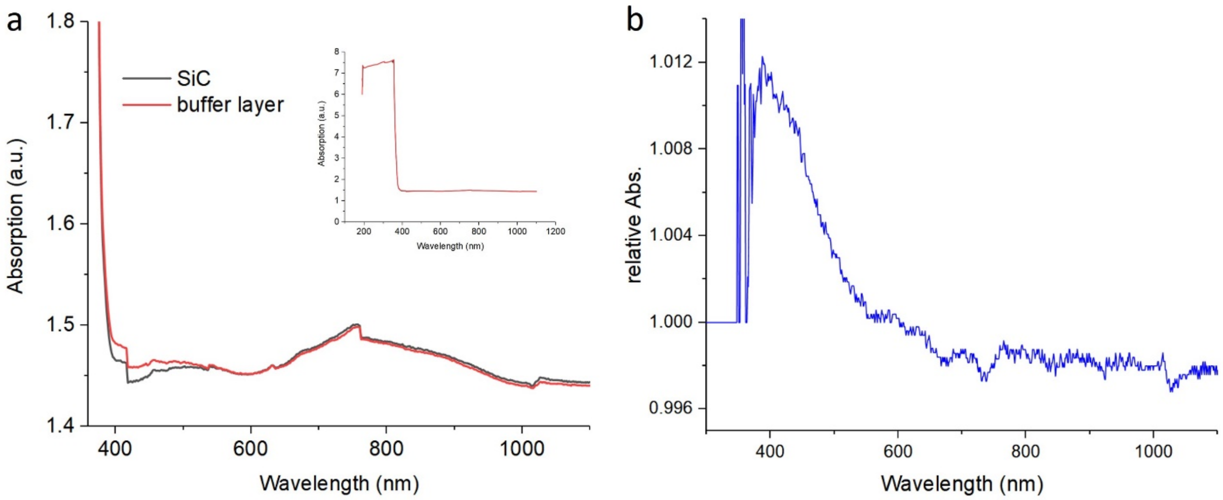

Figure 5-8. Experimental results of UV-Vis absorption of graphene buffer layer and SiC substrate at room temperature. (a) Absolute absorption of buffer layer and SiC substrate in the spectral range of interest. The inset figure shows the full spectrum with saturated absorption by SiC. (b) Relative absorption between buffer layer and pure SiC substrate. Again, the strong fluctuation and saturation below 380 nm is due to the large absorption by SiC.

5.4.3 Infrared pump-probe measurement at high temperature

Based on previous structural and electronic transport measurements, a model of localization and image potential is proposed by our collaborators at Georgia Tech, which views the buffer layer as a corrugated graphene layer on the top of SiC without involving any sp^3 hybridization [40]. This model predicts a series of image potential states [41] or a bandgap opening in buffer layer, and also indicate that it should be easy to decouple such a graphene buffer layer from the substrate as observed by many experiments on intercalation [27,28]. Therefore, it is a reasonable hypothesis that the buffer layer is a free-standing graphene layer that turns into a periodically corrugated layer upon cooling down due to the interaction with the substrate, and this process can be reversed by raising the temperature to return the buffer layer into free-standing graphene at higher thermal energy.

To verify the hypothesis, the buffer layer sample is heated to 1000 °C after annealing and pump-probe measurements are taken. Figure 5-9 shows the experimental results of its differential transmission. Clearly, they are totally different from the results obtained at room temperature presented in Figure 5-7. More importantly, these curves of buffer layer at high temperature are very similar to those of true graphene layers as shown in Figure 5-4 and Figure 5-5 in terms of general curve shapes and the relaxation timescale; the much reduced differential transmission magnitude and the relatively shorter decay time can be explained by a higher lattice temperature [42] and increased electron-phonon coupling [43,44]. These results are all consistent with our hypothesis and could be a strong evidence that the corrugated buffer layer has been lifted into a free-standing graphene layer at high temperature.

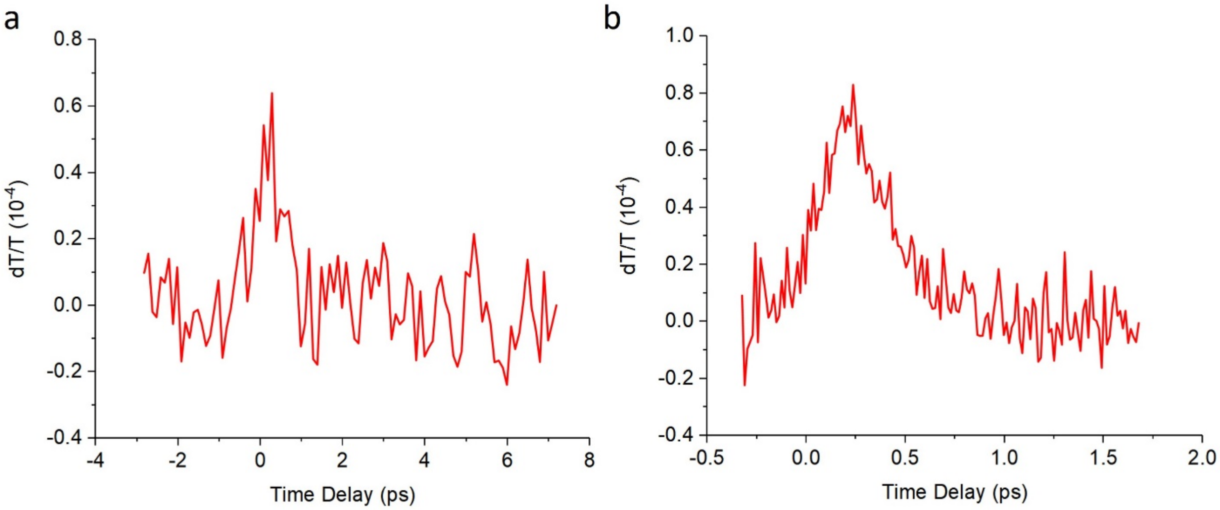

Figure 5-9. Experimental results of differential transmission of graphene buffer layer at 1000 °C. (a) Coarse scan with step size of 100 fs for larger temporal range. The curve is averaged over 20 scans. (b) Fine scan with step size of 13.3 fs but shorter temporal range. The curve is averaged over 30 scans. The probe wavelength is 1300 nm.

A more convincing result to support our hypothesis would be that the original differential transmission signal in Figure 5-7 would show up again when the temperature was dropped from 1000 °C back to room temperature, indicating the two-way phase transition between semiconducting and semi-metal graphene forms of the buffer layer. Unfortunately, however, this has not been observed experimentally yet. From the experimental data measured at room temperature after heating the buffer layer to 1000 °C, as shown in Figure 5-10, the differential transmission signal remains similar to that of CVD graphene, which means the room-temperature buffer layer after heating is not the same as the original form before heating. By a biexponential fitting to the curve, it turns out that the actual relaxation time of this buffer layer is 1.2 ps which is shorter than the characteristic decay time of ~2 ps for a pristine graphene layer. Based on these results, we believe that the buffer layer sample is intercalated by contaminants during the high temperature heating process, resulting in an inhomogeneous graphene layer after cooling down. This claim is further justified by the subsequent measurement of Raman spectroscopy showing a strong D-peak which indicates disorder – defects and/or edges [45] – in the final cooled-down buffer layer sample. This intercalation may be caused by the insufficiency of vacuum pumping system which fails to produce and maintain enough vacuum condition or by any unnoticed leakage at the connections of the quartz tube. In order to verify our hypothesis of the two-way phase transition and the image potential model, an improvement or a redesign of the heating system is required for future experiments.

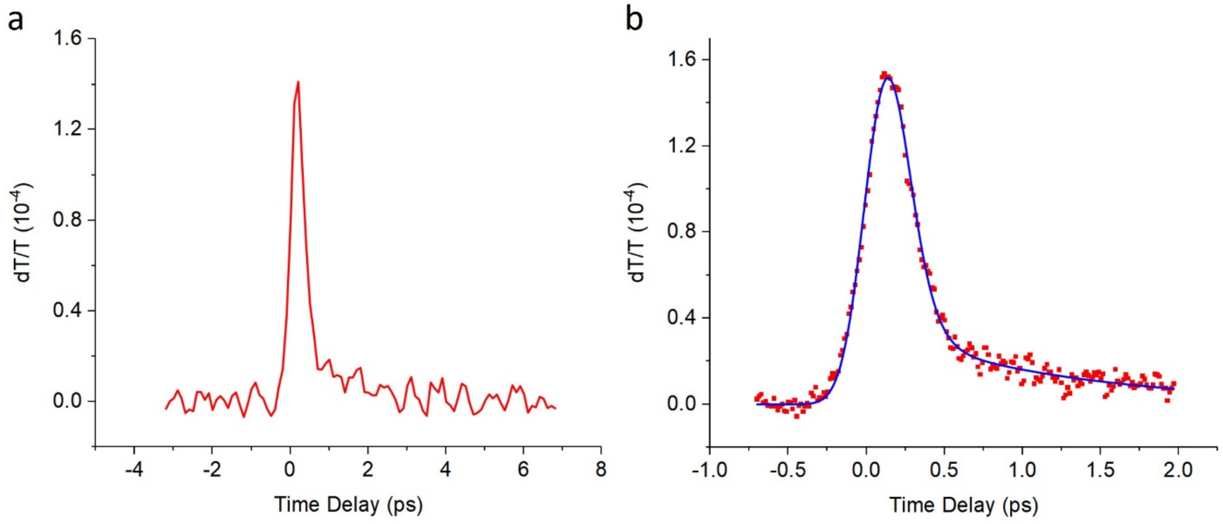

Figure 5-10. Experimental results of differential transmission of graphene buffer layer at room temperature after heated to 1000 °C. (a) Coarse scan with step size of 100 fs for larger temporal range. (b) Fine scan with step size of 13.3 fs but shorter temporal range. The red squares are experimental data and the blue curve is biexponential fit with a short decay time of 82 fs and a long decay time of 1.2 ps. Both scans are averaged over 20 measurements and the probe wavelength is 1300 nm.

5.5 Summary

Ultrafast infrared pump-probe spectroscopy has been used as the main tool for the optical characterization of the graphene buffer layer on SiC(0001), both at room temperature and high temperature. At room temperature, buffer layer shows totally different ultrafast response from that of normal graphene layers. Together with the results from UV-Vis spectroscopy, it is proposed that separated states or a bandgap opening between 2 eV and 2.4 eV exist in buffer layer at room temperature due to the interaction with SiC substrate. For high temperature experiment, a self-developed heating system has been demonstrated to be compatible with optical pump-probe setup and able to heat sample above 1000 °C on an optical table. Preliminary experimental results are consistent with the hypothesis that buffer layer can be decoupled from the substrate into a free-standing graphene layer at elevated temperature, although an improvement of the current heating system is required to avoid intercalation and more experiments are needed to fully understand the electronic and optical properties of buffer layer and their underlying mechanisms.

Reference

1. Novoselov, K. S., Geim, A. K., Morozov, S. V., Jiang, D., Zhang, Y., Dubonos, S. V., Grigorieva, I. V. and Firsov, A. A. Electric field effect in atomically thin carbon films. *Science*, **306**, 666-669 (2004).
2. Novoselov, K. S. A., Geim, A. K., Morozov, S., Jiang, D., Katsnelson, M., Grigorieva, I. V., Dubonos, S. V. and Firsov, A. Two-dimensional gas of massless Dirac fermions in graphene. *Nature*, **438**, 197-200 (2005).
3. Du, X., Skachko, I., Barker, A., and Andrei, E. Y. Approaching ballistic transport in suspended graphene. *Nat. Nanotechnol.*, **3**, 491, (2008).
4. Xiang, Q., and Yu, J. Graphene-based photocatalysts for hydrogen generation. *J. Phys. Chem. Lett.*, **4**, 753-759, (2013).
5. Chung, C., Kim, Y. K., Shin, D., Ryoo, S. R., Hong, B. H., and Min, D. H. Biomedical applications of graphene and graphene oxide. *Acc. Chem. Res.*, **46**, 2211-2224, (2013).
6. Blees, M. K., et al. Graphene kirigami. *Nature*, **524**, 204, (2015).
7. Zhou, S. Y., et al. Substrate-induced bandgap opening in epitaxial graphene. *Nat. Mater.*, **6**, 770, (2007).
8. Trauzettel, B., Bulaev, D. V., Loss, D., and Burkard, G. Spin qubits in graphene quantum dots. *Nat. Phys.*, **3**, 192, (2007).
9. Han, M. Y., Özyilmaz, B., Zhang, Y., and Kim, P. Energy band-gap engineering of graphene nanoribbons. *Phys. Rev. Lett.*, **98**, 206805, (2007).
10. Ni, Z. H., Yu, T., Lu, Y. H., Wang, Y. Y., Feng, Y. P., and Shen, Z. X. Uniaxial strain on graphene: Raman spectroscopy study and band-gap opening. *ACS nano*, **2**, 2301-2305, (2008).
11. Oostinga, J. B., Heersche, H. B., Liu, X., Morpurgo, A. F., and Vandersypen, L. M. Gate-induced insulating state in bilayer graphene devices. *Nat. Mater.*, **7**, 151, (2008).
12. Nevius, M. S., et al. Semiconducting graphene from highly ordered substrate interactions. *Phys. Rev. Lett.*, **115**, 136802, (2015).
13. Wang, F., et al. Wide-gap semiconducting graphene from nitrogen-seeded SiC. *Nano Lett.*, **13**, 4827-4832, (2013).
14. Mihnev, M. T., et al. Evidence for bandgap opening in buckled epitaxial graphene from ultrafast time-resolved terahertz spectroscopy. *Appl. Phys. Lett.*, **107**, 173107, (2015).
15. Neto, A. C., Guinea, F., Peres, N. M., Novoselov, K. S., and Geim, A. K. The electronic properties of graphene. *Rev. Mod. Phys.*, **81**, 109, (2009).
16. Wallace, P. R. The band theory of graphite. *Phys. Rev.*, **71**, 622. (1947).
17. Nair, R. R., et al. Fine structure constant defines visual transparency of graphene. *Science*, **320**, 1308-1308, (2008).

18. Gómez-Navarro, C., Weitz, R. T., Bittner, A. M., Scolari, M., Mews, A., Burghard, M., and Kern, K. Electronic transport properties of individual chemically reduced graphene oxide sheets. *Nano Lett.*, **7**, 3499-3503, (2007).
19. Mattevi, C., Kim, H., and Chhowalla, M. A review of chemical vapour deposition of graphene on copper. *J. Mater. Chem.*, **21**, 3324-3334, (2011).
20. De Heer, W. A., et al. Epitaxial graphene. *Solid State Commun.*, **143**, 92-100, (2007).
21. Nakashima, S. I., and Harima, H. Raman investigation of SiC polytypes. *Phys. Status Solidi A*, **162**, 39-64. (1997).
22. Bernal, J. D. The structure of graphite. *Proc. R. Soc. A*, **106**, 749-773, (1924).
23. Hass, J., et al. Why multilayer graphene on 4H−SiC ($000\overline{1}$) behaves like a single sheet of graphene. *Phys. Rev. Lett.*, **100**, 125504, (2008).
24. Hu, Y., et al. Structured epitaxial graphene: growth and properties. *J. Phys. D*, **45**, 154010, (2012).
25. Riedl, C., Coletti, C., and Starke, U. Structural and electronic properties of epitaxial graphene on SiC (0001): a review of growth, characterization, transfer doping and hydrogen intercalation. *J. Phys. D*, **43**, 374009, (2010).
26. Bostwick, A., Ohta, T., Seyller, T., Horn, K., and Rotenberg, E. Quasiparticle dynamics in graphene. *Nat. Phys.*, **3**, 36, (2007).
27. Riedl, C., Coletti, C., Iwasaki, T., Zakharov, A. A., and Starke, U. Quasi-free-standing epitaxial graphene on SiC obtained by hydrogen intercalation. *Phys. Rev. Lett.*, **103**, 246804, (2009).
28. Goler, S., et al. Revealing the atomic structure of the buffer layer between SiC(0001) and epitaxial graphene. *Carbon*, **51**, 249-254, (2013).
29. Conrad, M., et al. Structure and evolution of semiconducting buffer graphene grown on SiC (0001). *Phys. Rev. B*, **96**, 195304, (2017).
30. Baringhaus, J., et al. Exceptional ballistic transport in epitaxial graphene nanoribbons. *Nature*, **506**, 349, (2014).
31. Emtsev, K. V., Speck, F., Seyller, T., Ley, L., and Riley, J. D. Interaction, growth, and ordering of epitaxial graphene on SiC {0001} surfaces: A comparative photoelectron spectroscopy study. *Phys. Rev. B*, **77**, 155303, (2008).
32. Prasankumar, R. P., and Taylor, A. J. (Eds.). *Optical techniques for solid-state materials characterization*. CRC Press. (2016).
33. Ganikhanov, F., Burr, K. C., Hilton, D. J., and Tang, C. L. Femtosecond optical-pulse-induced absorption and refractive-index changes in GaAs in the midinfrared. *Phys. Rev. B*, **60**, 8890, (1999).
34. Sun, D., et al. Ultrafast relaxation of excited Dirac fermions in epitaxial graphene using optical differential transmission spectroscopy. *Phys. Rev. Lett.*, **101**, 157402, (2008).
35. Mihnev, M. T., et al. Electronic cooling via interlayer Coulomb coupling in multilayer epitaxial graphene. *Nat. Commun.*, **6**, 8105, (2015).

36. Chang, Y. C., Liu, C. H., Liu, C. H., Zhong, Z., and Norris, T. B. Extracting the complex optical conductivity of mono-and bilayer graphene by ellipsometry. *Appl. Phys. Lett.*, **104**, 261909, (2014).
37. Wang, H., et al. Ultrafast relaxation dynamics of hot optical phonons in graphene. *Appl. Phys. Lett.*, **96**, 081917, (2010).
38. Luo, C. W., Tseng, P. S., Chen, H. J., Wu, K. H., and Li, L. J. Dirac fermion relaxation and energy loss rate near the Fermi surface in monolayer and multilayer graphene. *Nanoscale*, **6**, 8575-8578, (2014).
39. De Heer, W. A., et al. Large area and structured epitaxial graphene produced by confinement controlled sublimation of silicon carbide. *Proc. Natl. Acad. Sci. U.S.A.*, **108**, 16900-16905, (2011).
40. Turmaud, J. P. *Variable range hopping conduction in the epitaxial graphene buffer layer on SiC (0001)*. Doctoral dissertation, Georgia Institute of Technology, (2018).
41. Shearer, A. J., Johns, J. E., Caplins, B. W., Suich, D. E., Hersam, M. C., and Harris, C. B. Electron dynamics of the buffer layer and bilayer graphene on SiC. *Appl. Phys. Lett.*, **104**, 231604, (2014).
42. Anisimov, S. I., Kapeliovich, B. L., and Perelman, T. L. Electron emission from metal surfaces exposed to ultrashort laser pulses. *Zh. Eksp. Teor. Fiz*, **66**, 375-377, (1974).
43. Hwang, E. H., and Sarma, S. D. Acoustic phonon scattering limited carrier mobility in two-dimensional extrinsic graphene. *Phys. Rev. B*, **77**, 115449, (2008).
44. Efetov, D. K., and Kim, P. Controlling electron-phonon interactions in graphene at ultrahigh carrier densities. *Phys. Rev. Lett.*, **105**, 256805, (2010).
45. Ferrari, A. C. Raman spectroscopy of graphene and graphite: disorder, electron–phonon coupling, doping and nonadiabatic effects. *Solid State Commun.*, **143**, 47-57, (2007).

Chapter 6

Conclusions and Future Work

In this thesis, several new methods for THz and ultrafast IR spectroscopy have been developed and applied for the studies of various biological materials and novel 2D materials. In this chapter, the conclusions are summarized and the future directions are discussed for each project.

6.1 THz time-domain polarimetry

In Chapter 2, a new method for THz time-domain polarimetry (THz-TDP) applicable to any generalized anisotropic and/or chiral materials is developed, based on the conventional THz time-domain spectroscopy (THz-TDS) with three additional linear polarizers. Complete data processing procedure and optical property derivations are presented together with the experimental setup. Compared to the conventional THz-TDS, the advantages of the new THz-TDP include: it generates information about anisotropic and chiral properties which are not accessible by THz-TDS; it gives more accurate transmission/absorption for complex materials; it is much less susceptible to environment especially humidity; it is totally compatible to the conventional THz-TDS setup therefore requires no major modifications. The accuracy and effectiveness of the new method are demonstrated and justified by the measurements of several test samples including anisotropic polymer sheet and chiral DNA solutions. As an important biomolecule, DNA shows negative circular dichroism (CD) below 0.8 THz which has not been observed before and is believed to be the first THz CD spectrum ever measured on biomolecules.

The future work for the THz-TDP method would be to improve its accuracy and precision. Until now, all the rotations of the polarizers are operated manually, which is very prone to human errors and cannot guarantee the same polarizer orientations over many scans leading to reduced accuracy and precision. Improvement can be achieved by mounting the polarizers onto motorized rotational stages and integrating these stages into current data control and acquisition program for complete automatic operation. The motorized stages can ensure very high precision hence better sensitivity, and can also reduce the operation interval during each scan which is critical for unstable or quickly changing samples such as chemical reactions and liquid biological materials.

As for the interpretation of the THz CD spectrum of DNA, the theoretical study is still lacking mainly due to the simulation difficulties imposed by the large size of DNA molecules. We are currently seeking collaborations who may have the capability to run such simulations or have a better idea of simplifying the problem. Experimentally, shorter DNA or RNA molecules called "oligonucleotides" [1] which may be relatively easier to simulate can be measured, but it is possible that shorter molecules may have a response frequency outside our current measurable THz range therefore different THz sources, detectors, polarizers may be needed.

6.2 THz spectroscopy of bacterial biofilms

In Chapter 3, the THz properties of several bacterial biofilms, both in freeze-dried state and in pristine wet state, are investigated using THz-TDP for the measurements of extinction and circular dichroism. The conclusions include: *S. aureus* and *B. subtilis* biofilms grown in PNG and TSBg media, whether they are freeze-dried or pristine wet, exhibit an absorption band at 0.6 – 0.8 THz which is consistent with molecular dynamics simulation and negative circular dichroism at around 1 THz; for wet biofilms, lens tissue is so far the best substrate for transmission/extinction measurement and a good one for circular dichroism measurement if it is taken within a short time with care; the calculation of relative extinction eliminates the strong interference of water absorption and clearly shows the absorption bands of pure biofilms; by gradually dehydrating the pristine wet biofilms, water is revealed as a necessary and important part to induce and enhance the THz absorption of vibrational modes in biological systems, which is also predicted by the molecular dynamics simulation.

All the measurements done so far are taken on the whole biofilms, therefore one of the future directions is to measure the individual biomolecules such as amyloid fibers, eDNA, etc.

separated and purified from biofilms in order to identify the origin of the THz signals and understand the functions of each individual ECM component.

As for the experimental setup, better control of the humidity surrounding the wet biofilms is needed to reduce the interference of water vapor spikes in the relative extinction spectrum and to clearly determine the potential vibrational modes at higher frequencies. This may be achieved by a specially designed humidity-controlled sample chamber transparent to the THz beam.

A quantitative study of the water effect on the THz signals and biological functions is also desired. This can be realized by integrating a flow cell to the THz setup, where the amount of water/media can be precisely determined and varied through the flow speed.

In terms of the potential electromagnetic communication between biological cells (DARPA "RadioBio" project), our THz extinction and CD spectroscopy is only limited to studying signal detection and finding out potential THz "antennas" in these biofilms. For the other necessary components of communication including signal generation and transferred information, there are plenty research opportunities for the future work. A custom-built THz FTIR spectrometer has been bought and installed for the purpose of THz emission spectroscopy of biofilms. After I assembled the vacuum system, tested liquid helium cooled bolometer detector, calibrated the whole FTIR and trained new students on its operation, my labmate has recently started taking THz emission spectra from biofilms with it. Finally, to examine how this THz communication affect the growth of biofilms, an experiment has been proposed to use an external THz source to "jam" the biofilms and then observe the changes in their growth. It is certain that with more experimental results and increased understanding of bioflms in the near future many other new ideas will be brought up along these directions.

6.3 Kirigami modulators and THz circular dichroism spectroscopy

In Chapter 4, real-time THz polarization modulation is enabled by our chiral kirigami modulators, based on which a new spectroscopic method – THz circular dichroism (TCD) spectroscopy – is developed and demonstrated on several biological materials. The main conclusions of this project are: THz polarization rotation as large as 80° and ellipticity up to 40° for both left-handed and right-handed polarization states have been achieved; the operating frequency can be tuned for a wide range by either varying the slant angle of the gold strips or changing the unit cell size of the kirigami pattern; finite element simulation matching the experimental data reveals the origin of the polarization modulation as the chiral plasmonic resonance in buckled metal strips; real-time TCD spectrometer has been demonstrated for the first time showing its capability to explore unknow properties of a wide range of materials.

The studies on THz polarization control and TCD spectroscopy are only at their early stages, so they provide many exciting opportunities for both fundamental research and practical applications for future work.

First, for the magnitude of polarization control a rotation of 90° and an ellipticity of 45° are desired which means any modulation between and including linear and circular polarizations can be realized. Our current kirigami modulators are not able to achieve these numbers; even though it has been shown that by stacking two or more modulators the modulation depth can be improved, the method is at the great cost of losing transmitted signals and the improvement saturates very quickly. Therefore, what is needed is a further optimization of the sample design in every possible aspect, including structures, mechanical properties, materials used, etc. Secondly, for the frequency range of any modulation, a broadband or a tunable spectral response is always wanted. In our current method, different kirigami modulators must be used in order to have different frequency responses. We have tried to incorporate a mixture of many different slant angles in one kirigami sample and demonstrated its broadband response between 0.4 - 0.8 THz but the magnitude is much reduced. In this sense, future work can be done on the optimization of this mixed kirigami modulator for a strong broadband modulation. Alternatively, a frequency-tunable modulator can provide another option, which will require a totally different design and need very advanced knowledge of mechanical engineering and topology. It may be difficult, but it is surely an exciting direction for future work.

As for TCD spectroscopy, the first future task would be to synchronize the modulator controller with the existing THz setup (rapid scan stage, function generator for the THz emitter, lock-in amplifier) to check how much the sensitivity can be improved and the potential for a practical TCD spectrometer for research and commercial applications. Materials-wise, since there are almost no experimental results about TCD available except a few examples presented in our work, any potential chiral material, including a wide range of biochemical molecules, various metamaterials, complex biological systems and novel optoelectronic materials (e.g. Weyl semimetal [2,3]) and devices, is a promising candidate for future research. The associated theoretical and computational studies of interpreting these potential TCD results and exploring the unknown THz chiral properties also present great research opportunities for future work.

6.4 Optical properties of epitaxial graphene buffer layer

In Chapter 5, ultrafast infrared spectroscopy has been used as the main tool for the studies of the optical properties of epitaxial graphene buffer layer on SiC(0001). Although the investigation is still preliminary, some promising results are obtained: due to the interaction with the substrate, graphene buffer layer at room temperature shows totally different electronic and optical properties from conventional graphene layers; from ultrafast infrared pump-probe spectroscopy and UV-Vis spectroscopy, it is proposed that a bandgap opening or a series of separate states between 2 eV to 2.4 eV exists in room-temperature buffer layer; it has been demonstrated that a self-built heating system is compatible to the infrared pump-probe spectrometer for differential transmission measurement at above 1000 °C; the differential transmission signals at high temperature match the hypothesis that a buffer layer can be decoupled from the substrate into a free-standing graphene layer with high thermal energy.

There are many challenges but also opportunities for this project, both engineeringly and scientifically. At the moment, the most important issue that needs to be solved is to have a better heating and vacuum system to avoid sample intercalation at high temperature. More advanced design with the consideration of gas pressure, mechanical vibration, heat endurance, etc. are needed and industrial solutions may be sought. After solving this problem, the temperature-dependent pump-probe experiment can be expected to either verify or reject the hypothesis of the semiconducting-semimetal transition in buffer layer.

In addition to the infrared pump-probe spectroscopy and UV-Vis spectroscopy presented in this thesis, other spectroscopic methods can provide additional and/or complementary insights on the optical properties of the buffer layer. First, Fourier transform infrared spectroscopy (FTIR), as a good method for the study of near- and mid-IR absorption, has been performed on both SiC substrates and buffer layers, but the results showed very strong fringe patterns whose origins are still unclear – they could come from the finer structures on SiC substrates, or the misalignment of the instrument, or something else that we are not aware of yet – and need deeper investigation in the future. Secondly, with a potential bandgap opening above 2 eV which corresponds to a transition shorter than 620 nm, visible pump-probe may be a better method to directly study the electronic structure and the carrier dynamics of the buffer layer at room temperature. However, the SiC substrate starts to have huge absorption below 400 nm and may contribute a large two-photon absorption for any visible wavelengths used for the pump and probe beams, so careful selections of pump-probe wavelengths and/or advanced optical techniques such as valley polarization [4] may be needed for such measurement. Lastly, if the potential bandgap is direct and the buffer layer is mostly homogeneous, photoluminescence spectroscopy may be used for a more complete characterization of the optical and electronic properties of graphene buffer layer.

With increasing knowledge of the raw material, another very important future direction will be the research on the buffer layer-based devices. It is anticipated that electronics and optoelectronics based on the epitaxial graphene buffer layer and other novel 2D materials will soon become a burgeoning field for both scientific research and practical applications.

Reference

1. Uhlmann, E., and Peyman, A. Antisense oligonucleotides: a new therapeutic principle. *Chem. Rev.*, **90**, 543-584, (1990).
2. Burkov, A. A. Chiral anomaly and transport in Weyl metals. *J. Phys. Condens. Matter*, **27**, 113201, (2015).
3. Sirica, N., et al. Tracking ultrafast photocurrents in the Weyl semimetal TaAs using THz emission spectroscopy. *Phys. Rev. Lett.*, **122**, 197401, (2019).
4. Rycerz, A., Tworzydło, J., and Beenakker, C. W. J. Valley filter and valley valve in graphene. *Nat. Phys.*, **3**, 172, (2007).